Fall 2015

# Numerical framework for mesoscale simulation of heterogeneous energetic materials

Nirmal Kumar Rai
*University of Iowa*

# NUMERICAL FRAMEWORK FOR MESOSCALE SIMULATION OF HETEROGENEOUS ENERGETIC MATERIALS

by

Nirmal Kumar Rai

A thesis submitted in partial fulfillment
of the requirements for the Doctor of Philosophy
degree in Mechanical Engineering in the
Graduate College of
The University of Iowa

December 2015

Thesis Supervisor: Professor H.S.Udaykumar

Graduate College
The University of Iowa
Iowa City, Iowa

CERTIFICATE OF APPROVAL

_____

PH.D. THESIS

_____

This is to certify that the Ph.D. thesis of

Nirmal Kumar Rai

has been approved by the Examining Committee for
the thesis requirement for the Doctor of Philosophy degree
in Mechanical Engineering at the December 2015 graduation.

Thesis Committee: _____
H.S. Udaykumar, Thesis Supervisor

_____
P. Barry Butler

_____
Kyung.K Choi

_____
Jia Lu

_____
Edward Sander

# ACKNOWLEDGEMENTS

I would like to acknowledge number of people who have helped in the successful completion of this thesis. Firstly, I want to express my sincere gratitude to my PhD advisor, Dr. H.S. Udaykumar. He has been extremely patient and helpful throughout the course of my PhD work. He is a great mentor and always motivate towards free thinking and to carry out independent research.

I would like to thank my committee members who have helped with their suggestions to make this thesis better. I would like to express my sincere thanks to Professor Jia Lu who has always entertained my questions and concerns regarding this thesis and my course work during my graduate school.

I would like to acknowledge Martin Schmidt from EGLIN Air Force Base for his consistent grant support to carry out this thesis work. Also, I would like to acknowledge Robert Dogan, Christopher Molek and Eric Welle from EGLIN AFB for the valuable suggestions and collaborative efforts which have played a crucial role in the progress of the current research.

I would like to express my sincere thanks to my family in India including my father Rakesh Rai, my mother Meera Rai, my siblings Amrita and Vishal, my aunts Sunita Pandey and Sudipta Sen, my uncles Arun Pandey and Pallav Sen who motivated me to take up PhD as a career path and for their immense support during the course of my graduate study.

I would like to thank all my past lab mates Anil, John and Seth who have always guided me during initial years of my graduate study. I would also like to thank my present lab mates Oishik, Ehsan, Liza, Sid, Pratik, Aaron, Mike, Moustafa, Jarred and Kayley for creating a fun and positive work environment in the lab.

I would like to thank my friends Pradeep, Nisarga, Suman, Gupto, Bhakti, Ipshita, Kashyap, Shivangi, Aashay, Abhay in Iowa City for all the fun and happy memories which I will cherish throughout my life.

# ABSTRACT

Heterogeneous energetic materials such as plastic bonded explosives (PBX), pressed explosives etc have very detailed and non-uniform microstructure. The heterogeneities are usually present in the form of binder, voids, microcracks etc. Shock interaction with these heterogeneities leads to local heated regions known as hot spots. It is widely accepted that these hot spots are predominantly the cause of triggering reaction and eventually ignition in these energetic materials. There are various physical mechanisms operating at mesoscale through which hot spot can be created such as void collapse, inter-granular friction in energetic crystals, shock heating of HMX crystals and binder etc. Hence, microstructural heterogeneities can play a vital role for shock initiation in heterogeneous explosives. In the current work, a general framework is established for performing mesoscale simulations on heterogeneous energetic materials. The numerical framework is based on a massively parallel Cartesian grid based Eulerian solver. Narrow band level set approach is used for sharp tracking of the material interfaces. The interfacial conditions are applied using modified ghost fluid method. The use of level set method for interface tracking provides an inherent advantage of using level set based image segmentation algorithm(active contouring) for the representation of explosives microstructure. The image processing approach allows to perform simulation on real geometries than the idealized shapes. The image processing framework is incorporated in the Eulerian solver. The energetic material considered in the current work is HMX. The chemical decomposition of HMX is modeled using Henson Smilowitz chemical kinetic law. Shock analysis is performed on two different samples of HMX based pressed explosives. Also, both two dimensional and three dimensional shock analysis on mock sugar geometry are performed. The effect of shock strength and relative positioning of voids on ignition threshold of porous HMX is studied. The current work is focused towards the development of a computational framework which can replicate the experimental way

of studying the shock initiation behavior of energetic materials i.e. using flyer plate simulations.

# PUBLIC ABSTRACT

Heterogeneous energetic materials are commonly used in various engineering applications such as mining, munitions, propellants design etc. Examples of such materials are plastic bonded explosives (PBX), pressed explosives etc. Energetic materials are useful because it can release large amount of energy in a very short span of time through initiation of chemical reactions, ignition and detonation. However, rapid release of energy in energetic materials makes them unsafe to handle as even small external disturbances may cause runaway thermal heat release. The behavior of energetic materials is highly unpredictable, which poses challenges related to the controlled design. The controlled design of heterogeneous energetic materials requires understanding of the physical mechanisms which govern the chemical reaction initiation and ignition process. The chemical reaction in heterogeneous explosives initiates because of various physical mechanisms operating at the microstructural scale (mesoscale). The current work is aimed towards understanding of these governing physical mechanisms and sensitivity characterization of heterogeneous energetic materials under shock load using mesoscale numerical simulations.

TABLE OF CONTENTS

LIST OF TABLES

LIST OF FIGURES

# CHAPTER 1

# INRODUCTION

## 1.1 Background and motivation

Engineering applications such as mining, design of propellants devices for rocket propulsions, design of munitions etc uses energetic materials for high energy release and deposition. Examples of energetic materials are cyclotetramethylene-tetranitramine (HMX), triamino-trinitrobenzene (TATB), trimethylenetrinitramine (RDX) etc. It is an interesting question to find out that what makes energetic materials special compared to other organic compounds such as coal, kerosene etc. It can be intuitively reasoned that energetic materials have high energy content per unit mass which is released when undergoing combustion. It is true that energetic materials have considerable amount of energy content, however comparison of heat of combustion of HMX, kerosene and coal reveals some interesting information. For example, heat of combustion of coal (anthracite) is 30.8 $MJ/Kg$, for kerosene it is 43.3 $MJ/Kg$, and for HMX[3] is 9.9 $MJ/Kg$.The heat of combustion of HMX is considerable lower than many non-detonable organic compounds which are present in nature. So, if it's not the energy content, then what makes energetic materials sensitive? This can be understood by analyzing the chemical structure of these compounds. The molecular structure of HMX, kerosene and coal is shown in Figure 1-1. The difference between HMX and kerosene or coal is that, HMX molecule contains both fuel and oxidizer (oxygen) bonded together in a single stable compound, whereas kerosene or coal does not contain oxygen in their molecules. Hence, HMX is a self-sustaining molecule which can undergo combustion itself i.e. the oxygen required for combustion is provided from the molecule itself. However, coal or kerosene requires oxygen from their surrounding environment for combustion. This causes energetic materials to release high amount of energy very quickly (typically of the order of microseconds to nanoseconds)

through violent chemical reactions. This quick release of energy makes energetic materials useful for the mentioned engineering applications.

There are various forms in which energetic materials are used in real life applications. The current work is focused towards analysis of two commonly used heterogeneous solid explosives. These are plastic bonded explosives (PBX) and pressed explosive. PBX and pressed explosives vary from each other in terms of their composition and the way they are synthesized. PBX are composite materials formed by binding/coating energetic crystals such as HMX with polymeric binder materials such as estane[4]. On the other hand, pressed explosives are formed by pressurizing energetic crystals with each other to cast in some desired shape to use it for a particular application. There can be many different variations of both of these types of explosives based on the type of energetic crystals, crystal sizes, percentage composition of binder, porosity etc. For example, PBX9501 and PBX 9404 are two different types of PBX one with 95% HMX by weight and other with 94%. Also, Class III and Class V are two examples of pressed explosives[5], both samples vary from each other in terms of the respective crystal size. Figure 1-2 and Figure 1-3 shows the microstructure of PBX and pressed explosives.

As it was mentioned previously, the self-sustaining combustible property of energetic materials is the key characteristic which makes them useful. However, it is this property too which poses challenges related to its safety in handling and transport. Heterogeneous explosives are extremely sensitive to mechanical insult; application of transient loads may lead to initiation and run away thermal heat release even when it is not desired. Safety of heterogeneous explosives is a concern because of its highly uncertain behavior subjected to different environmental conditions. For example, a sample of heterogeneous explosive might not detonate under a strong impact but it may initiate chemical reactions even under mild loading situations. There are many examples[3] from history that shows that even following proper handling and transport practices had led to many catastrophic destructions[3]. It is an extremely challenging task to design or predict

explosives behavior for any general situation with full confidence. However, it is important to design explosives so that its behavior is controllable i.e. it should perform as it is desired to and remain insensitive in other scenarios.

## 1.2. Sensitivity characterization of heterogeneous energetic materials

The performance assessment and controlled design of heterogeneous energetic materials are attributed towards its sensitivity characterization. The sensitivity measurement of heterogeneous explosives can provide some insightful information which can help in efficient design of explosives with the determination of safety envelope corresponding to the various different loading scenarios.

Heterogeneous energetic materials under applied shock load may initiate chemical reaction depending on the loading strength. The initiation and growth of chemical reaction releases reaction fronts and blast waves in the energetic materials. The interaction of these reaction fronts and blast waves with the incident shock wave leads to the propagation of detonation wave. The distance travelled by the incident wave to transform into full detonation front is termed as run-to-detonation distance[6]. The logarithmic plot of variation of run-to detonation-distance/time with respect to incident pressure loading is known as Pop-plot[7]. Pop-plots can be used as one of the ways to characterize the sensitivity of the HE materials[7]. In the past, various experimental [8-10] methodologies were employed to characterize run to detonation distance and Pop-plots. Figure 1-4(a) shows Pop-plot[1] for HMX based and TATB based explosive. It can be seen that for both the type of explosives, as incident loading magnitude (quantified using pressure) increases, the run to detonation distance decreases. The decrease in run to detonation distance indicates high sensitivity. Also, TATB based explosive requires high loading strength as compared to HMX based explosive to obtain the same run to detonation distance. This shows that TATB based explosive is less sensitive than HMX based one. Hence, one can

represent the gross sensitivity dependence of explosives on the different loading conditions using Pop-plot.

The effect of loading on sensitivity of explosives can also be obtained using initiation threshold curve as shown in the work of James[2, 11, 12]. The initiation threshold curve is obtained by finding out under what loading conditions a particular sample of explosive will detonate. Flyer plate experiments are performed to load the explosive samples. The initiation threshold curve for PBX9404[2] material is shown in Figure 1-4(b). The points shown on the curve are the conditions i.e. flyer speed and velocity which has led to detonation for this sample. It can be seen that with the increase in flyer plate thickness, less velocity is required to detonate the material and thinner flyer requires higher speed of impact for detonation.

Pop-plots[7] and James initiation threshold curve[2] are some of the ways to represent the sensitivity of explosive samples. In order to obtain these plots, data from physical experiments performed on explosive material is required. Significant development of experimental methodologies[5, 13-19] have taken in past to understand the behavior of explosives. However, design of such experimental set up can be challenging considering the uncertain and extremely sensitive behavior of explosives. It requires sophisticated measurement equipment's and techniques and that makes experiments very expensive. This has led to the development of numerical methods to quantify the sensitivity of the HE materials.

### 1.3.Numerical modeling of energetic material: macroscale approach

In previous works, numerical simulations to study shock initiation behavior of energetic materials were performed by modeling heterogeneous explosives by treating them as homogenized solids[20, 21]. The effects of mesoscale physical phenomena contributing to the formation of hot spots were modeled using phenomenological burn

models. These models attempt to reflect the mesoscale hot spot energy deposition mechanism at macroscale using closure terms. The commonly used burn models are Ignition and Growth[20], Forest Fire[22] and JTF model[23]. Although, these macroscale approaches are able to characterize sensitivity of energetic material, they carry some inherent disadvantages[24].

Firstly, although, reaction initiation and detonation in energetic materials are observed at macroscale, it is well understood that physical processes that initiates chemical reactions operates on meso-scale (scale of material microstructure) and it depends intrinsically on the microstructural details of the energetic materials. The use of averaging methods leads to loss of localized information which is important to predict the shock initiation behavior. Secondly, in these burn models, the initiation, ignition and growth of chemical reaction depends directly on the applied pressure loading, while the underlying chemical kinetics follows the Arrhenius rate law i.e. it is temperature dependent. Also, the values of fit constants to parameterize the burn models are obtained using experiments performed on particular batches of explosives and apply to specific formulations. Their applicability in the face of variations of formulations in terms of composition or microstructural differences is therefore difficult to determine. Hence, for a complete understanding and general applicability of sensitivity measurement it is desirable to use mesoscale simulations which can model the material heterogeneities.

### 1.4.Numerical modeling of energetic material: mesoscale approach

Heterogeneous energetic materials[25] have a non-uniform microstructure due to the presence of heterogeneities in the form of binder material, voids, microcracks etc. The interaction of incident load with these heterogeneities leads to the formation of locally heated regions termed as “hot spots”[26]. It is an established concept that these hot spots acts as the favorable sites for triggering chemical reactions. Hot spots can be formed

through different physical mechanisms which operate at the meso-scale. A detailed description of ten different hot spot formation mechanisms is discussed by Field[27]. These includes adiabatic compression of gases trapped in the void regions under applied load[28-32], hydrodynamic collapse of voids under shock loading leading to the formation of material jet[33, 34], viscous or plastic heating due to deformation of the voids[35], intergranular frictional heating arises due to impact between energetic crystals[28-30, 36-38], formation of adiabatic shear bands[39-43] in the material during mechanical failure etc. Each of these mechanisms plays role in the formation of hot spots depending on the loading regime, microstructural details of the energetic material etc. For example, hydrodynamic void collapse is considered to be one of the predominant hot spot formation mechanisms in strong shock load regime[44-46]. In order to understand the relative importance of these hot spot formation mechanisms in different loading conditions mesoscale numerical framework is desired.

Mesoscale simulations can reveal important physical mechanisms which lead to initiation and ignition in energetic materials. The possibility of extracting physical insights that may not be easily derived from physical experiments have motivated the research community to develop mesoscale numerical frameworks in the past [1, 24, 47-59]. The focus of these mesoscale frameworks were mainly to model and capture the various mechanisms causing hot spot formation such as void collapse[45, 56-62], friction[63-65], material heterogeneities[48, 50, 52, 54, 66], heating due to elastoplastic deformation[4, 66, 67]. Of course, these mechanisms need to be modeled accurately to predict the correct hot spot temperature which eventually leads to the initiation of chemical reactions. The formation of hot spots is a localized phenomenon and it depends greatly on the local morphological characteristics of the explosives. The effect of morphology on hot spot prediction was studied in the past[48, 52, 55, 60, 64, 67] by modeling the microstructural details using various approaches. Mas and Clements [48, 49] used the HMX particle size distributions to design a representative volume element (RVE) consisting of HMX crystals

and plasticized binder in both two and three dimensions. The effective properties of the RVE is modeled using Mori-Tanaka[68, 69] effective medium theory. Baer's[52] work included Monte Carlo and molecular dynamics based methods to pack the randomly distributed crystals with prescribed porosity. Image processing techniques applied on experimentally generated digital images is incorporated in an Eulerian hydrocode in the work of Benson and Colney [54] to perform simulations on real meso-structure. In the work of Barua and Zhou[55], the image of PBX microstructure is used to generate cohesive finite element model to perform mesoscale simulations. The extraction of explosive geometry from experimentally generated images is one of the important ingredients for accurate hot spot prediction.

The current work is focused towards shock initiation characterization of heterogeneous energetic materials. In the strong shock regime, amongst various mechanisms, void collapse is often considered as predominant and has garnered extensive study[44-46, 56, 57, 60]**.** Presence of voids in an energetic material increases its sensitivity, as measured for example by the relationship between void fraction and run-to-detonation[25]**.** Previous work has characterized the void collapse phenomenon at the mesoscale in HMX explosives[45, 56-60]. The work by Menikoff [45] provides interesting insights into the phenomenon of void collapse and the involvement of dissipative phenomena such as viscous dissipation and plastic work in the formation of hot spots. Void collapse leading to hot spot formation and initiation of reaction has been analyzed in the work of Tran et. al.[57] where HMX decomposition was modeled using the McGuire and Tarver [70] 4-equation chemical kinetic law for HMX. The effect of void size and loading intensity on energy deposition in HMX was also demonstrated. The recent work by Levesque and Vitello[60] has shown the effect of various void shapes such as spherical, elliptical, cylindrical, conical etc on the post collapse temperature. It was observed that energy deposited by voids depends on the orientation of these voids with respect to the incident shock loading.

The formation of hot spots after void collapse may or may not lead to initiation of chemical reaction in heterogeneous explosives. The reaction initiation depends on the local temperature of the hot spot and its size. The reaction can initiate only when the local hot spot conditions are maintained before mechanisms like heat diffusion starts playing a role in extracting energy from the hot spot. This was discussed in the work of Tarver et. al.[71] where the critical size of hot spots was determined for HMX and TATB materials. It was shown that for a given temperature of the hot spot there exists a critical size above which reaction initiation will be imminent. Moreover, it was also observed that the surrounding temperature of hot spots can increase its sensitivity towards ignition. The analysis by Tarver et. al.[71] characterizes the ignition threshold based on constant temperature distribution over an already created (by some means) hot spot. In fact, the hot spot size and its temperature distribution is determined by the mechanisms that initiated the hot spot, such as void collapse. Hence, the estimate of ignition threshold based on morphological feature of energetic materials such as void size and prescribed loading conditions is desirable.

### 1.5.Accomplishments of the present work

Homogenized continuum models as mentioned in the previous section are not capable of characterizing the local hot spot formation in heterogeneous energetic materials arising due to various physical phenomenon which may arise under impact loading due to averaging process involved. Hence, mesoscale modeling of the heterogeneous explosive is necessary for the accurate characterization of the physical processes that can cause the formation of local hot spot leading to initiation of chemical reaction and ignition.

In this work, a numerical framework for mesoscale computation on heterogeneous energetic materials like plastic bonded explosives (PBX), pressed explosives etc. is developed which can identify reasons that leads to the initiation of chemical reactions and ignition in heterogeneous energetic materials in the high shock load regime. The hot spot

mechanism considered in this work are void collapse, shock heating of the HMX crystals and plastic deformation of HMX crystals. The numerical framework is based on Eulerian Cartesian grid-based massively three dimensional solver[72-75] combined with a level set based image processing machinery[76] to characterize the real microstructure of the explosives. The image to computation approach for mesoscale simulation on explosives allows for the accurate prediction of hot spot location and its strength.

A seven step chemical kinetic mechanism for HMX decomposition given by Henson-Smilowitz[77] is incorporated in mesoscale computation of HMX based explosives for the shock initiation and ignition study. The chemical kinetic equations are solved using 5th order Runge Kutta Fehlberg method[78] and the chemical species are advected with the flow using Strang splitting approach. The chemical reaction model is parallelized in the current framework using MPI libraries. The HMX decomposition mechanism with the current numerical framework is able to predict the ignition sites in the domain based on the local hot spot conditions.

This work characterizes shock initiation and ignition criterion in HMX due to void collapse using the Henson-Smilowitz chemical decomposition law[77]. Various factors such as shock strength and void volume fraction in the heterogeneous HMX is identified that can significantly affect shock initiation and ignition behavior of the explosive. Also, this study is able to develop an internal energy based ignition threshold criterion for HMX which depends on shock speed and void positioning.

The framework developed is also used to study the shock initiation behavior of plastic bonded explosive and two categories of pressed explosives i.e. Class III and Class IV. The shock analysis is performed on the real microstructures by performing image processing algorithms on the microstructural images[76]. The current framework is able to predict the initiation of chemical reaction and ignition in these explosives. Apart from the simulation on the real geometries, in order to understand the behavior of the pressed explosives, numerical experiments on elongated voids are designed. The numerical

experiments point out that the orientation of the elongated voids with respect to the incident shock plays an important role in the determination of which location in the pressed explosives can be critical.

Inter-granular friction between the HMX has been considered as an important mechanism for the hot spot formation. Hence, as a first step an algorithm for the treatment of contact and separation of material interfaces is being developed in the current work. The advantage of the model lies in its ease of implementation; in contrast to Lagrangian contact treatments search operations for detecting collisions are simplified by the use of level sets[79] and no local constraints to prevent interpenetration through penalty-type force application is necessary to separate interfaces. Since the framework is Eulerian difficulties associated with carrying meshes through the material interactions, managing meshes to retain solution accuracy and stability and detecting contact between interacting surfaces are circumvented. The contact conditions are handled by implicitly satisfying the interfacial conditions on the parts of the interacting material interfaces that are in contact using a modified Ghost Fluid Method[80]. Use of a sharp interface treatment obviates the need to develop special treatments for materials that coexist within a grid cell. Such subgrid material pairs are always maintained as distinct entities separated by sharp interfaces. The results obtained from numerical simulations form various multimaterial impact problems considered matches well with experimental data where available and with other numerical simulations. The contact algorithm developed can also handle any general situation of contact and impact situation involving large deformations.

This work is focused towards development of a mesoscale numerical framework which is capable to perform numerical experiments as close to physical experiments. Hence, flyer plate experiments on real samples of Class III and Class V pressed energetic samples are performed to replicate the same loading condition as applied in physical experiments.

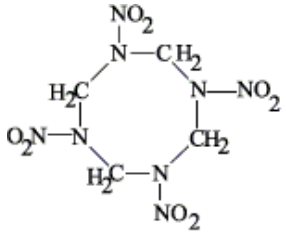

(b) HMX ($C_4H_8N_8O_8$)

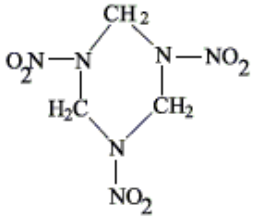

(a) RDX ($C_3H_6N_6O_6$)

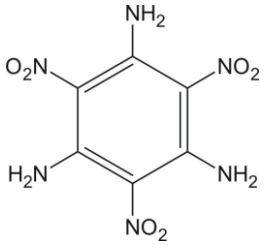

(c) TATB ($C_6H_6N_6O_6$)

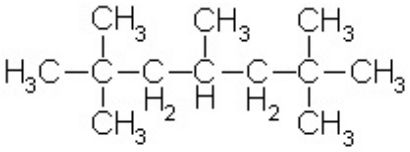

(c) Kerosene ($C_{12}H_{26}$)

Figure 1-1: Chemical structure of energetic materials (HMX, RDX, TATB) and non-energetic materials (Kerosene). The presence oxygen molecule present in the molecular structure of energetic materials makes it a self-sustaining combustible compound, whereas non energetic materials requires oxygen from the surroundings for combustion.

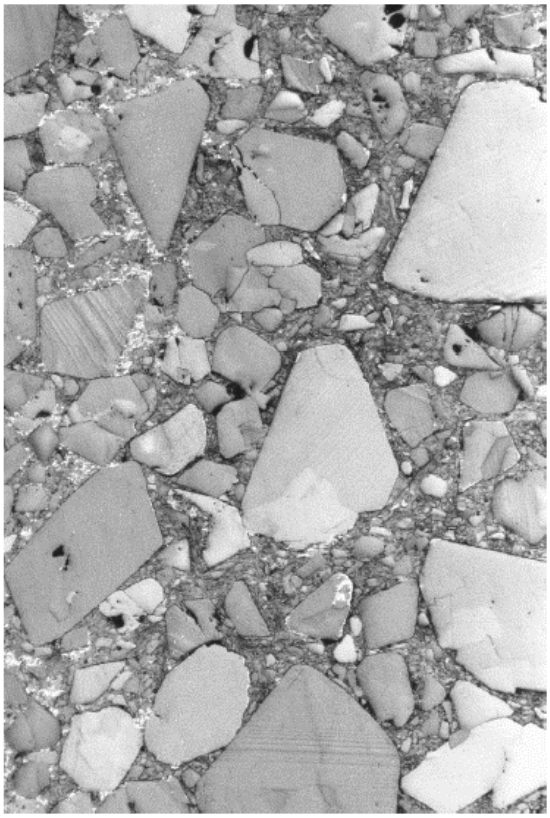

Figure 1-2: Microstructure of PBX9501 contain mixtures of coarse and fine grained HMX crystals along with binder. The image is obtained from the work of Caroline Handley[1].

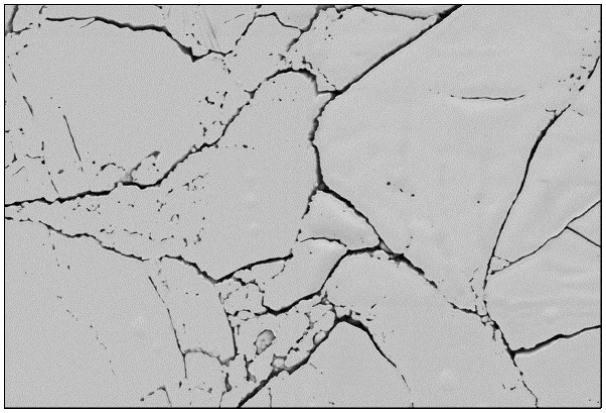

(a)

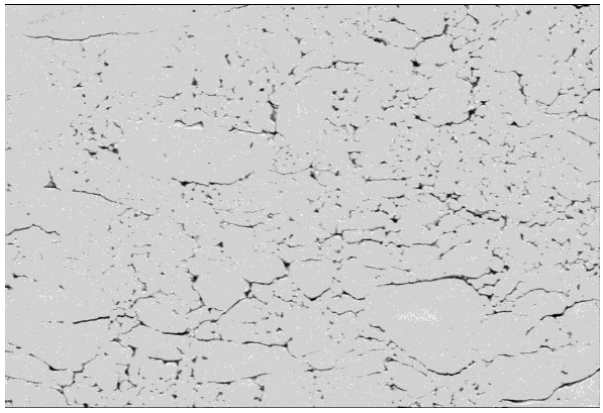

(b)

Figure 1-3: Microstructure of HMX based pressed energetic material (a) Class III type explosive (b) Class V type explosives. Both of these type of explosives vary from each other in terms of HMX crystals sizes.

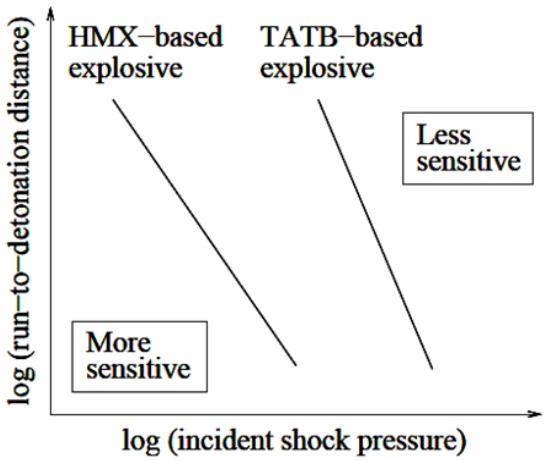


(a) Pop-plot representation of HMX and TATB based explosives

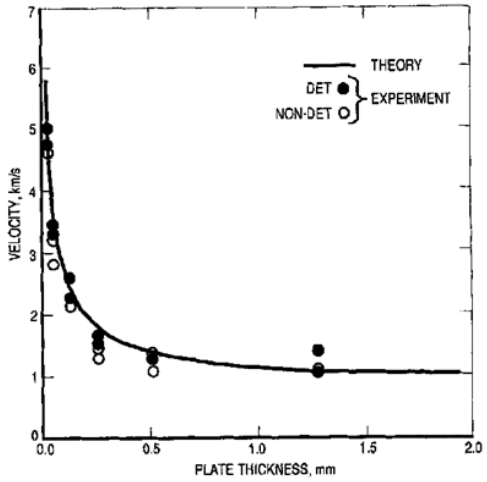


(b) Initiation threshold curve for PBX 9404

Figure 1-4: Two different types of sensitivity measurement methods (a) Pop-plot – logarithmic plot between run to detonation distance and incident loading magnitude(express in terms of pressure), plot shows two different types of explosives (HMX based and TATB based)[1]. (b) James initiation threshold curve for PBX9404[2] material, plot is showing a thresholding curve as a function of flyer plate speed and its thickness, the thresholding curve distinguishes the regions between detonation and non-detonation regimes.

# CHAPTER 2

# NUMERICAL FRAMEWORK

## 2.1 Governing equations

The governing equations in Eulerian framework comprise a set of hyperbolic conservation laws[81, 82]. In Cartesian coordinates, the governing equations of conservation of mass, momentum and energy take the following form,

$$\frac{\partial \rho}{\partial t} + div\left(\rho \vec{V}\right) = 0 \tag{2.1}$$

$$\frac{\partial \rho \vec{V}}{\partial t} + div\left(\rho \vec{V} \otimes \vec{V} - \sigma\right) = 0 \tag{2.2}$$

$$\frac{\partial \rho E}{\partial t} + div\left(\rho E \vec{V} - \sigma \vec{V}\right) = 0 \tag{2.3}$$

$$\sigma = S - PI \tag{2.4}$$

$$\frac{\partial \rho S}{\partial t} + div\left(\rho \vec{V} S\right) + \frac{2}{3}\rho G tr(D) I - 2\rho G D = 0 \tag{2.5}$$

In equations (2.1)-(2.5) $V$ is velocity, $\rho$ is density, $E$ is the specific internal energy, $D$ is strain rate tensor, and $G$ is the shear modulus of material. The stress state of material is specified by the Cauchy stress tensor $\sigma$ (equation (2.4)) which consists of deviatoric part, S and dilatational part, $P$. The dilatational part, $P$ (pressure) is given by the Mie-Gruneisen equation of state:

$$P(e,V) \approx \Gamma(V)\frac{(e - e_c(V))}{V} + P_c(V) = \Gamma \frac{e}{V} + f(V) \tag{2.6}$$

where, $e_c$ and $P_c$ denotes the reference internal energy and pressure at 0 K, and $\Gamma(V)$ is the Grüneisen parameter defined as,

$$\Gamma(V) = V\left(\frac{\partial P}{\partial e}\right)_V = \frac{\Gamma_0 \rho_0}{\rho} \tag{2.7}$$

where, $\rho_0$ is the density of the unstressed material

The function $f(V)$ is given as,

$$f(V) = \begin{cases} \dfrac{\rho_0 c_0^2 \Phi}{(1 - s\Phi^2)^2}\left[1 - \dfrac{\Gamma}{2V}(V_0 - V)\right] & if \quad V \le V_0 \\ c_0^2\left(\dfrac{1}{V} - \dfrac{1}{V_0}\right) & if \quad V > V_0 \end{cases} \tag{2.8}$$

where, $\Phi = 1 - V/V_0$ , $v = 1/\rho$ and $c_0$ is the bulk sound speed. The material parameters for the equation of state are given in Table 2-1[83].

### 2.1.1 Material models

The materials in the current work have been modeled as elasto-plastic solids. Hence, the evolution of the deviatoric stress components is performed using the radial return algorithm[84] with the yield surface being estimated using the Johnson Cook strength model[85]. The Johnson Cook strength model is given by:

$$\sigma_Y = \left[A + B\varepsilon_p^n\right][1 + \mathrm{C}\ln(\dot{\varepsilon}^*)][1 - T^{*m}] \tag{2.9}$$

where, $\sigma_Y$ is the yield stress, $\varepsilon_p$ is the equivalent plastic strain, $\dot{\varepsilon}^* = \dot{\varepsilon}/\dot{\varepsilon}_0$ , $\dot{\varepsilon}$ is the plastic strain rate, and $\dot{\varepsilon}_0$ is the dimensionless plastic strain rate.

$T^* = (T_0 - T_{ref})/(T_{MELT} - T_{ref})$ , $T_0$ is the temperature of the material, and

$T_{ref}$, reference temperature = 298 K and $\dot{\varepsilon}_0 = 1\ s^{-1}$.

A, B, C, n, m, are model constants and their values for different materials have been specified in **Error! Reference source not found.**[83].

The current work involves mesoscale simulations of plastic bonded explosives (PBX). PBX is composed of energetic crystals bonded together with polymer binders. In this work, energetic crystals are identified as HMX and polymer binder as ESTANE. Along with these two phases, arbitrarily shaped voids may be present in the microstructure because of manufacturing defects.

The mechanical behavior[86] of HMX is modeled as an elastic perfectly plastic material. The dilatational part, $P$ for HMX is given by Mie-Gruneisen equation of state. The polymeric binders typically exhibit viscoelastic behavior. The viscoelastic behavior of the ESTANE is modeled using the dirty binder model given by Mas and Clements[4]. The dilataional behavior, $P$ for the binder is given by Mie-Gruneisen equation of state. The deviatoric stresses are evolved as viscoelastic response. The shear modulus, G varies with time for the viscoelastic material. The time variation of G is obtained using a generalized Maxwell model where 22 elements prony series has been used to characterize the variation of shear modulus, G with relaxation time. The shear modulus, G variation is given by equation (2.10).

$$G(t_r) = G_\infty + \sum_{i=1}^{N_P} G_i e^{-\frac{t_r}{t_{r,i}^P}} \tag{2.10}$$

where, $G_\infty$ is the steady state shear modulus, $G_i$ is the shear modulus of $i^{th}$ element, $N_P$ is the number of terms in the prony series and $t_{r,i}^P$ is the relaxation times for each elements. The shear modulus for each elements $G_i$ and relaxation times $t_{r,i}^P$ for ESTANE is provided in **Error! Reference source not found.**[87].

## 2.2.Numerical methodology

### 2.2.1 Discretization schemes

The governing equations of mass, momentum, energy conservation along with the evolution equation of deviatoric stress components are solved using a 3rd order ENO (Essentially Non Oscillatory) scheme for the spatial discretization[88] and a 4th order Runge Kutta time integration method in the current framework. The details regarding its implementation has been discussed in the previous work[72, 89].

### 2.2.2 Level set representation of embedded interface

In the current Eulerian framework the level set method[79, 90, 91] has been used to represent embedded objects. The use of standard narrow band level set approach allows tracking the material interfaces in a sharp manner. The level set field, $\phi_l$ at any point is defined as the signed normal distance from the $l^{th}$ immersed object with $\phi_l < 0$ inside the immersed boundary and $\phi_l > 0$ outside. The interface is implicitly determined by the zero level set field i.e. $\phi_l = 0$ contour represents the $l^{th}$ immersed boundary (shown in Figure 2-1).

The details regarding the implementation of the narrow band level set approach have been discussed in previous work [72, 89]**.** Note that the level set field provides sharp delineation of all interacting interfaces so that even in those control volumes in which two or more interfaces coexist there is no mixing of the materials.

In the current framework, the mesoscale computation is performed on the real geometries of explosive microstructure rather than idealized shapes. This is facilitated with the use of image processing algorithms. The image processing algorithms uses various image formats like XCMT, SEM etc. and can generate level sets representing the image geometry with desirable accuracy. The image processing algorithms used in the current work is explained in the next section.

### 2.2.3 Image processing approach: representing real geometries

The use of level set functions to represent material interfaces gives an inherent advantage of using level set based image processing algorithms such as active contouring[7]. The image processing algorithm operates on the image intensity field and generate object interfaces using level set field. The process of obtaining the level set representation of object interfaces from images involves various steps. These steps are discussed in the following sections. This image to level set approach used in the current work is verified and validated for various biomedical images shown in the previous work of Seth et. al[76].

#### 2.2.3.1 Image representation in 2D and 3D

In the current numerical framework, the images are obtained as 2D sections of the physical geometry as shown in Figure 2-2(a). These 2D sections can be stacked upon in the physical space to obtain the 3D representation of object shown by Figure 2-2(b). The example shown in Figure 2-2(a) shows the XCMT image of a microstructure of mock sugar explosive, representing the intensity field. The image processing framework is capable of reading different formats of image files to obtain the intensity field.

#### 2.2.3.2 Noise reduction

The XCMT image of the sugar mock explosive shown in Figure 2-2 contain noises in forms of speckles, a type of multiplicative noise. These noises can lead to incorrect boundary representation of the objects. Hence, a noise reduction technique is required which can remove the image noise while preserving the edges of the objects in the domain. In the current work, speckle reduction anisotropic diffusion (SRAD)[92] algorithm is used for image denoising. SRAD is a nonlinear filtering which operates on the image intensity field and performs anisotropic diffusion based on the local intensity gradient. It inhibits diffusion near the object edges and perform intensity diffusion away from it. The governing equation for SRAD is given by equation (2.11).

$$\frac{\partial I}{\partial t} = div\left[c\left(\left|\nabla I\right|\right)\nabla I\right],\ \ I\left(t=0\right) = I_0 \tag{2.11}$$

where, $I(x,y,z,t)$ is the intensity field, $c(x,y,z,t)$ is the diffusion coefficient given by equation (2.12).

$$c\left(x,y,z,t\right) = \frac{1}{1+\left[q^2\left(x,y,z,t\right)-q_0^2\left(t\right)\right]/\left[q_0^2\left(t\right)\left(1+q_0^2\left(t\right)\right)\right]} \tag{2.12}$$

where, $q(x,y,z,t)$ is the instantaneous coefficient of variation given by equation (2.13). The values of $a, b$ and $c$ is given in Table 2-4[92] for 2D and 3D.

$$q\left(x,y,z,t\right) = \sqrt{\frac{\left|a\left(\left(\nabla I\right)/I\right)^2 - b\left(\nabla^2 I/I\right)^2\right|}{\left[1+c\left(\nabla^2 I/I\right)\right]^2}} \tag{2.13}$$

and $q_0\left(t\right) = \lambda\iint_A q^2\left(x,y,z,t\right)dxdydz \Big/ \iint_A dxdydz$, where $A$ is the image domain and $\lambda$ is the parameter to control diffusion.

Equation (2.11) is discretized and solved using explicit time integration for the mock sugar microstructure shown in Figure 2-2. The denoised image field is shown in Figure 2-3.

It can be seen from the Figure 2-3, SRAD reduces speckles present in the original image while preserving the edges of the HMX crystals.

2.2.3.3 Image segmentation

The surface modeling and its representation of image objects is obtained by applying active contour image segmentation algorithm. The level set based active contours approach of Chan and Vese[93] is implemented. The level set evolution equation based on this approach is by given by equation (2.14).

$$\frac{d\phi}{dt} = \delta_e(\phi)\left[\mu div\left(\frac{\nabla\phi}{|\nabla\phi|}\right) - \nu - \lambda_1(u_0 - c_1)^2 + \lambda_2(u_0 - c_2)^2\right] \tag{2.14}$$

where,

$\phi$ is the level set field and $\phi = 0$ represents the object boundary.

The level set equation (2.14) evolves an initial level set curve of any prescribed shape such as cylinder, spheres etc. to converged steady state solution of the level set field. This algorithm is applied on the denoised image of mock sugar explosive shown in Figure 2-3(b). A detailed description of the current implementation of active contour approach can be found in the work of Seth et. al[76].

The results obtained from active contour is shown in Figure 2-4. The HMX crystal interfaces represented using active contour level set field is superimposed on the 2D image section of Figure 2-2(a) to show the accuracy of the active contour method. It is evident from Figure 2-5 that active contour is able to represent the crystal interfaces with desirable accuracy.

The level set field obtained from the active contour approach can represent the objects precisely. However, the current numerical framework imposes certain restrictions on the obtained level set field. The level set field is required to be a signed distance function and it should satisfy the eikonal equation[79] given by equation (2.15).

$$|\nabla\phi| = 1 \tag{2.15}$$

The obtained active contour level set field (Figure 2-4) is not a signed distance function. This is because the level set curve is evolved using the image intensity field and intensity field is not a geometrical property of the object. The level set line contours obtained from active contours is shown in Figure 2-6. It can be seen that the magnitude of

the level set gradient is not constant or unity i.e $|\nabla\phi| \neq 1$. There are regions in the domain with non-uniform level set gradient.

Hence, in order to employ the numerical schemes to perform computations on the level set field obtained from active contouring, the signed distance level set field is required to be constructed around the object interfaces. The object interfaces is maintained to be fixed.

It is shown by Russo et. al.[94] that level set reinitialization method with subcell fix can be used to construct a signed distance function around an existing level set interface. The current framework incorporates this algorithm.

The signed distance function is obtained by solving the hyperbolic equation given by equation (2.16) till steady state. The steady state solution will lead the level set field to satisfy $|\nabla\phi| = 1$.

$$\frac{\partial\phi}{\partial t} = \mathrm{sgn}(\phi^0)(1 - |\nabla\phi|),\ \phi(x,0) = \phi^0(x) \tag{2.16}$$

The algorithm is explained in detailed in the work of Russo et. al[94]. The level set field for the 2D mock sugar explosive obtained from the reinitialization with subcell fix algorithm is shown in Figure 2-7. It can be seen that the steady state solution of equation (2.16) generates the signed distance level set field around existing interfaced. This level set representation of the material interfaces is consistent with the numerical solver used in the present work.

2.2.3.4 Level set mapping from image domain to flow domain

The image denoising, segmentation and reinitialization methods operates on the image domain where the domain is defined by the number of pixels in each direction. For example, 2D mock sugar explosive section is defined by $64 \times 64$ pixel. However, the numerical simulation is performed on the physical domain of the image geometry. Hence,

the level set obtained from the image processing framework needs to be mapped to the physical or computing domain from the image domain. In the current framework, a bilinear interpolation scheme is used to map the level set field.

For every grid point $(i, j)$ on the computational domain as shown in Figure 2-8, it is required to obtain the corresponding level set value from the image domain. This is done in few steps explained in this section.

*Step 1:* Firstly, the projection of the computational domain point $(i, j)$ in the image domain (denoted by $m$) is obtained using linear scaling as given by equation (2.17).

$$x_m = x_i \frac{X_I}{X_C}$$
$$y_m = y_i \frac{Y_I}{Y_C} \tag{2.17}$$

where,

$(x_i, y_i)$ is the coordinate of the computational domain grid point $(i, j)$.

$(x_m, y_m)$ is the coordinate of the projection of computational grid point $(i, j)$ in the image domain denoted by $m$.

$X_I$ and $Y_I$ are the number of pixels in $X$ and $Y$ directions respectively.

$X_C$ and $Y_C$ is the physical dimension of the geometry.

*Step 2:* The projected point $m$ may not necessarily coincide with the exact pixel location where level set values are explicitly determined using image processing approach. Hence, it is required to obtain an interpolated value of level set value a point $m$ using the local field information. In order to use any interpolation scheme to construct a level set field, the local neighbor information is needed. Hence, for point $m$, its nearest pixel point is determined by comparing the distance of the neighboring grid points. After comparing

the distances, the pixel point lying closest to the projected point $m$ is determined. The closet point thus obtained is named as point $a$ shown in Figure 2-8.

*Step 3:* To obtain the level set value at the projected point $m$, a bilinear interpolation scheme is used in the current work. Higher order interpolation schemes is avoided in this case because, it can smooth out the level set information as it uses more information locally to construct the interpolation field.

For bilinear interpolation, 4 points are required locally to construct the field in 2D and 8 points in 3D. Hence, for point $m$, its nearest neighboring pixel point $a$ and its neighbors $b, c,$ and $d$ are selected to construct the bilinear interpolation field.

The bilinear field in 2D is assumed to of the form given by

$$\phi = A + Bx + Cy + Dxy \tag{2.18}$$

where, $\phi$ is the level set field and $A, B, C$ and $D$ are the coefficients needed to be evaluated.

The bilinear field given by equation (2.18) needs to be satisfied at points $a, b, c,$ and $d$ explicitly.

$$\phi_i = A + Bx_i + Cy_i + Dx_i y_i \tag{2.19}$$

where, $i = a, b, c$ and $d$.

Equation (2.19) leads to the following system of equation represented as

$$\begin{bmatrix} 1 & x_a & y_a & x_a y_a \\ 1 & x_b & y_b & x_b y_b \\ 1 & x_c & y_c & x_c y_c \\ 1 & x_d & y_d & x_d y_d \end{bmatrix} \begin{Bmatrix} A \\ B \\ C \\ D \end{Bmatrix} = \begin{Bmatrix} \phi_a \\ \phi_b \\ \phi_c \\ \phi_d \end{Bmatrix} \tag{2.20}$$

The values of coefficients $A, B, C$ and $D$ by solving equation (2.20).

Once, the value of coefficients are known, the interpolated level set value at point $m$ is obtained using equation (2.18). The method explained here is applied in the same way in 3D and the bilinear level set field in 3D is given by equation (2.21). It uses 8 points to construct the 3D field.

$$\phi = A + Bx + Cy + Dz + Exy + Fyz + Gzx + Hxyz \tag{2.21}$$

Step 1-3 is repeated foe every computational domain point to obtain the level set field in the computing domain. The 2D and 3D level sets of mock sugar explosive shown in Figure 2-2 is interpolated using the bilinear approach and the results is shown in Figure 2-9. The computational domain as shown in Figure 2-9(b) is of size $1mm \times 1mm$ in 2D and is of size $1mm \times 1mm \times 1mm$ in 3D shown in Figure 2-9(d). The grid size for both 2D and 3D is $0.01mm$. It can be seen that the bilinear algorithm can map the level set field from image domain to the computational domain with desired accuracy.

### 2.2.4 Ghost fluid method for elasto plastic material interactions

Boundary conditions at the sharply defined material interfaces in multimaterial high velocity impact for the elasto-plastic solids have been enforced using a variant of the ghost fluid method(GFM)[95]. GFM relies on the definition of a band of ghost points corresponding to each phase of the interacting materials. The ghost points for a material are considered to be the points lying outside the material and real points are those which are inside. The band of ghost points are defined for each of the materials present in the computational domain. Once these ghost points are identified the next step is to populate the ghost field for each of the materials. The ghost field is obtained by constructing least-squares interpolation[96] of the field variables of real material points and imposing the appropriate interfacial conditions as discussed in section 2.2.4.1. This least -squares

method has been found to work well in a wide range of situations of impact and penetration including situations that lead to the formation of small fragments**.**

Consider the example shown in Figure 2-10 in which material 1 and material 2 are separated by an interface. The band of ghost points are identified separately for each of the material as shown in Figure 2-10. Once the ghost points are identified, the ghost field for material 1 is constructed using the least square interpolation of the variables of the real points in material 1. Also, ghost field of material 2 is populated using the information of the real points of material 2. The application of least square field along with interfacial conditions leads to the population of ghost field for each materials.

Once the ghost points are identified and the values of the flow variables (e.g. density, velocities, pressure, temperature, stress components etc.) at these points are populated with the least square field, the two-material problem can be converted to two single-material problems consisting of real fields and their corresponding ghost fields. The use of GFM to convert a multimaterial problem into extended single material problems is advantageous for handling contact situations as it provides independent fields for each material. These independent fields can easily be coupled based on the contact constraints locally at the impacting interface.

The detailed implementation of GFM framework using the least-squares approach is provided in previous work [72, 74, 89].

#### 2.2.4.1 Applying interfacial conditions

In the current Eulerian framework, the interaction of the materials with each other or with the surrounding void (in the case of free surfaces) is handled by the application of appropriate boundary conditions at the location of the sharp interfaces defined by the zero-level set contour. As the interfaces are arbitrarily aligned with the Cartesian grid, in order to apply the appropriate boundary conditions the stress tensor and velocity vector is

transformed to the local normal and tangential directions. The normal and tangential velocity components are given as:

$$u_n = \left|\vec{u}_n\right| = \vec{u}.\hat{n} \tag{2.22}$$

$$u_t = \left|\vec{u}_t\right| = \vec{u}.\hat{t} \tag{2.23}$$

where, $\vec{u}$ is the velocity vector, $\hat{n}$ and $\hat{t}$ are the local normal and tangential vectors and $\vec{u}_n$ and $\vec{u}_t$ are the normal and tangential velocity vectors.

The total stress tensor $\sigma$ transformed in the local normal and tangential components is given as:

$$\tilde{\sigma} = J\sigma J^T = \begin{pmatrix} \tilde{\sigma}_{nn} & \tilde{\sigma}_{nt} \\ \tilde{\sigma}_{nt} & \tilde{\sigma}_{tt} \end{pmatrix} \tag{2.24}$$

where, the transformation matrix is given as

$$J = \begin{pmatrix} n_x & n_y \\ t_x & t_y \end{pmatrix} \tag{2.25}$$

and $\tilde{\sigma}_{nn}$, $\tilde{\sigma}_{nt}$ are the normal stress components of the stress tensor and $\tilde{\sigma}_{tt}$ is the tangential component.

Three types of conditions apply at the interfaces in the test cases shown in this work:

2.2.4.1.1 Material – Material conditions

In the case where materials interact with each other on parts of the interface, continuity of normal stress components and the continuity of normal velocity component are enforced. No constraint is applied on the tangential components of stress and velocity fields. The coupling of the normal component of stress and velocity and decoupling of the

tangential components ensures frictionless sliding between the materials. Thus, at the interfaces:

$$[\vec{u}.\hat{n}] = 0 \tag{2.26}$$

$$[\tilde{\sigma}_{nn}] = 0 \tag{2.27}$$

$$[\tilde{\sigma}_{nt}] = 0 \tag{2.28}$$

$$[P] = 0 \tag{2.29}$$

where, $\tilde{\sigma}_{nn}$ and $\tilde{\sigma}_{nt}$ are the normal components of the stress tensor, *P* is pressure.

2.2.4.1.2 Material – Void conditions

This type of interfacial condition arises whenever the material interface interacts with a surrounding void, i.e. at a free surface. Conditions corresponding to physically consistent wave reflection phenomena are enforced at all free surfaces. Hence, zero-traction conditions on the normal stress components are enforced on those portions of the interface that are free surfaces, viz.:

$$\tilde{\sigma}_{nn} = 0 \tag{2.30}$$

$$\tilde{\sigma}_{nt} = 0 \tag{2.31}$$

2.2.4.1.3 Material –Rigid solid conditions

The rigid solid interface can also modeled in the current framework in situations when a deformable solid impacts on a rigid solid. The normal velocity at the colliding interface satisfies the following dirichlet condition given as:

$$\vec{u} \cdot \hat{n} = U_n \tag{2.32}$$

where, $U_n$ is the normal velocity of the rigid solid.

The continuity of the normal stress components is enforced and to ensure the free slip condition no constraint on the tangential stress components is applied.

### 2.2.5 Contact algorithm

In order to handle collision or separation of materials at a common interface a frictionless contact algorithm is applied. The steps involved in the algorithm are explained sequentially below.

#### 2.2.5.1 Detecting collision

For all materials in the computational domain, the nodes in the Cartesian mesh that straddle the material interface are tagged as "interfacial nodes"; "interfacial nodes" are nodes that interact with the surrounding material. In the level set framework these nodes are easily identified as those for which the level set value for one of the neighbors is of the opposite sign. Thus these nodes represent the set of points in the domain that will be examined to determine if a collision is imminent or not. This procedure is carried out after each update of the interfaces. To detect collision, for every interfacial node, the distance between itself (level set indexed $l$ ) and an adjoining level set (indexed $k$) is computed using the associated level set functions from:

$$\delta_{lk} = \left|\phi_l + \phi_k\right| \forall l \neq k \tag{2.33}$$

Note that not every level set evolved in the computational domain needs to be checked for collision. Collision checking is only conducted at an interfacial node if there are two level sets whose narrow bands overlap at that node. If the distance $\delta_{lk}$ computed between the two approaching level sets is less than a specified tolerance, then the node is marked as a "colliding node" (Figure 2-11). The tolerance value is set at $\kappa\Delta x$ where $\kappa$ corresponds to the CFL number which depends on the (local) interface advection velocity used to evolve the level sets in time. Use of this preset tolerance preempts inter-penetration

of level sets. Thus, at the instant at which an interfacial node is flagged for collision treatment to take effect the two colliding interfaces are separated by a distance $\kappa\Delta x$ .

2.2.5.2 Kinematic and stress constraints

Use of the level set function facilitates the identification of colliding nodes between the materials. Once the colliding interfacial nodes are identified, the next step is to calculate the traction at the common interface between the neighboring materials, as shown in Figure 2-12(a). The tractions at the colliding nodes (e.g. *A1* and *A2* in Figure 2-12(a)) are calculated using a least-squares approach[96] as explained in the next section.

2.2.5.3 Calculation of the stress field at the colliding nodes

The stress field in the region surrounding the colliding nodes is required to calculate the value of normal traction at the interface. The least-squares method to obtain the stress field is explained below:

Step 1: First, all the immediate neighbors (8 in 2D) of the interfacial point where the normal traction is to be calculated are identified. For example for point *A1* the neighboring points are shown in Figure 2-12(b).

Step 2: Once the neighbors are identified then the "real" material points are selected, i.e. points which lie inside the material; those points in the stencil that lie outside the material are rejected in the calculation of stress field as shown in Figure 2-12(c). Once all the "real" neighboring points are identified the least-squares algorithm[96] is used to calculate the value of normal traction at the colliding nodes. First, the "real" neighboring material points are used to generate a bilinear interpolant given as:

$$T_n = a_1 + a_2 x + a_3 y + a_4 xy \tag{2.34}$$

where, $T_n$ is the bilinear interpolant to the normal traction field and $a_i$'s the unknown coefficients for the construction of the bilinear field.

The error in the approximation, *e* can be calculated from:

$$e = \sum_{i=1}^{n} \left( a_1 + a_2 x_i + a_3 y_i + a_4 x_i y_i - T_{n_i} \right)^2 \tag{2.35}$$

where, *n* is the total number of available "real" neighboring material points and $T_{n_i}$ is the computed value of normal traction at the neighboring nodes.

Least-squares minimization of the error (equation (2.35)) provides the coefficients of the interpolant (equation (2.34)) as follows:

$$\begin{bmatrix} \sum_{i=1}^{n} x_i^2 & \sum_{i=1}^{n} x_i y_i & \sum_{i=1}^{n} x_i^2 y_i & \sum_{i=1}^{n} x_i \\ \sum_{i=1}^{n} x_i y_i & \sum_{i=1}^{n} y_i^2 & \sum_{i=1}^{n} x_i y_i^2 & \sum_{i=1}^{n} y_i \\ \sum_{i=1}^{n} x_i^2 y_i & \sum_{i=1}^{n} x_i y_i^2 & \sum_{i=1}^{n} x_i^2 y_i^2 & \sum_{i=1}^{n} x_i y_i \\ \sum_{i=1}^{n} x_i & \sum_{i=1}^{n} y_i & \sum_{i=1}^{n} x_i y_i & \sum_{i=1}^{n} 1 \end{bmatrix} \begin{Bmatrix} a_1 \\ a_2 \\ a_3 \\ a_4 \end{Bmatrix} = \begin{Bmatrix} \sum_{i=1}^{n} T_{n_i} x_i \\ \sum_{i=1}^{n} T_{n_i} y_i \\ \sum_{i=1}^{n} T_{n_i} x_i y_i \\ \sum_{i=1}^{n} T_{n_i} \end{Bmatrix} \tag{2.36}$$

The value of the normal traction at the colliding node is then obtained from (2.34). If there are not enough neighboring points inside the materials to construct the least-squares field, then the field is not constructed and the value of traction at the colliding node itself is used. This eventuality only arises in the rare instances when there are small fragments or sharp re-entrant corners. For sufficiently well-resolved and smooth interfaces an adequate least-squares stencil is typically available.

Step 3: The normal traction obtained at the colliding nodes is next used to find the value of normal traction at the interface. First, considering any of the two materials shown in Figure 2-12(a), say material 1, the colliding nodes in this material are known a priori (labeled *A1*in Figure 2-12(a)). Then the closest colliding node in material 2 with respect to material 1 is identified (labeled *A2* in Figure 2-12(a)). These points *A1* and *A2* are used to

find the normal traction value at the intermediate interfacial point (marked in Figure 2-12(a)) using equation (2.37).

$$T_n = \frac{w_2 T_{n_1} + w_1 T_{n_2}}{w_1 + w_2} \tag{2.37}$$

where, $T_{n_1}$ and $T_{n_2}$ are the normal tractions at the colliding points which form a pair across the interface and $w_1$ and $w_2$ are the weights given as:

$$w_1 = |\phi_1| \text{ and } w_2 = |\phi_2| \tag{2.38}$$

where, $\phi_1$ and $\phi_2$ are the normal distance of the colliding nodes from the respective material interfaces (such as *A1* from material 1 interface and *A2* from material 2 interface). The weights $w_1$ and $w_2$ gives measure of the influence of the respective colliding nodes on the interfacial point. So, the farther the colliding nodes is from the interface the lesser is its influence on the calculation of normal traction at the interfacial point.

The above process is applied to all the colliding nodes of material 1 in order to enforce the contact conditions at the interface along the parts of the interacting interfaces that qualify as colliding nodes.

2.2.5.4 Implementation of contact constraints

Following contact and wave interactions at colliding interfaces, separation between the materials takes place when the materials pull apart from each other at the common impacting interface. The normal traction and normal velocity at the colliding interfacial nodes are used to identify whether the materials pull apart from each other, based on which contact conditions are applied as described below:

If $T_{n_{interfacial\,node}} < 0$ (compressive stress state) then the material-material conditions are applied to both colliding nodes (e.g. *A1* and *A2)*.

If $T_{n_{interfacial\,node}} > 0$ (tensile stress state) then the material-void conditions are applied to both colliding nodes. Once the material-void conditions come into play,

separation between the materials occurs naturally, i.e. no introduction of a void is necessary; the sharp interfaces are evolved and pull apart due to the independent velocities in the individual interacting materials.

### 2.2.6 Chemical kinetics for HMX

In the current work, HMX is modeled as reactive material. The chemical decomposition behavior of HMX is modeled using Henson-Smilowitz[77] multi-step kinetics mechanism. The chemical decomposition of HMX starts with the initial transformation of β-HMX to δ-HMX through nucleation and growth mechanism given by equation (2.39) and (2.40). The first order nucleation of β-HMX is governed by rate $k_{1nf}$ and reverse nucleation by $k_{1nr}$. The growth of both phases is governed by endothermic reactions:

$$\beta - HMX \underset{k_{1nr}}{\overset{k_{1nf}}{\rightleftarrows}} \delta - HMX \tag{2.39}$$

$$\begin{aligned} \beta + \delta &\xrightarrow{k_{1gf}} 2\delta \\ & \qquad \Delta H_1 = 9.8\ kJ/mol \\ \beta + \delta &\xrightarrow{k_{1gr}} 2\beta \end{aligned} \tag{2.40}$$

The δ-HMX thus formed transforms to ε-HMX as given by equation (2.41) and it decomposes to the other gaseous products as given by equation.

$$\delta - HMX \underset{k_{2b}}{\overset{k_{2a}}{\rightleftarrows}} \varepsilon - HMX \tag{2.41}$$

$$\delta \begin{cases} \xrightarrow{k_{2a}} 2NO_2 + 4HCN + 2NO + 2H_2O \quad \Delta H = 219.0\ kJ/mol \\ \xrightarrow[k_{2b}]{} 2NO_2 + 4HCN + 2NO + 2H_2O \quad \Delta H = 219.0\ kJ/mol \end{cases} \tag{2.42}$$

The complex gaseous reaction between $CH_2O$ and $NO_2$ formed from the decomposition of δ-HMX provides significant release of heat and this is characterized as dark zone burning:

$$CH_2O + NO_2 \underset{k_{3b}}{\overset{k_{3a}}{\rightleftharpoons}} HCO + HONO \qquad \Delta H_{3a} = 49.6\ kJ/mol \tag{2.43}$$

$$NO_2 + HCO \begin{cases} \xrightarrow{k_{2a}} CO + HONO \qquad \Delta H_{3b} = 219.0\ kJ/mol \\ \xrightarrow[k_{2b}]{} H + CO_2 + NO \qquad \Delta H_{3c} = 219.0\ kJ/mol \end{cases} \tag{2.44}$$

The temperature rise from dark zone burning leads to highly exothermic reaction characterizing the bright zone burning zone given as:

$$HCN + NO_2 \rightarrow H + N_2O + NO + CO_2 \quad \Delta H_4 = -1088\ kJ/mol \tag{2.45}$$

The kinetic law for transformation and decomposition of HMX is given by a set of coupled differential equations representing the evolution of chemical species β-HMX, δ-HMX, ε-HMX, $NO_2$ , $CH_2O$ , HCN and unreacted gaseous phase *g* as follows:

$$\frac{d[\beta]}{dt} = -k_{1nf}[\beta] + k_{1nr}[\delta] - (k_{1gf} - k_{1gr})[\beta][\delta] \tag{2.46}$$

$$\frac{d[\delta]}{dt} = -\frac{d[\beta]}{dt} - k_{2a}[\varepsilon] \tag{2.47}$$

$$\frac{d[\varepsilon]}{dt} = k_{2b}[\delta] \tag{2.48}$$

$$\frac{d[NO_2]}{dt} = 2k_{2a}(\rho - [\beta + \delta]) - 2k_{3a}[NO_2][CH_2O] - 2k_{4a}[HCN] \tag{2.49}$$

$$\frac{d[CH_2O]}{dt} = 4k_{2b}(\rho - [\beta + \delta]) - k_{3a}[NO_2][CH_2O] \tag{2.50}$$

$$\frac{d[HCN]}{dt} = 4k_{2a}(\rho - [\beta + \delta]) - k_{4a}[HCN] \tag{2.51}$$

$$\frac{d[g]}{dt} = k_{2a}[\varepsilon]\left(10\frac{k_{2a}}{k_{2a} + k_{2b}} + 8\frac{k_{2b}}{k_{2a} + k_{2b}}\right) \tag{2.52}$$

where $[\rho] = [\beta] + [\delta] + [g]$.

The rate constants for these reactions are in the form:

$$k_i(T) = \frac{k_B T}{h} Q \exp\left(\frac{T\Delta S^* - \Delta E^*}{RT}\right) \tag{2.53}$$

where, $k_b$ and $h$ are Boltzman's and Planck's constants respectively, $\Delta E^*$ and $\Delta S^*$ are energy and entropy of the activated state and $Q$ is an equilibrium constant relating the concentrations of species to reagents. The values for $Q$, $\Delta E^*$ and $\Delta S^*$ are given in [77].

The temperature change due to heat release is obtained from:,

$$[c]C_{avg}\frac{\partial T}{\partial t} = -\left(\Delta H_1 \frac{\partial[\beta]}{\partial t} + \Delta H_{2b} k_{2b}(\rho - [\delta]) + \Delta H_3 k_3 [NO_2][CH_2O] + \Delta H_4 k_4 [HCN]\right) \tag{2.54}$$

where, $C_{avg} = \left([\beta]C_\beta + [\delta]C_\delta + [g]C_{gases}\right)/[\rho]$ is the average specific heat of the system.

The specific heat for each species is linearly dependent on temperature $C_i = C_1^i + C_2^i T$ .

2.2.6.1 Numerical algorithm for reactive system

The Henson-Smilowitz rate mechanism is coupled with the governing system equations for mass, momentum, energy and evolution of deviatoric stresses. In the current Eulerian framework, the chemical species which are formed after decomposition of HMX is evolved in time and advected using:

$$\frac{\partial \rho[C_i]}{\partial t} + div\left(\rho \vec{V}[C_i]\right) = S_i \tag{2.55}$$

$[C_i]$ is the concentration of the species and $S_i$ is the production rate (equations (2.46)-(2.52)) source term for the *ith species.*

For high temperatures the reaction time scales decrease rapidly and the time scale for species advection and reaction may differ by several orders of magnitude. Hence, for higher temperatures several constraints must be applied on the time stepping of the governing equations apart from usual CFL-type stability criterion which may lead to very

small time steps and infeasible flow calculations. This numerical stiffness problem is circumvented by using a Strang operator splitting[97] approach. First, advection of species is performed using the flow time step to obtain predicted species values using an explicit update:

$$\frac{\partial \rho [C_i]^*}{\partial t} + div\left(\rho \vec{V}^n [C_i]^*\right) = 0 \tag{2.56}$$

In the second step the evolution of the species is performed using an implicit approach to correct the species concentrations due to species generation/depletion due to chemical reactions:

$$\frac{\partial [C_i]^{n+1}}{\partial t} = S_i^{n+1} \tag{2.57}$$

The species evolution equation (2.57) is solved using the $5^{th}$-order Runge-Kutta Fehlberg [78] method, which uses an internal adaptive time-stepping scheme to deal with the stiffness of the chemical kinetics.

Table 2-1: Parameters for Mie-Gruneisen Equation of State for different materials.

| Material | $\rho_0 \frac{kg}{m^3}$ | $c \frac{W}{m-K}$ | $K \frac{J}{Kg-K}$ | $\Gamma_0$ | $c_0 \frac{m}{s}$ | S |
|---|---|---|---|---|---|---|
| Copper | 8930 | 383.5 | 401.0 | 2.0 | 3940.0 | 1.49 |
| Tungsten | 17600 | 477.0 | 38.0 | 1.43 | 4030.0 | 1.24 |
| Steel | 7850 | 134.0 | 75.0 | 1.16 | 4570.0 | 1.49 |
| HMX | 1900 | 1000.0 | 0.4 | 1.1 | 2058.0 | 2.38 |

Table 2-2: Material model parameters[89] with reference to equation (2.9) where A = $Y_0$, $T_0$ = 298K.

| Material | $Y_0$ (GPa) | B (GPa) | N | C | m | G (GPa) | $T_m$ (K) |
|---|---|---|---|---|---|---|---|
| Copper | 0.4 | 0.177 | 1.0 | 0.025 | 1.09 | 43.33 | 1358 |
| Tungsten | 1.51 | 0.177 | 0.12 | 0.016 | 1.0 | 124.0 | 1777 |
| High-hard steel | 1.50 | 0.569 | 0.22 | 0.003 | 1.17 | 77.3 | 1723 |
| Aluminum | 0.324 | 0.114 | 0.42 | 0.002 | 1.34 | 26.0 | 925 |
| Mild Steel | 0.53 | 0.229 | 0.302 | 0.027 | 1.0 | 81.8 | 1836 |
| HMX | 0.26 | - | - | - | - | - | - |

Table 2-3: Shear stress and relaxation time terms for 22 element prony series elements for Estane binder in PBX9501[87].

| Shear stress prony series terms (Mpa) $G_i$ | | Relaxation times (s) $t_{r,i}^P$ | |
|---|---|---|---|
| $G_\infty$ | 0 | $t_{r,1}^P$ | $0.735e^{-15}$ |
| $G_1$ | 75.8 | $t_{r,2}^P$ | $0.735e^{-14}$ |
| $G_2$ | 117.489 | $t_{r,3}^P$ | $0.735e^{-13}$ |
| $G_3$ | 177.828 | $t_{r,4}^P$ | $0.735e^{-12}$ |
| $G_4$ | 251.188 | $t_{r,5}^P$ | $0.735e^{-11}$ |
| $G_5$ | 346.737 | $t_{r,6}^P$ | $0.735e^{-10}$ |
| $G_6$ | 457.088 | $t_{r,7}^P$ | $0.735e^{-9}$ |
| $G_7$ | 436.516 | $t_{r,8}^P$ | $0.735e^{-8}$ |
| $G_8$ | 223.872 | $t_{r,9}^P$ | $0.735e^{-7}$ |
| $G_9$ | 52.481 | $t_{r,10}^P$ | $0.735e^{-6}$ |
| $G_{10}$ | 12.882 | $t_{r,11}^P$ | $0.735e^{-5}$ |
| $G_{11}$ | 2.618 | $t_{r,12}^P$ | $0.735e^{-4}$ |
| $G_{12}$ | 2.104 | $t_{r,13}^P$ | $0.735e^{-3}$ |
| $G_{13}$ | 0.4753 | $t_{r,14}^P$ | $0.735e^{-2}$ |
| $G_{14}$ | 0.2218 | $t_{r,15}^P$ | $0.735e^{-1}$ |
| $G_{15}$ | 0.1622 | $t_{r,16}^P$ | 0.735 |
| $G_{16}$ | 0.0056 | $t_{r,17}^P$ | $0.735e^{1}$ |
| $G_{17}$ | 0.0891 | $t_{r,18}^P$ | $0.735e^{2}$ |
| $G_{18}$ | 0.0676 | $t_{r,19}^P$ | $0.735e^{3}$ |
| $G_{19}$ | 0.03802 | $t_{r,20}^P$ | $0.735e^{4}$ |
| $G_{20}$ | 0.01585 | $t_{r,21}^P$ | $0.735e^{5}$ |
| $G_{21}$ | 0.007413 | $t_{r,22}^P$ | $0.735e^{6}$ |
| $G_{22}$ | 0.004168 | | |

Table 2-4: Speckle reducing anisotropic diffusion method parameters for two 2D and 3D[92].

| SRAD parameters | 2 Dimensions | 3 Dimensions |
|---|---|---|
| $a$ | $1/2$ | $1/3$ |
| $b$ | $1/16$ | $1/36$ |
| $c$ | $1/4$ | $1/6$ |

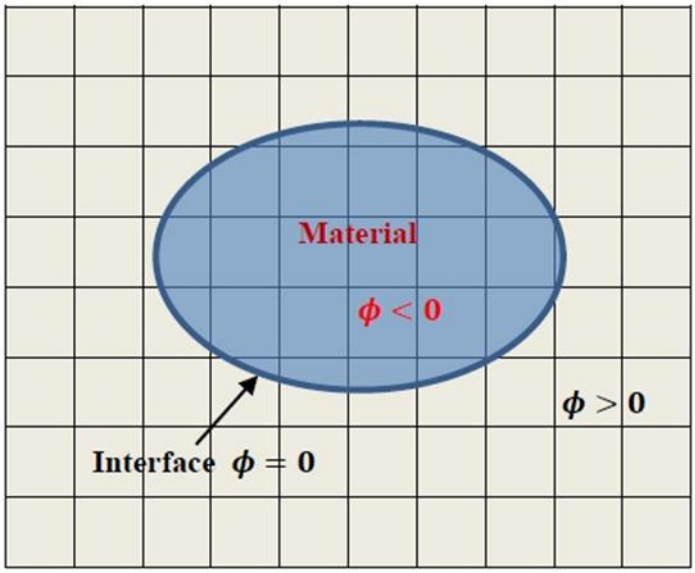


Figure 2-1: Level set representation of embedded object. Level set field $\phi > 0$, represents region outside the object and $\phi < 0$, representing inside regions.

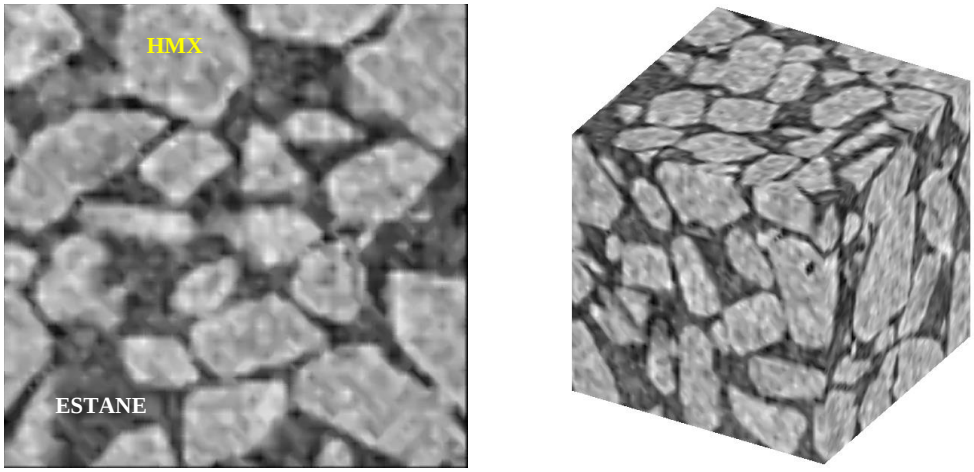


(a) 2D section – XCMT image

(b) 3D geometry

Figure 2-2: Image intensity field of sugar mock explosive consists of HMX crystals and Estane binder (a) 2D section of the explosive microstructure with $64 \times 64$ pixel size b) 3D geometry of the explosive with $64 \times 64 \times 64$ pixel size obtained by stacking up the 2D image sections.

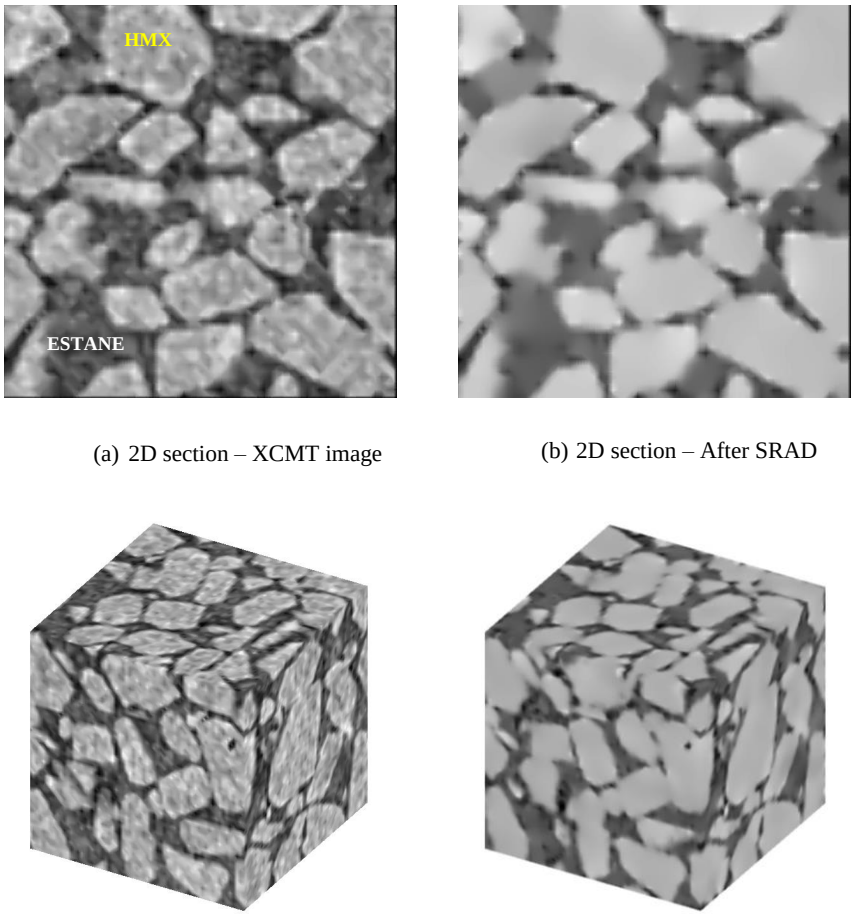


(a) 2D section – XCMT image

(b) 2D section – After SRAD

(a) 3D geometry - Original

(b) 3D geometry – After SRAD

Figure 2-3: Image intensity field obtained after applying speckle reduction anisotropic reduction algorithm(SRAD) with diffusion parameter $\lambda = 1.0$.

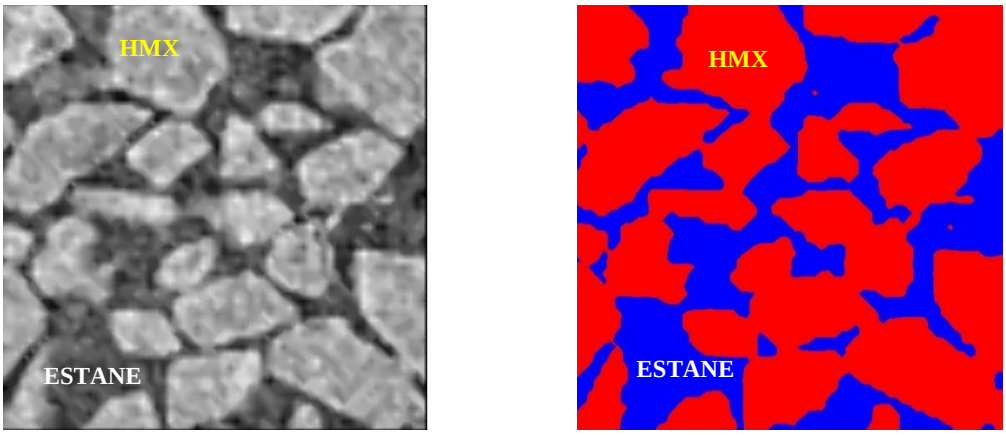


(a) 2D section – XCMT image

(b) Segmentation – level set representation of mock explosive

Figure 2-4: Image segmentation of sugar mock explosives using active contour approach.

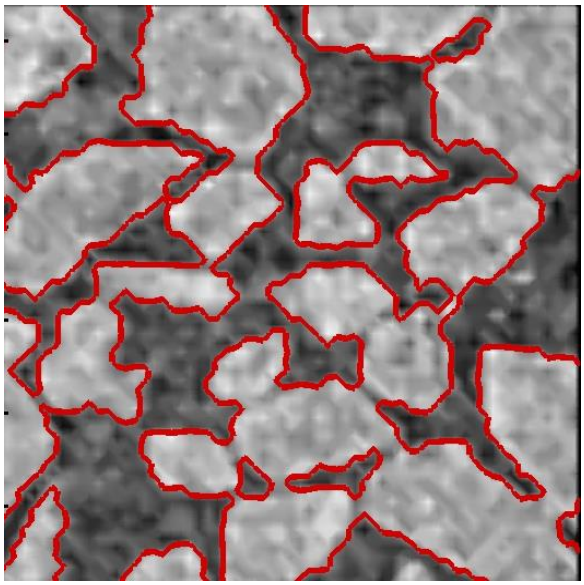

Figure 2-5: Segmented curve (Red) obtained using the active contour approach is superimposed on the original geometry of the mock explosive.

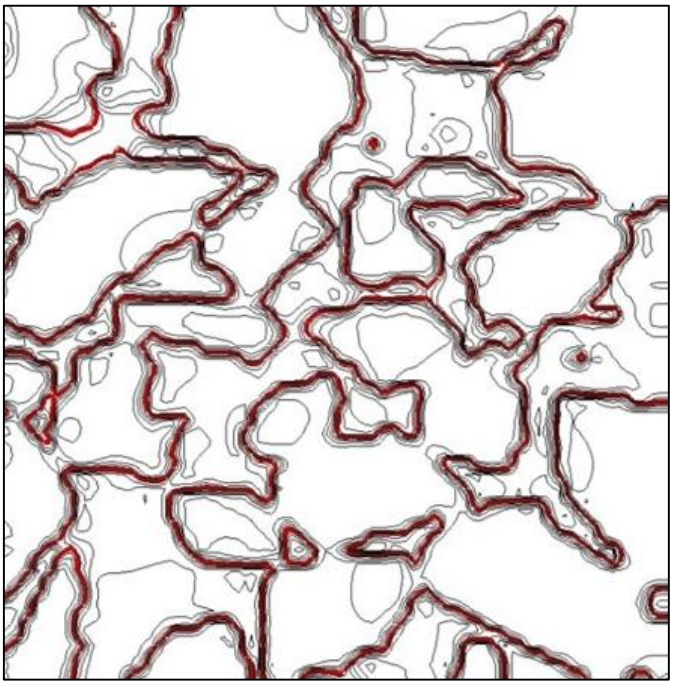

Figure 2-6: Level set field shown using line contours where HMX crystals boundary is accurately captured and displayed as the bold line. However, it does not satisfy signed distance function property.

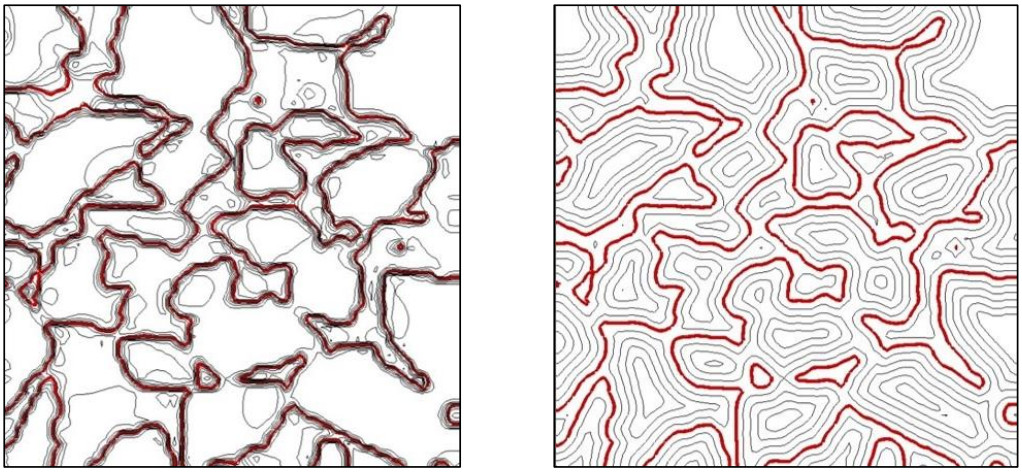

(a) Level set field after active contour

(b) Level set field after employing reinitialization with subcell fix algorithm

Figure 2-7: Level set field line contour for 2D section of mock sugar explosive, red curve represents interface of HMX crystals.

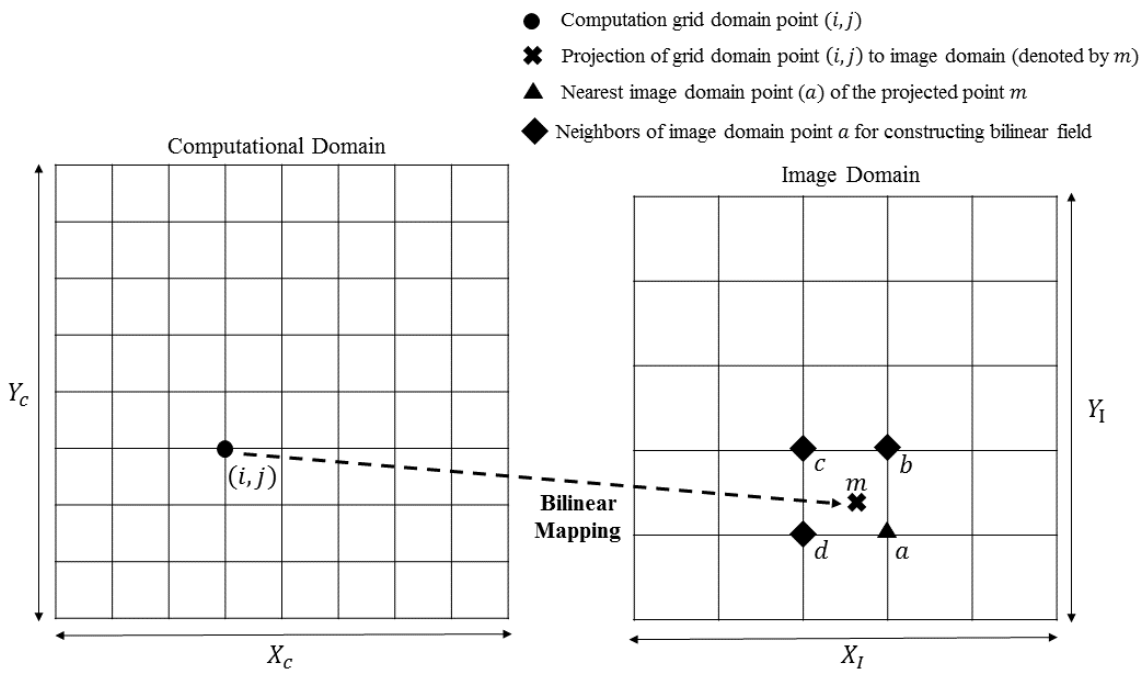


Figure 2-8: Bilinear mapping to obtain the level set information from image domain to computational domain. The image domain level set is obtained after performing denoising, segmentation on the intensity field and reinitialization of the active contour level set. $X_I$ and $Y_I$ are the number of pixels in $X$ and $Y$ directions, $X_c$ and $Y_c$ are the dimensions of the physical domain in $X$ and $Y$ directions.

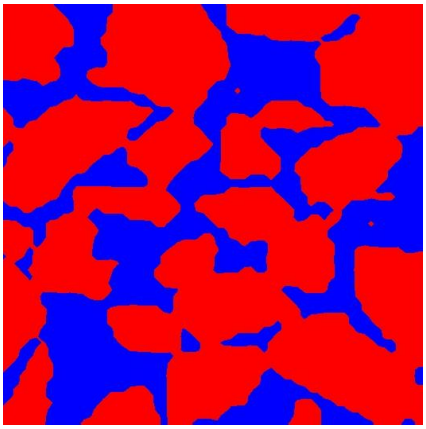

(a) Image domain - 64 × 64 pixels

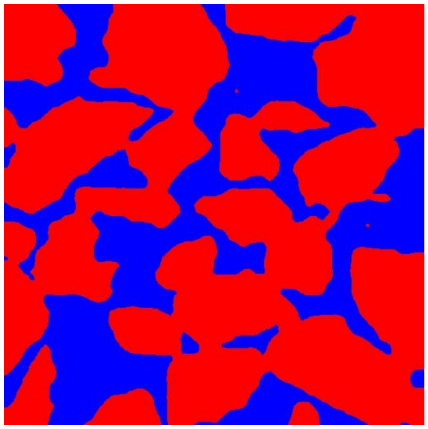

(b) Computational domain - 100 × 100 grid points

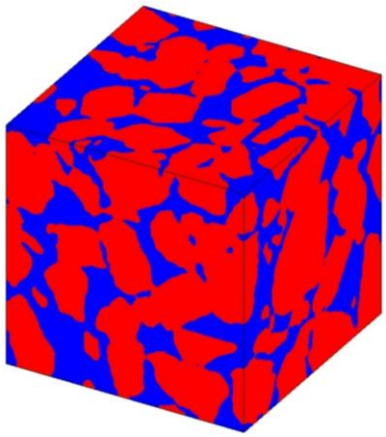

(c) Image domain - 64 × 64 × 64 pixels

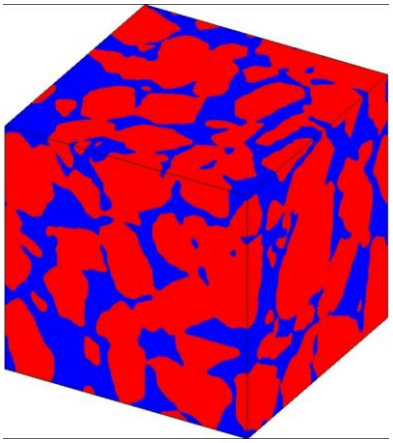

(d) Computational domain - 100 × 100 × 100 grid points

Figure 2-9: Level set geometry in both image and computational domain of mock sugar explosives. The computational domain level set field is obtained using the bilinear interpolation mapping from the image domain. The image domain contains 64 pixels in each direction for both 2D and 3D. The computation domain represents a unit square $mm^2$ and a unit cube $mm^3$ in 2D and 3D respectively with a uniform grid size of $0.01\ mm$ in each directions.

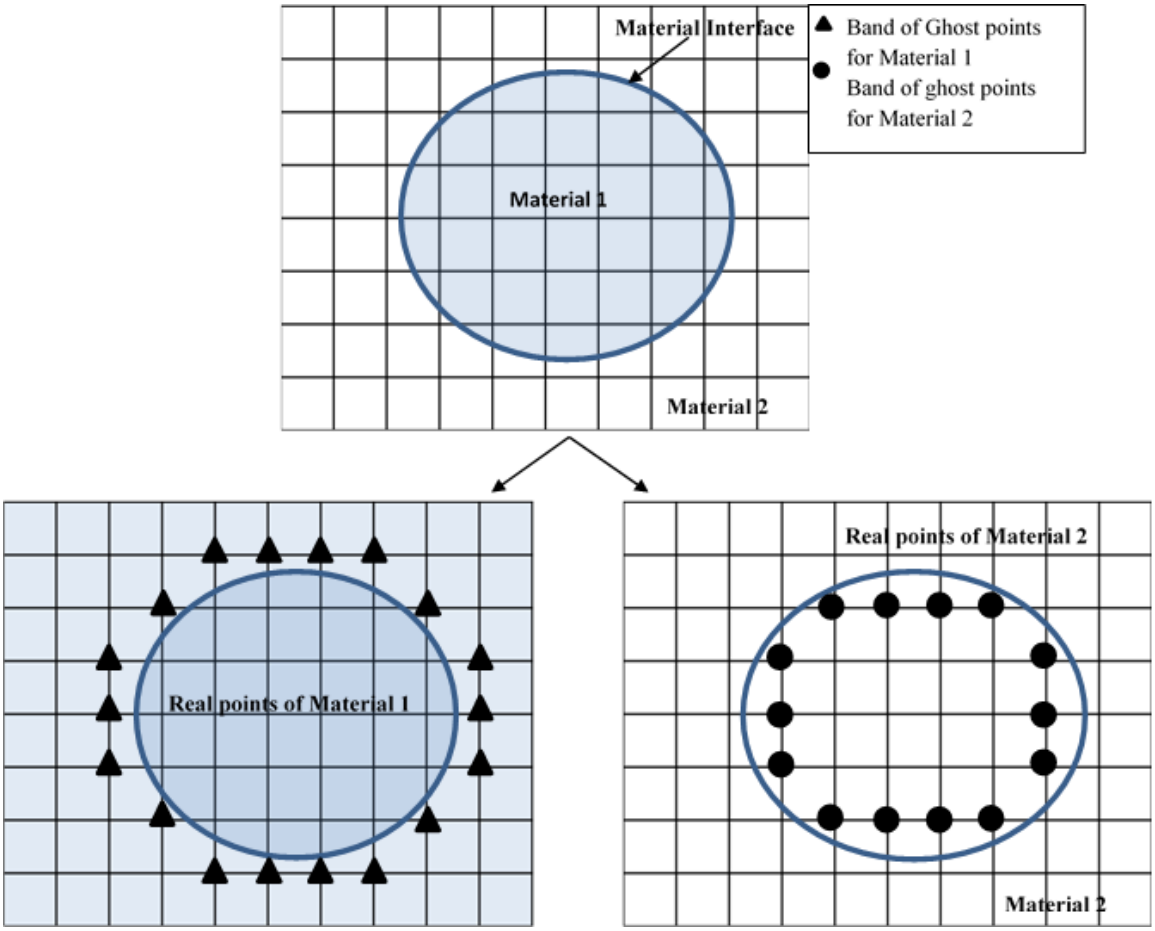


Figure 2-10: Ghost Fluid Method (GFM) converts a single multi material interaction problem into two single material problems where both materials are treated independently based on their real field and corresponding ghost field.

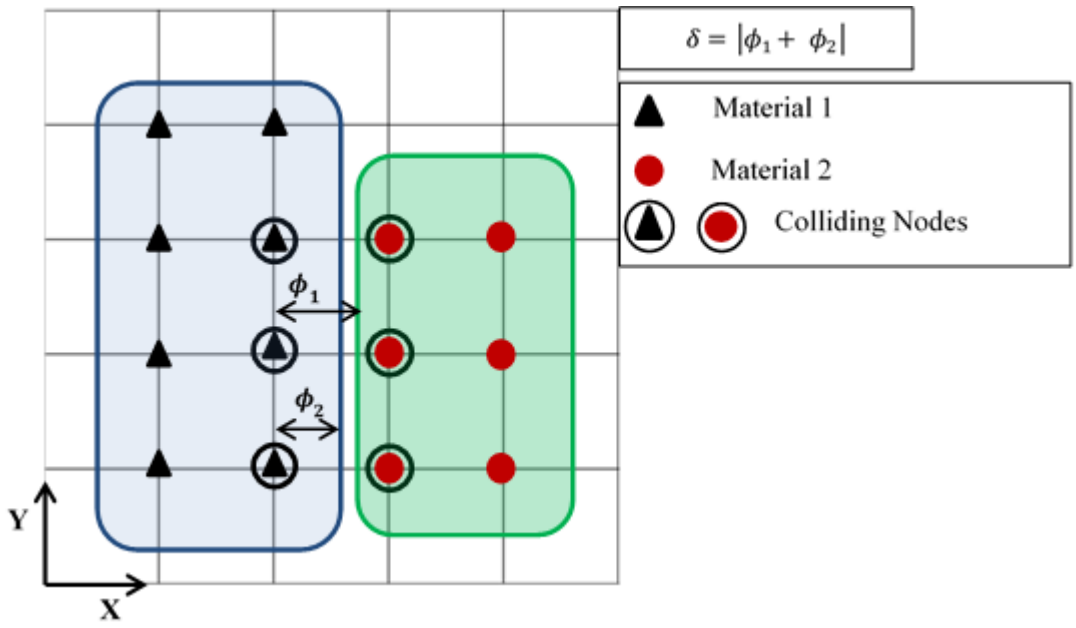


Figure 2-11: Collision detection procedure between two materials by calculating the relative distance $\delta$ between two materials using the level set function $\phi_1$ and $\phi_2$.

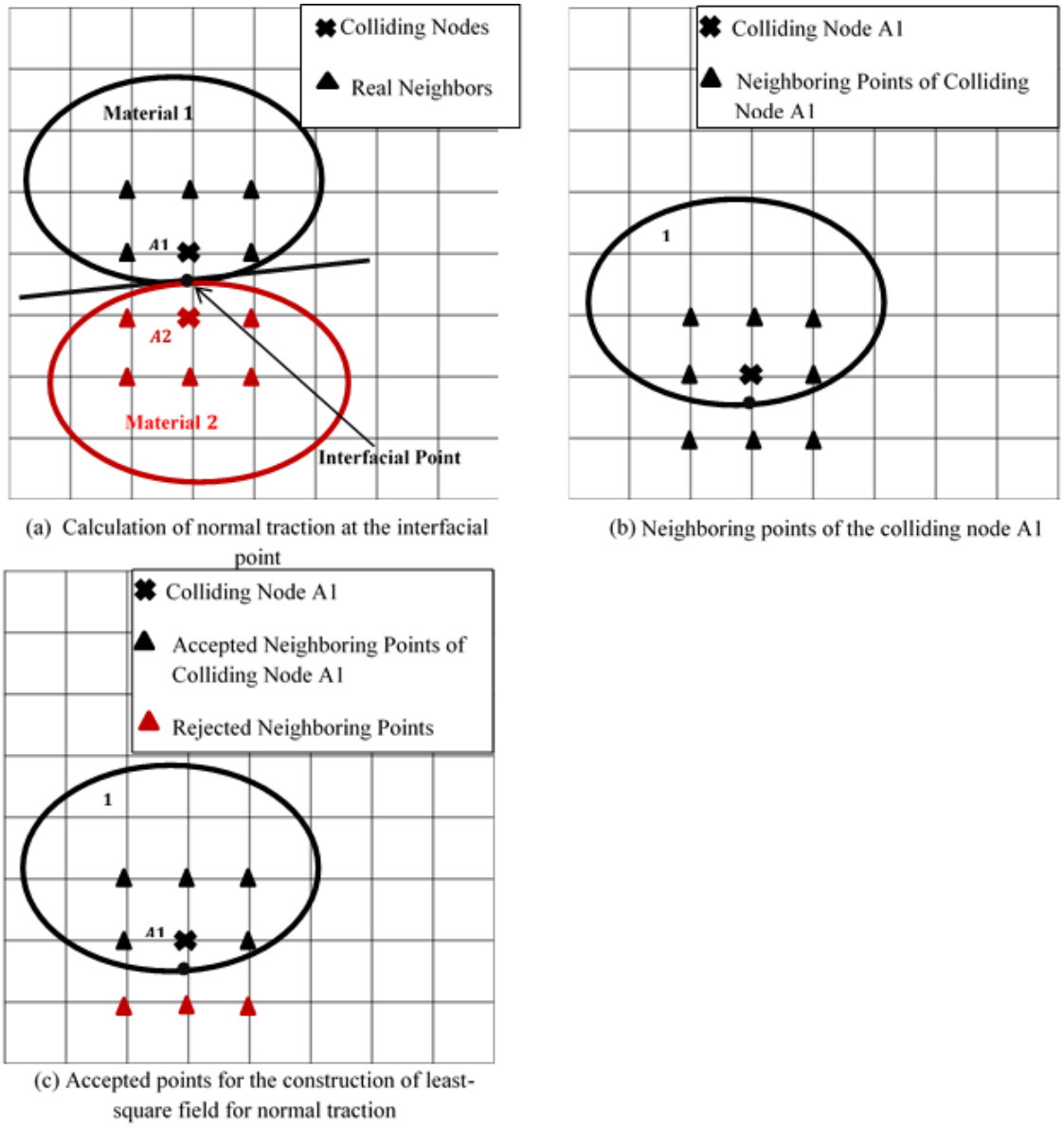


Figure 2-12: Procedure for the calculation of normal traction at the impacted interfaces between two materials using the least squares method.

# CHAPTER 3

# REACTIVE VOID COLLAPSE: EFFECTS OF CHEMICAL KINETICS, THERMAL DIFFUSION AND VOID-VOID INTERACTIONS

## 3.1. Introduction

In this chapter, the formation of hot spots due to void collapse in HMX crystals under shock loading is analyzed using mesoscale simulations. This study is aimed at modeling the interaction of shocks with voids followed by the formation of hot spots leading to ignition or quenching by thermal diffusion and other energy removal mechanisms. The numerical framework used in the current analysis is based on a massively parallel Eulerian based Cartesian based solver as explained in chapter 2. The current work follows the work of Kapahi and Udaykumar[58] where void collapse simulations were performed to understand various factors that can affect the hot spot temperature including void–void interactions. However, the analysis was performed considering HMX as an inert material. In present study, chemical reactions in HMX have been modeled using the Henson-Smilowitz chemical kinetic law[77]. The inclusion of the reactive flow model and heat diffusion effects in the current analysis helps to understand the interaction of the phenomena at the various time scales involved. A “go/no-go” criterion is determined for initiation at the mesoscale as a function of the shock strength and void-void interactions in a void field. The development of a “go/no-go” criterion is aimed to determine the critical shock speed and void arrangement for a given void size. It is demonstrated that the complex interactions of the physical mechanisms involved, the imposed shock characteristics (strength and pulse duration) and the void distribution all play key roles in determining the sensitivity of a heterogeneous explosive.

## 3.2.Results

This study is aimed at understanding the interactions among the various physico-chemical mechanisms involved in shock initiation in HMX. The interactions between elasto-plastic deformation and collapse of the void, thermal diffusion and chemical heat release is shown to lead to an ignition prediction criterion, i.e. a go/no-go criterion for initiation at the meso-scale. The ignition criterion is also shown to depend on various factors which can affect ignition such as shock strength, void arrangements and void volume fraction in HMX. The results obtained from the current analysis are categorized and presented in the following sections; in section 3.2.1, 3.2.2 and 3.2.3, the time scales of the interacting physico-chemical processes that influence initiation due to the void collapse mechanism are identified. Section 3.2.4 presents the analysis of a single void under shock loading combined with chemical kinetics. Section 3.2.5 then analyses the effect of thermal diffusion in determining a go/no-go criterion for ignition. The dependence of the initiation criterion on imposed shock strength is studied in Section 3.2.6. Following these analyses for single voids studies of void-void interactions and its implications for initiation sensitivity are performed in section 3.2.7. Finally, section 3.2.8 builds on the insights accumulated in the afore-mentioned studies to show that the distribution of voids in the energetic material can have significant effects on whether a shock of given strength leads to initiation. The results presented demonstrate that initiation in an energetic material depends in a rather complex way on several aspects of the meso-structure and loading conditions.

Depending on the size and strength of the hot spot, initiation of reaction can take place which can lead to ignition and growth of reaction front. However, depending on the time scale over which the local hot spot conditions are maintained, mechanisms such as heat diffusion and rarefaction can draw energy from the hot spot and may lead to quenching of reactions. The mechanisms of void collapse, reaction and heat diffusion operate at different time scales as discussed below. To clarify the interactions between the competing

mechanisms they are included in a stepwise fashion starting from the thermo-hydrodynamics of void collapse

### 3.2.1 Hydrodynamic collapse regime

This regime is characterized by hydrodynamic collapse of the void under the influence of a shock pulse. In the presence of voids in the matrix, shock loading results in large plastic deformation of the upstream surface of the void (i.e. the surface facing the shock pulse, see Figure 3-6(c)). The surface deformation culminates in a high speed jet in the material which impacts on the upstream surface of void leading to its collapse (Figure 3-6 (d)). The kinetic energy of the jet is converted into internal energy following collapse which leads to a significant rise in temperature in a localized zone Figure 3-6(d) or "hot spot". These hot spots acts as a favorable sites for the initiation of chemical reactions. The mechanism of hydrodynamic impact leading to void material jetting, collapse and energy conversions has been discussed in details in previous works [45, 56-58, 60].The time scale of the hydrodynamic impact and void collapse regime typically corresponds to the shock passage time over the domain and lies in the range of $10^{-9}$ seconds. For example, it was observed in previous work[58] that for a void of diameter $10\ \mu m$ in HMX matrix of size $30\ \mu m \times 30\ \mu m$, loaded with a $500\ m/s$ shock speed, void collapse takes place at approximately 8 nanoseconds.

### 3.2.2 Chemical reaction, ignition and growth regime

Hot spots may trigger chemical reactions in heterogeneous explosives depending on the maximum temperature reached at collapse. In the Henson-Smilowitz model implemented herein, chemical reactions are initiated with the initial endothermic transformation of solid β-HMX to solid δ-HMX. The δ-HMX further decomposes to ε-HMX and gaseous products . As the Henson-Smilowitz (H-S) model is based on Arrhenius rate laws, the time to ignition predicted by the reaction model depends on the initial temperature. In order to understand the dependency of the time to ignition on initial

temperature for the reaction model a study has been carried out which records the time to ignition for various initial temperatures. To illustrate the typical progression of ignition resulting from the H-S model, the chemical kinetics module was studied separately (i.e. without the flow computations) by supplying for an initial input temperature of $1100\ K$ to the chemistry module. The resulting species concentration behavior with time are shown in Figure 3-1. It can be seen from Figure 3-1(a) that at $1\ \mu s$ solid HMX (β-HMX and δ-HMX) decomposes completely to gaseous products and a significant rise in temperature is observed as shown in Figure 3-1(b). Hence, for $1100\ K$ initial temperature the time to ignition is about $1\ \mu s$.

Calculations of the chemical decomposition and heat release for a wide range of initial temperatures i.e. $800\ K - 1800\ K$ similar to the 1100K case shows the time to ignition for various initial temperature in Figure 3-2. The time to ignition is very sensitive to the initial temperature and varies from milliseconds to nanoseconds. In the context of void collapse, the initial temperature for reaction corresponds to the hot spot temperature which dictates initiation and ignition in HMX. If the hot spot temperature is high enough, i.e. above $1400\ K$ then reaction can initiate in the nanoseconds time range; however, if the hot spot temperature lies below $900\ K$ the reaction will occur at the time scale of milliseconds. Therefore, in light of the influence of thermal diffusion (discussed below) and other mechanisms (e.g. rarefaction waves) that drain energy from a hot-spot the maximum temperature at the collapse of a void is an important factor in determining initiation of runaway chemical reactions.

### 3.2.3 Thermal diffusion regime

As shown in the previous section, time to ignition in HMX depends strongly on the hot spot temperature. For temperatures below $900\ K$, it is observed that time to ignition lies in the milliseconds range. In this range, it is expected that thermal diffusion may play a crucial role in quenching of the hot spot. The importance of thermal diffusion on ignition

can be estimated by estimating the diffusion time scale $l^2/\alpha$, where $l$ is the characteristic length scale of the problem and α is the thermal diffusivity of HMX. For the hot spot $l$ is of the order of μm and the corresponding diffusion time scale will lie in the range of milliseconds.

The times scales of collapse, chemical reactions and thermal diffusion-are illustrated in Figure 3-3. It is interesting to note that if the hot spot temperature is greater than $1400\ K$ ignition can take place in the hydrodynamic impact regime i.e. in the range of nanoseconds, i.e. the collapse and reaction time scales lie in the same range. Hence, the initiation of chemical reaction follows hard on collapse of the void with significant rise in temperature; in such an event thermal diffusion will not play a role since the time scale for diffusion is milliseconds. However, if the hot spot temperature is below $900\ K$ where ignition time is of the order of milliseconds then thermal diffusion can play an important role and can draw the energy from hot spot which eventually leads to smearing of the local energy maxima. Therefore, the interplay of the three time scales indicated in Figure 3-3 will determine whether a particular hot spot goes critical; this point will be further developed in the following sections.

### 3.2.4 Single void collapse: formation of reactive hot spot in the absence of thermal diffusion

The characterization of the three interacting processes and associated time scales in void-collapse induced hot spot formation is now performed using void collapse of a single cylindrical void of radius $5\ \mu m$ in HMX matrix of domain size $30\mu m \times 30\ \mu m$ under shock loading. The problem setup is shown in Figure 3-4. The shock loading is applied from the west face of the domain boundary, where the particle velocity is imposed at 500 m/s with a pulse duration of 4 nanoseconds. In the first case, thermal diffusion is not included in order to analyze the relationship between reaction initiation and the hot spot temperature formed due to void collapse.

A grid convergence study for this problem is presented in previous work [58]. However, the previous analysis was done on an inert HMX material. In the current analysis, the grid convergence study for the reactive void collapse problem has been performed for four different grid sizes of $\Delta x = 0.06\,\mu m,\ 0.05\,\mu m,\ 0.0375\,\mu m$ and $0.03\,\mu m$. The time to ignition in HMX matrix predicted by the chemical reaction model after the formation of a hot spot is used in the grid convergence study (Figure 3-5). It can be seen from Figure 3-5 that the time to ignition converges to 0.3 milliseconds as the grid is refined to $\Delta x = 0.03\,\mu m$. Henceforth, a grid size of $\Delta x = 0.03\,\mu m$ is used for the analysis in the present work.

The computed hot-spot temperatures are shown in Figure 3-6 at various instants during hot spot formation. It is observed that collapse of the void results in the formation of a hot spot with a maximum temperature of $950\,K$ in the domain. Also, the collapse of the void leads to the generation of a shock wave from the collapse zone as shown in Figure 3-6(d). The time scale involved in this process is of the order of nanoseconds, which is too short a time for reactions to set in at the hotspot temperature of 950K (see Figure 3-2). Hence, the simulation is continued beyond the collapse process; ignition is then observed at 0.3 milliseconds as shown in Figure 3-6(f).

### 3.2.5 Single void collapse in the presence of reaction and diffusion

In the previous case, thermal diffusion was not included; ignition was obtained at 0.3 milliseconds, i.e. on the time scale over which thermal diffusion is expected to play a role. In order to understand the effects of diffusion, the above simulation is conducted again with the diffusion terms turned on in the governing equations. The temperature contour plots in this case are shown in Figure 3-7 and can be compared with Figure 3-6 for the case without diffusion. It can be seen from Figure 3-7(f-g) that after the formation of hot spot,

diffusion transports away the localized energy from the hot spot and smears out the temperature field; no ignition is obtained in this case.

### 3.2.6 Prediction of ignition for different shock strengths

As shown above, for a loading strength corresponding to $V_0 = 500\ m/s$, initiation is not obtained due to quenching by thermal diffusion. It was discussed in section 3.2.2 that for high hot spot temperatures, i.e. above $1400\ K$, the reactive time scales are in the nanosecond range. For higher shock strengths, higher hot spot temperatures can be expected due to the higher speeds of jet impact during void collapse; this can lead to initiation of HMX. To examine the effect of shock strength, a simulation with $V_0 = 800\ m/s$ is attempted for the same void size of $10\ \mu m$ diameter and shock pulse duration. The temperature contour plots for $800\ m/s$ shock loading at different time instants during the collapse of the void is shown in Figure 3-8. It can be seen from Figure 3-8 that as the void collapses the hot spot temperature is sufficient to initiate the chemical reaction in HMX. The reaction front eventually grows from this reactive hot spot location as shown in Figure 3-8(c-g) leading to ignition in the other parts of the domain. The ignition is also characterized by the complete decomposition of solid HMX to gaseous products. The concentration of solid $\beta - HMX$ and $\delta - HMX$, along with gaseous product HCN at 11.6 μs is shown in Figure 3-9. For this higher shock strength of $V_0 = 800\ m/s$, initiation of chemical reaction takes place in the nanoseconds time range and diffusion is unable to quench the chemical heat release from the hotspot leading to initiation of the material.

Based on the observations from the shock simulations of an isolated void with the two shock strengths defined by $V_0 = 500\ m/s$ and $800\ m/s$ , it can be deduced that a critical shock strength for initiation could lie between the two values investigated. Hence, to establish an ignition criterion for the current problem of void size of $10\ \mu m$ diameter, two intermediate shock strength values, i.e. $V_0$ of $550\ m/s$ and $650\ m/s$ were simulated.

The value of shock strength for which initiation occurs yields a criticality condition or a go/no-go criterion for the specified void size.

To identify whether ignition occurs for a particular shock strength the total normalized specific internal energy, ΔE in the domain (shown in Figure 3-10) was recorded at each time instant and is used as a threshold measure for ignition characterization. This value is computed as follows:

$$\Delta E = \frac{e_t - e_\infty}{e_\infty} \tag{3.58}$$

where, $e_t$ is the total specific internal energy in the domain given as:

$$e_t = \frac{\int_V \rho e \, dV}{\int_V \rho \, dV} \tag{3.59}$$

$\rho$ is density, $e$ is specific internal energy and $V$ is the total volume of the domain.

$e_\infty$ is the total specific internal energy of the domain at ambient temperature of $T_\infty = 298\ K$ and given as:

$$e_\infty = \frac{\int_V \rho C_v T_\infty \, dV}{\int_V \rho \, dV} \tag{3.60}$$

$C_v$ is specific heat at constant volume. Therefore, ΔE is a measure of the excess specific internal energy in the domain due to the imposition of the load. The variation of ΔE with time is shown in Figure 3-10. It can be seen that for $V_0$ values of $500\ m/s$ and $550\ m/s$ , the hot spot is diffused and the value of the internal energy eventually settles down to the bulk value of the domain, i.e. corresponding to that of a homogeneous material. However, for higher shock strengths $V_0$ =of $650 m/s$ and $800\ m/s$, the hot spot temperature is high enough to initiate chemical reaction leading to ignition in a few nanoseconds and diffusion does not play a significant role in removing energy from the hot spot. The above simulations therefore establish a threshold for initiation of HMX in the vicinity of a void.

### 3.2.7 Effect of void-void interactions on shock initiation

In the case of a single void, it was observed that when the void collapses under the shock load, a secondary wave emanates from the collapsed zone as shown in Figure 3-6(d). In heterogeneous explosives, due to the presence of multiple voids in the domain, this secondary wave from the collapse of one void can affect the collapse of the surrounding voids by interacting with the incident shock or the secondary waves from the other voids; These effects were studied in the case of void collapse in an inert material in previous work[58]. It was observed that relative positioning of voids with respect to each other can affect the collapse temperatures of downstream voids. For example, in the case when voids are arranged in tandem fashion with respect to the incident shock wave, the void which is downstream experiences "shielding" from the void present in front of it, and for the offset arrangement of voids the collapse of the front void sets off a secondary shock wave upon collapse that causes "reinforcement" of the incident shock and leads to higher collapse temperature of the downstream void[58]. Thus, it is likely that the presence of voids in the neighborhood can shift the criticality condition for initiation in a heterogeneous energetic material. To examine this possibility, the current numerical framework has been used to study the effect of void-void interactions on ignition and growth of chemical reaction. Two different void configurations have been considered, as shown in Figure 3-11. In the first arrangement (Figure 3-11(a)), two voids are positioned in-line with a horizontal gap of 0.5D and in the second arrangement (Figure 3-11(b)) voids are offset, separated by a horizontal gap of 0.5D and vertical offset of 0.5D. The void sizes are the same, as in the single void simulations, i.e. D=10 $\mu m$. A shock with $V_0 = 550\ m/s$ is applied from the west face of the domain boundary and the shock pulse duration is 4 nanoseconds for all the void configurations.

3.2.7.1 Tandem voids

Shock analysis on tandem voids (Figure 3-11(a)) is performed for loading with $V_0$= $550\ m/s$; the temperature contour plots at different time instants are shown Figure 12. It can be seen that shock loading leads to the collapse of both the voids and formation of hot spots. After the shock wave passes, the two hot spots persist in the domain for $2.6\ \mu s$ until diffusion smears out the local temperature zone leading to extinction. The diffused hot spots are shown in Figure 3-12(f-g). In this case the temperature of the hot spot or the local energy excess was not sufficient to initiate sustained chemical reactions.

For the same shock loading of $550\ m/s$ and 4 nanosecond pulse duration for a single void of $10\ \mu m$ diameter no reaction and ignition was observed (Figure 3-10). Based on this observation, in the tandem void situation it is to be expected that the first void which interacts with the prescribed shock wave will not ignite. Also, if a void is downstream in the same line to the first void with respect to the shock wave, the downstream void experiences "shielding" from the void present in front of it and should not ignite as well. The shielding of shock wave strength for the secondary void can be seen from Figure 3-12(c-d). The observations regarding tandem voids from the previous work[58] is consistent with the current analysis.

3.2.7.2 Offset voids

The configuration of the voids is now changed, so that the downstream void is arranged (Figure 3-11(b)) with 0.5D offset value and loaded with the same prescribed shock load corresponding to $V_0$= $550\ m/s$ speed and 4 nanosecond pulse. The temperature contours are shown in Figure 3-13. In an offset void situation, the shock wave leads to the collapse of both the voids and formation of hot spots as in the tandem case. However, here the hot spot obtained from the collapse of the downstream void leads to initiation of chemical reaction and ignition in HMX. The hot spot strength of the downstream void is therefore sufficient for the initiation and growth of chemical reaction. Note that for the

given void diameters and shock loading a single void or tandem void configuration did not lead to reaction initiation and ignition. This can also be seen in the current simulation from the interaction of the first (upstream) void with the incident shock wave, shown in Figure 3-13(c). The shock load leads to the collapse of the void but no reaction is observed. However, collapse of the first void generates a secondary shock wave, as shown in Figure 3-13(d). This secondary wave strengthens the incident shock wave on the downstream offset void. The strengthened shock wave interacts with the void present downstream leading to initiation of chemical reaction, ignition and reaction growth in the domain. Thus, the presence of multiple voids can initiate reactions where none exist in the presence of an isolated void provided the voids have a suitable relative arrangement. In fact, previous work [58] with inert voids indicated that there is an optimal relative arrangement of two voids that maximizes the likelihood of initiation.

#### 3.2.7.3 Ignition threshold criterion for void arrangements

The above shock analysis of tandem and offset void arrangements shows the importance of relative positioning of voids on initiation of reaction and initiation in an energetic material. The strengthening of the incident shock wave causes the reaction initiation in 0.5D offset void arrangement. However, if the voids are offset by a large distance it is expected that the collapse of one void will not affect the other one in the domain. Therefore an optimal offset is likely to exist. To understand the effect of the offset on reaction initiation, a study is performed which is aimed to develop an ignition threshold criterion based on the offset value of the voids. Two other offset arrangements have been considered with different offset values of D and 2D.The horizontal gap of 0.5D has been used for all void arrangements and the shock loading is also same for all the simulations.

The variation of $\Delta E$ (equation (2.1)) with time for different void arrangements with offset values of 0, 0.5D, D and 2D is shown in Figure 3-14. The zero offset value corresponds to the tandem void situation where no reaction was observed for the given

shock load. This can be seen from Figure 3-14, as the internal energy for the tandem void becomes constant after impact has ensued and the incident shock pulse has passed. The same behavior is observed for the situation when the voids are separated by the offset value of 2D. In this situation, the voids are too far apart and the collapse of the first void does not affect the collapse of the second offset void. For the offset values of 0.5D and D, the strengthening mechanism of the shock wave leads to reaction initiation. This can be seen from significant rise in internal energy as shown in Figure 3-14 for these two offset arrangement. These results therefore indicates a threshold criterion for ignition in HMX based on different void arrangements which can be present in an explosive microstructure.

### 3.2.8 Shock initiation in HMX with void volume fraction of 10%

The microstructure of heterogeneous explosives contains various heterogeneities in the form of randomly distributed voids, microcracks etc. and void-void interaction can influence its shock sensitivity. The insights provided by the void-interaction studies above can now be applied to understand the effect of porosity distribution in an idealized sample of void-containing energetic material. In order to study the effects of void-void interaction in heterogeneous explosives, shock analysis in HMX with 10% void volume fraction has been conducted in the following. Two different void distributions are considered, one with a regular distribution pattern and the other with a random distribution, both at 10% void fraction.

#### 3.2.8.1 Regular distribution

The regular pattern of voids is shown in Figure 3-15 where the voids in the domain are numbered from 1-9. The domain size is $0.1\ mm \times 0.1mm$ and void volume fraction is 10%. The void diameter used in this analysis is $10\ \mu m$ as before. Shock loading of $V_0 = 550\ m/s$ is applied from the west face of the domain for 4 nanoseconds duration. Figure 3-16 Since the voids in this regular pattern are arranged in a tandem fashion, based on the

observations from void-void interactions the shielding effect is expected. The shielding is experienced most strongly by voids 7, 8 and 9 and for the applied shock load these voids do not collapse completely. The shock energy is attenuated by the collapse of voids 1, 2 and 3. The attenuation of the incident shock leads to low collapse temperatures for voids 4 and 6. It is interesting to note that void 5 also did not collapse; void 5 experiences shielding not only from void 2, but also from voids 1 and 3. The same is observed for void 8 and the deformation for void 8 is less than voids 7 and 9, although they are arranged in the same vertical line. Due to the presence of shielding, no ignition is observed in this case.

3.2.8.2 Random distribution

The above regular arrangement of voids in tandem fashion shows the pronounced effect of shielding and no ignition is obtained. It was observed in section 3.2.7 that when voids are arranged with some offset, reaction can be triggered. If voids are randomly distributed it may be expected that reaction can be triggered for the same shock strength as applied previously. Hence, the void volume fraction of 10% is randomly distributed in a HMX matrix with the initial configuration shown in Figure 3-17. The shock loading and void size is the same as for the regularly distributed voids case. In this randomly distributed configuration, void 1 and 2 are offset from each other. In the same way voids 2, 6 and 7 are also offset from each other. The offset voids 2, 4, 6 and 7 can acts as potential sites to trigger ignition based on previous observations. However, Voids 3, 5 and 8 are arranged tandem and voids 5 and 8 can experience a shielding effect. The temperature contour plot obtained from the simulation is shown in Figure 3-18. From Figure 3-18(c), it can be seen that void 2 experiences secondary shock effect from void 1 which enhances the original shock wave and triggers the reaction and eventually ignition at the hotspot. The same applies for void 6 which experiences secondary wave effect from void 2 and reaction triggers at void 6 as shown in Figure 3-18(e). Void 4 shown in Figure 3-18(f) experiences secondary shock effects from both voids 2 and 3 and the hot spot temperature is sufficient

to initiate reaction. The reaction front grows from voids 2, 4 and 6. As the shock passes by void 1, it leads to the formation of a hot spot locally. However, the hot spot strength was not sufficient to ignite on its own. Once the reaction front from hotspot 2 grows and interacts with the hotspot at position 1, it increases the strength of the hot spot at void 1 and void 1 ignites as well. This shows the growth of the reactive zone as the initial reaction front interacts with other hot spots in the domain. Note that Voids 5 and 8 experience shielding effects from void 2 as all three are arranged tandem and no reaction was observed at these locations. Thus, in order to predict the sensitivity of a heterogeneous energetic material the characterization of both void fraction field as well as relative location of void spaces in the material may be necessary.

## 3.3. Conclusions

The numerical framework is used to simulate the void collapse phenomenon leading to formation of hot spot and initiation of chemical reactions under the influence of shock loading. Three different physical processes are involved in the complete chain of events from void collapse to initiation of chemical reaction. First, the shock wave interaction with a void leads to its collapse and formation of hot spots; this is characterized as hydrodynamic regime; the time scale of this mechanism corresponds to the shock passage time i.e. nanoseconds. Following the formation of hot spots, chemical reaction may be initiated depending on the temperature of the hot spot; this phase is characterized as chemical reaction regime. The time scale for the chemical reaction varies from milliseconds to nanoseconds depending on the hot spot temperature. If the hot spot temperature is not sufficiently high, heat diffusion can extract energy from the hot spot and quench the hot spot. Since heat diffusion acts on times scales of milliseconds, for high hot spot temperatures chemical reactions may be initiated at too short a time scale to lead to quenching, i.e. the runaway chemical heat release may be well underway before diffusion can act. The interplay of the three processes at different time scales was shown in this work

to lead to a go/no-go criterion that can be predicted through simulations for HMX under shock loading.

Simulations were performed to study the interactions amongst voids in a multiple void situation. It is shown that the relative positioning of voids with respect to each other can affect the post shock hot spot temperature and therefore reaction initiation. If the voids are arranged in tandem with respect to the incident shock, the void downstream of the shock experiences a shielding effect and lower collapse temperature. However, if the voids are present in offset arrangement and if the offset distance lies in a certain range, then the incident shock is strengthened by a secondary wave which emanates from the collapse of the first void which leads to high collapse temperature and initiation of chemical reaction at the downstream void. An ignition threshold was obtained for a given shock strength based on the arrangement of the voids.

There are several limitations of the above presented study, including the restriction of void shapes to cylindrical geometries in a 2D setting. The modeling of the HMX material following ignition, i.e. when the hot spot consists of a gas-solid mixture or later in the reaction growth process when it is comprised primarily of gas, has not been rigorously performed; therefore, material behavior beyond ignition will require a full multiphase mixture treatment that is beyond the scope of this work. Therefore, the regime for which the current study applies consists mainly of the initiation phase of chemical reactions. The chemical kinetics model and material model for HMX are other elements that require more rigorous treatment and need to be improved once such models become available. Despite these limitations, the study provided insights into the role of various time scales involved in the void collapse phenomena in energetic materials. The framework allowed for quantification of sensitivity as a function of shock speed and void fraction and demonstrated the characterization of a go/no-go criterion based on meso-scale simulation of a heterogeneous energetic material. Furthermore, shock speeds and relative void positions in the sample were identified as important factors that contribute towards

increasing the sensitivity of energetic materials. However, there are other factors which can also contribute to the shock initiation in heterogeneous explosives such as shock pulse duration, void size, void shapes etc. The role of each of these factors in shock initiation is being examined in ongoing work.

Table 3-1: Parameters for the Johnson Cook Material Model[86] and Mie-Grüneisen E.O.S.[86] for HMX.

| Material | $\rho_0$ $(Kg/m^3)$ | $C$ $(J/kg-K)$ | $\Gamma_0$ | $c_0$ $(m/s)$ | $s$ | *Thermal Diffusivity* $\alpha\ (m^2/s)$ | *Yield Stress, Y(MPa)* |
|---|---|---|---|---|---|---|---|
| HMX | 1860 | 1000 | 1.1 | 2650 | 2.38 | $1.1\times 10^{-7}$ | 260 |

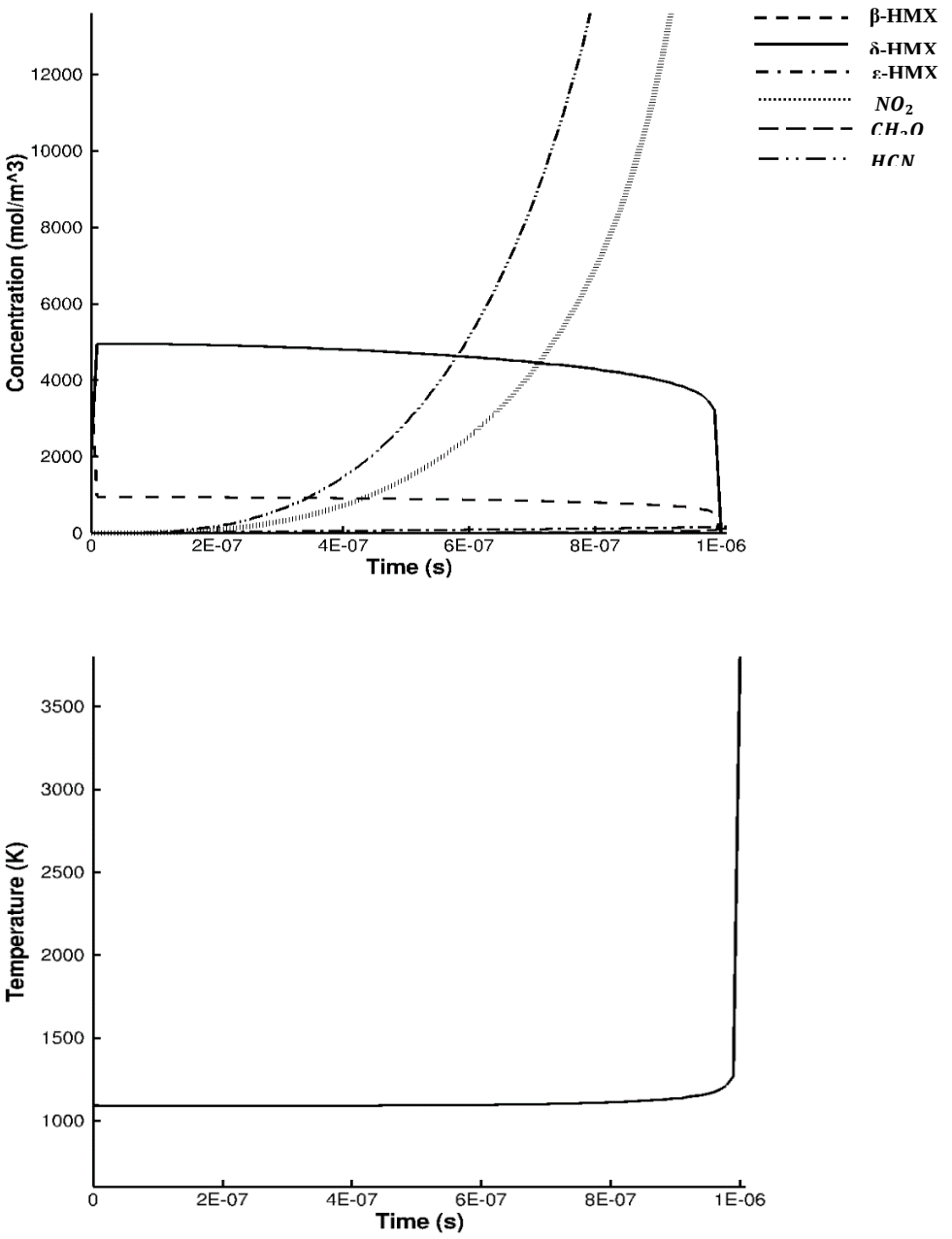


Figure 3-1: Response of Henson-Smilowitz reaction model to an initial temperature of 1100 *K*. (a) Variation of species concentration with time showing complete decomposition of solid HMX to gaseous products leading to ignition (b) Variation of temperature with time showing rise in temperature because of ignition.

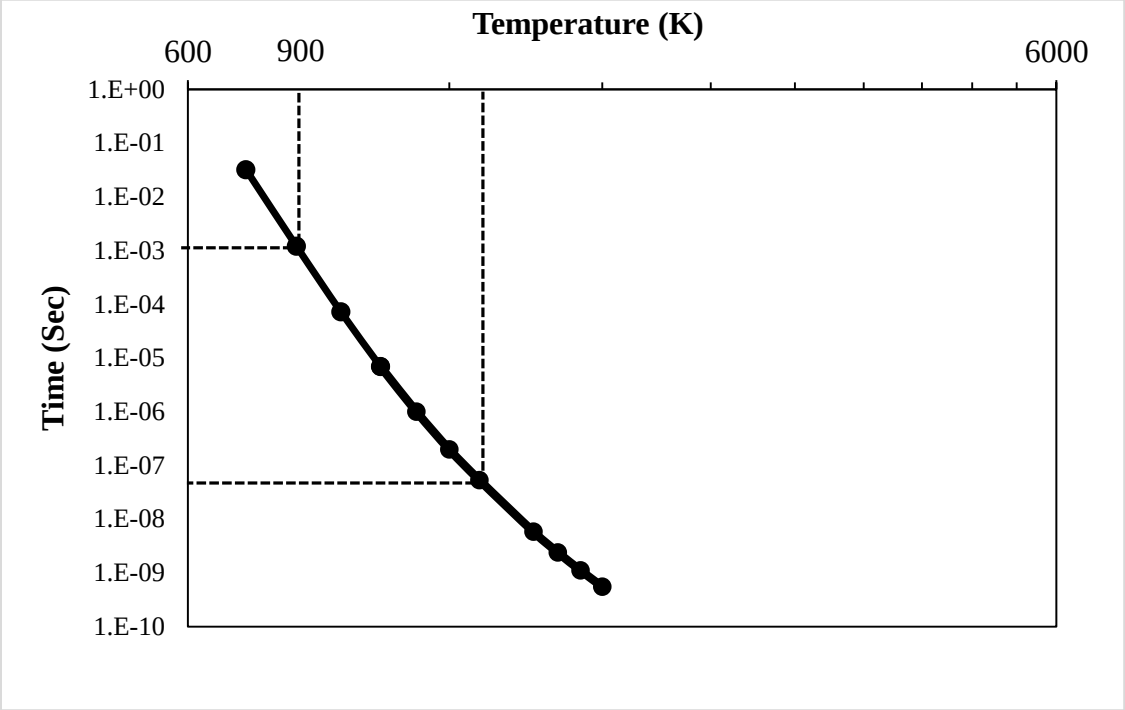


Figure 3-2: Plot of variation of time to ignition predicted by the Henson-Smilowitz model for initial temperature range of 800 *K* – 1800 *K*. The time to ignition varies from milli-seconds to nanoseconds for the given temperature range.

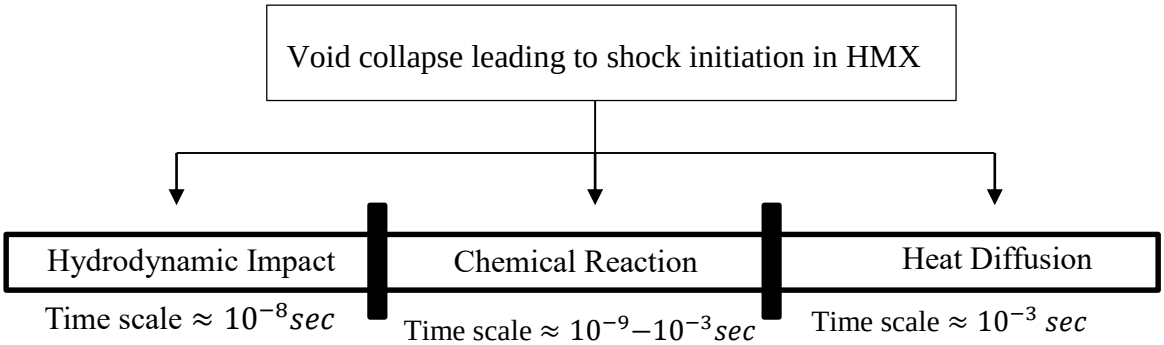


Figure 3-3: Void collapse mechanism leading to initiation of chemical reaction in HMX involves three different physical processes hydrodynamic impact on voids, chemical reaction kinetics and ignition and heat diffusion. These processes operates at different time scales.

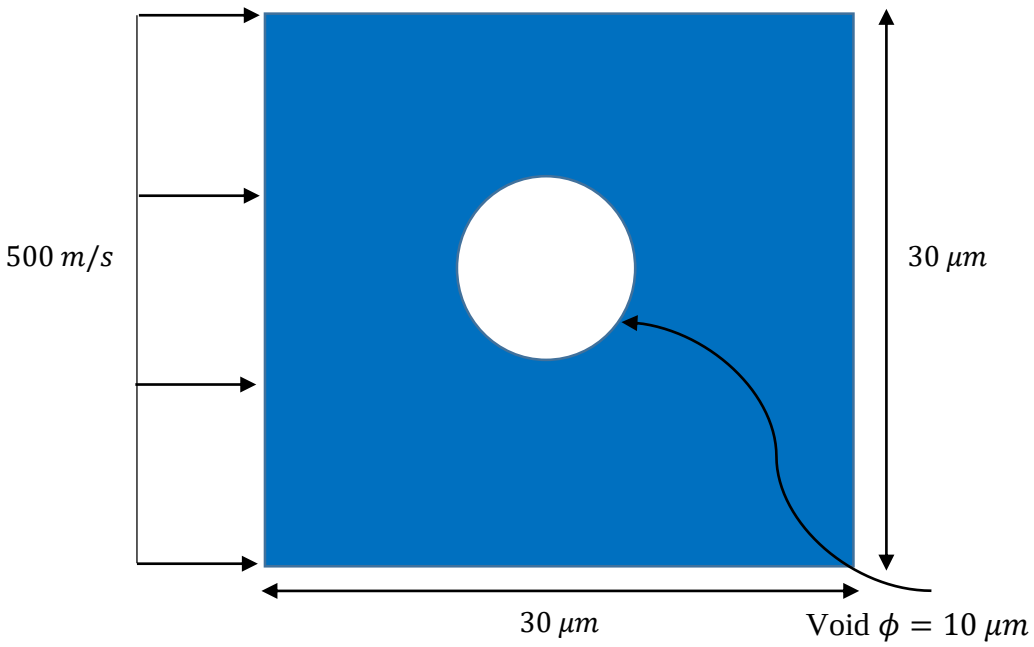


Figure 3-4: A cylindrical void of radius 5 µm embedded in an HMX matrix of size 30 µm × 30 µm. Shock loading of strength 500 *m/s* is applied from the west boundary of the domain.

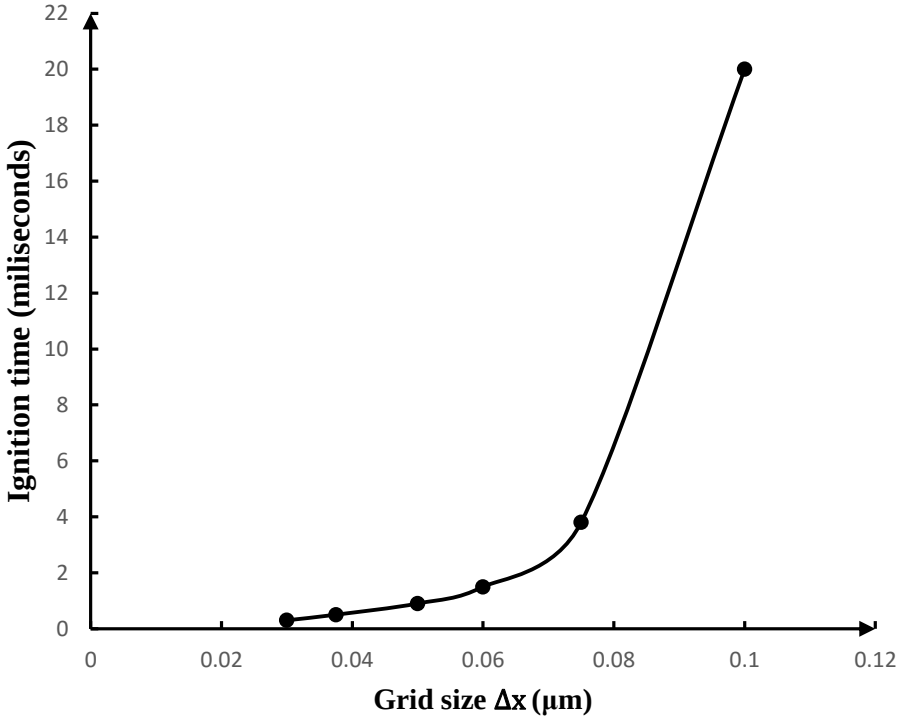


Figure 3-5: Grid convergence study of ignition time for a single void collapse with shock loading of 500 m/s. The results is shown for six different grid sizes of 0.1 μm, 0.075 μm, 0.06 μm, 0.05 μm, 0.0375 μm and 0.03 μm.

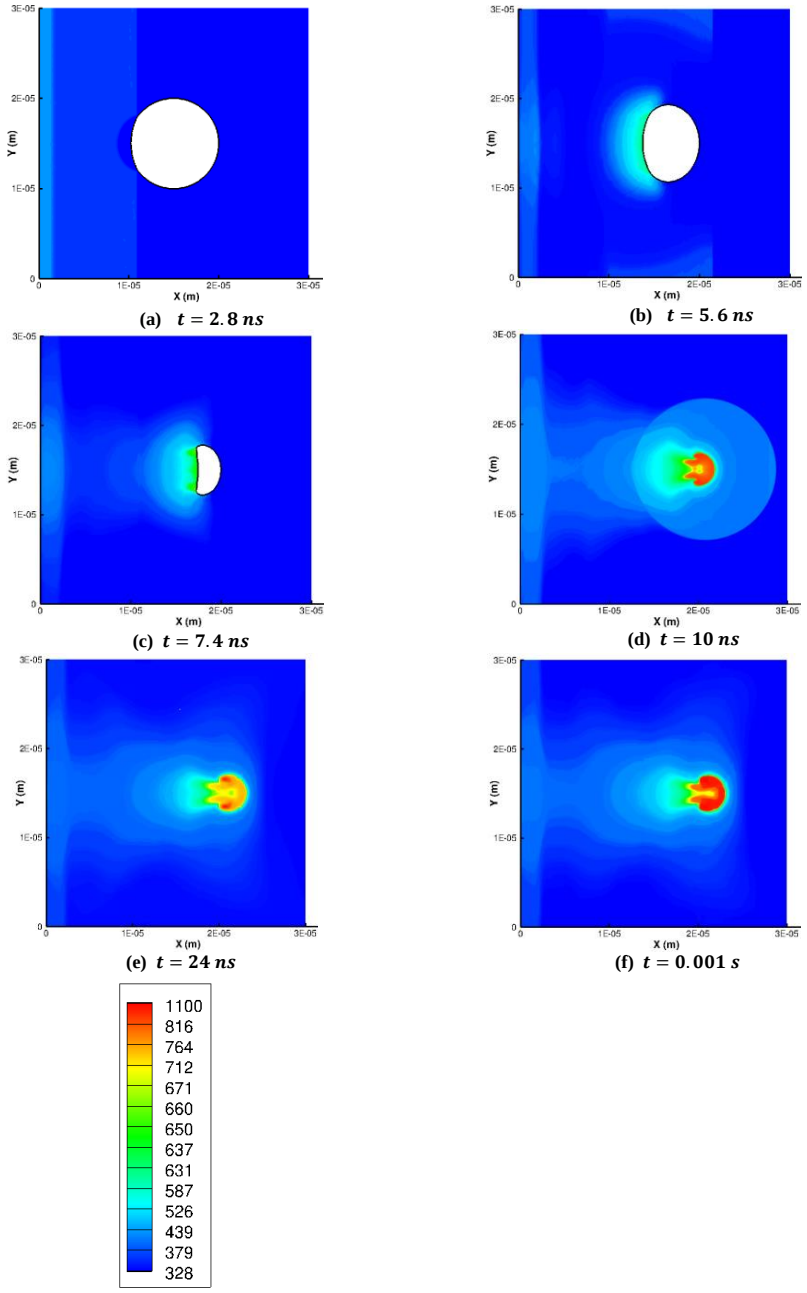


Figure 3-6: Temperature (K) contours for different stages of void collapse phenomenon showing reaction at late stage (f) for a shock loading of 500 m/s. The domain size is 30 μm × 30 μm.

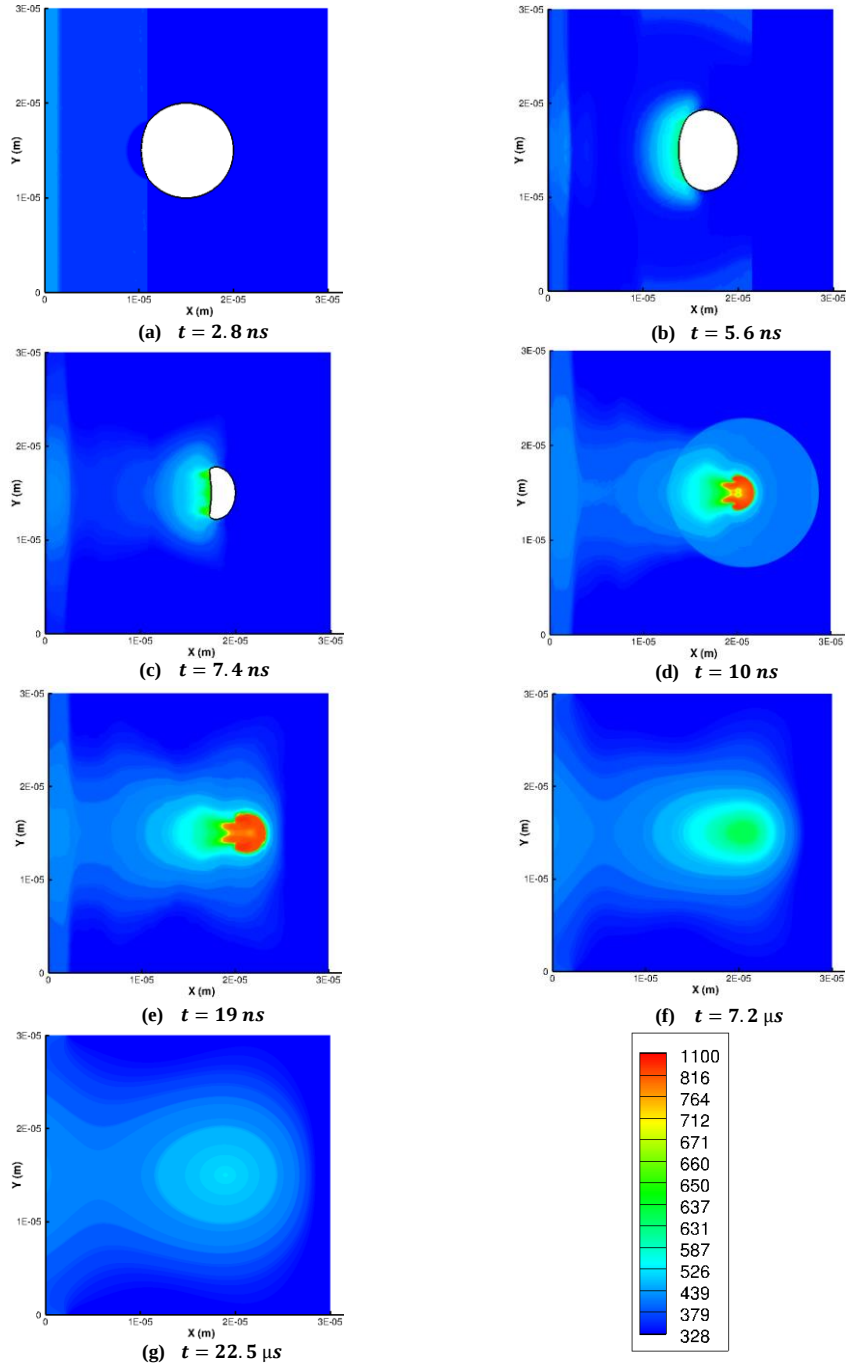


Figure 3-7: Temperature (K) contours for different stages of void collapse phenomenon with diffusion being modeled for a shock loading of 500 m/s. The domain size is 30 µm × 30 µm.

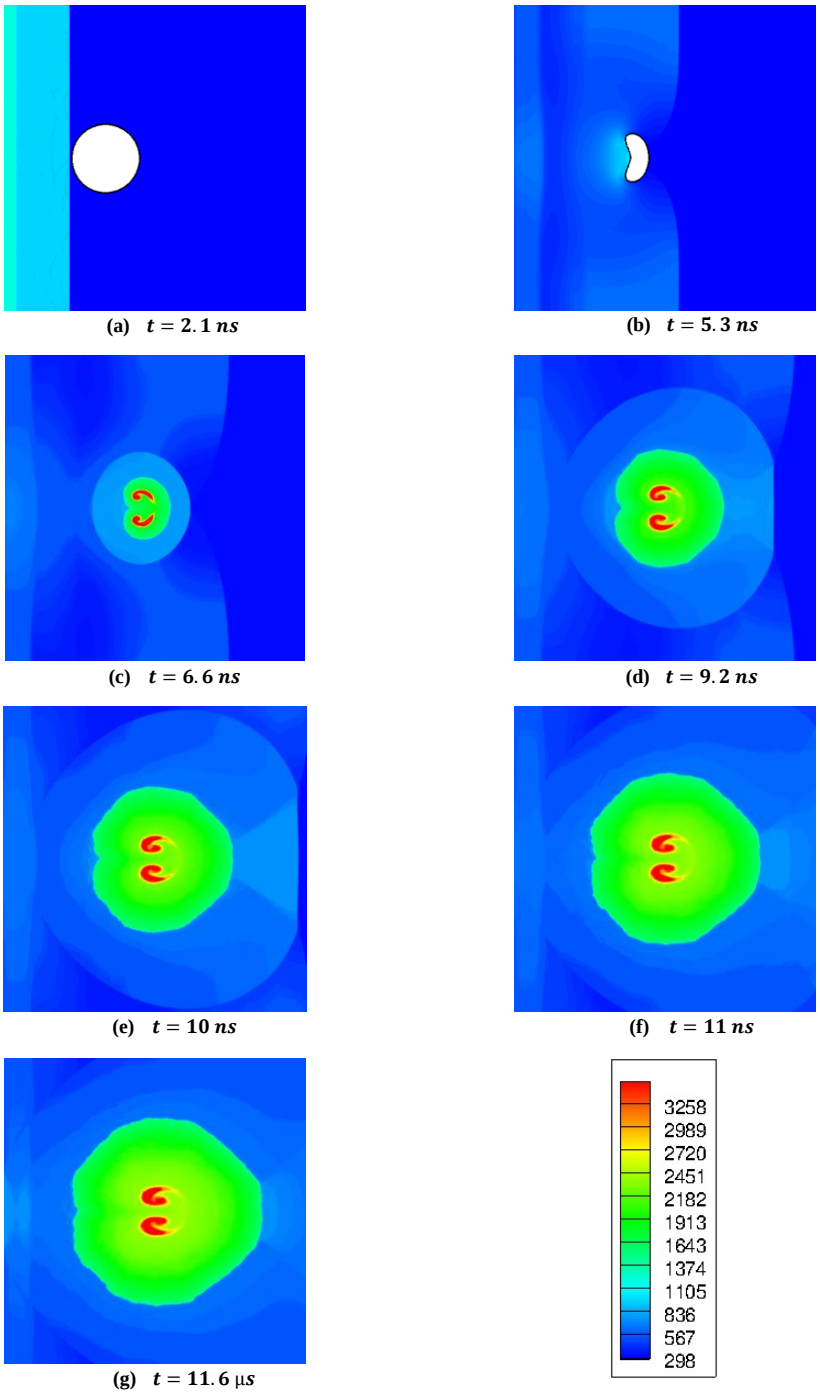


Figure 3-8: Temperature (K) contour for different stages of void collapse phenomenon for shock loading of 800 m/s. The domain size is 45 µm × 45 µm. Contours show the ignition and growth of chemical reaction in the domain.

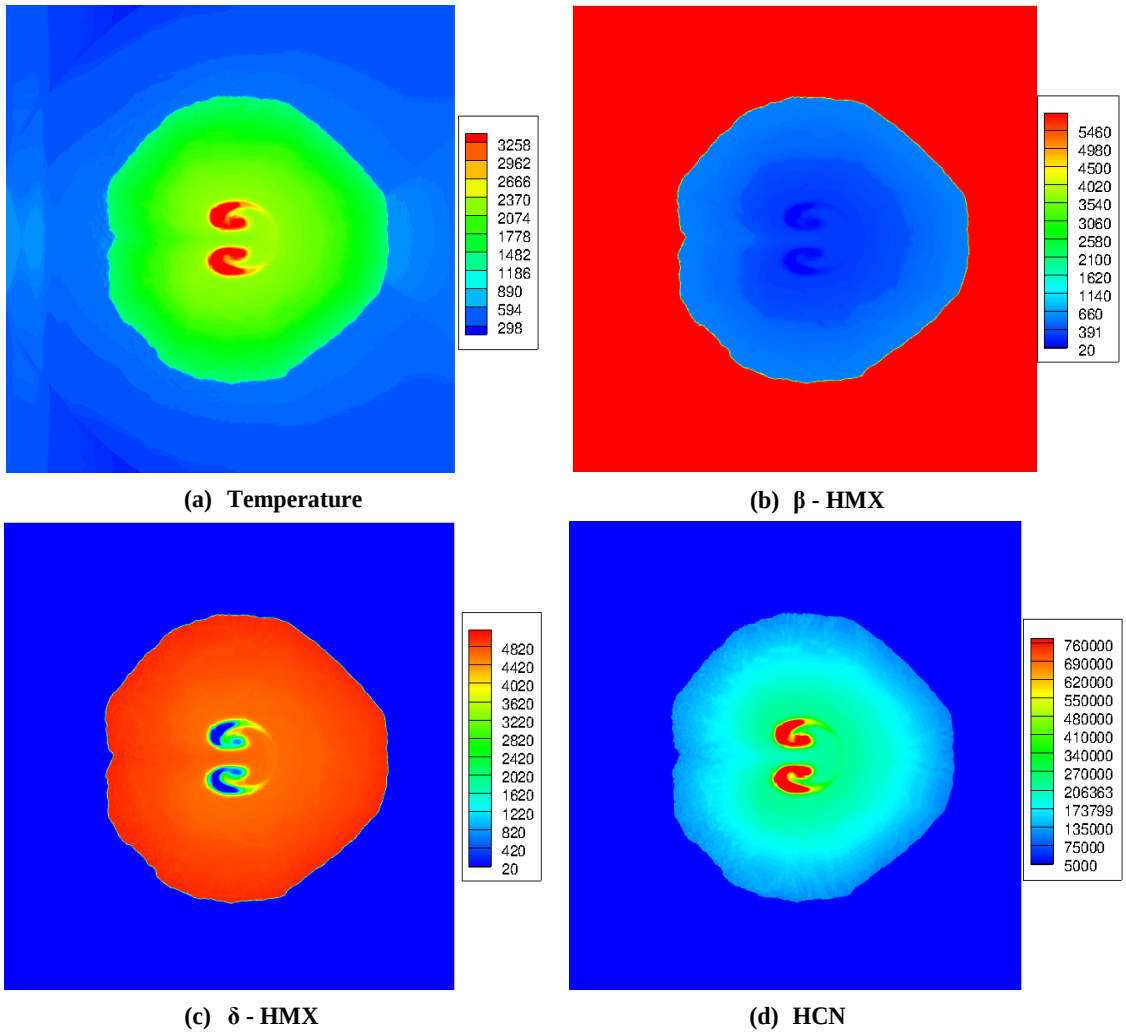


**(a) Temperature** **(b) β - HMX**

**(c) δ - HMX** **(d) HCN**

Figure 3-9: Temperature (K) and species ($mol/m^3$) concentration at 11.6 μs for shock loading of 800 m/s. Contours shows the ignition and growth of chemical reaction in the domain.

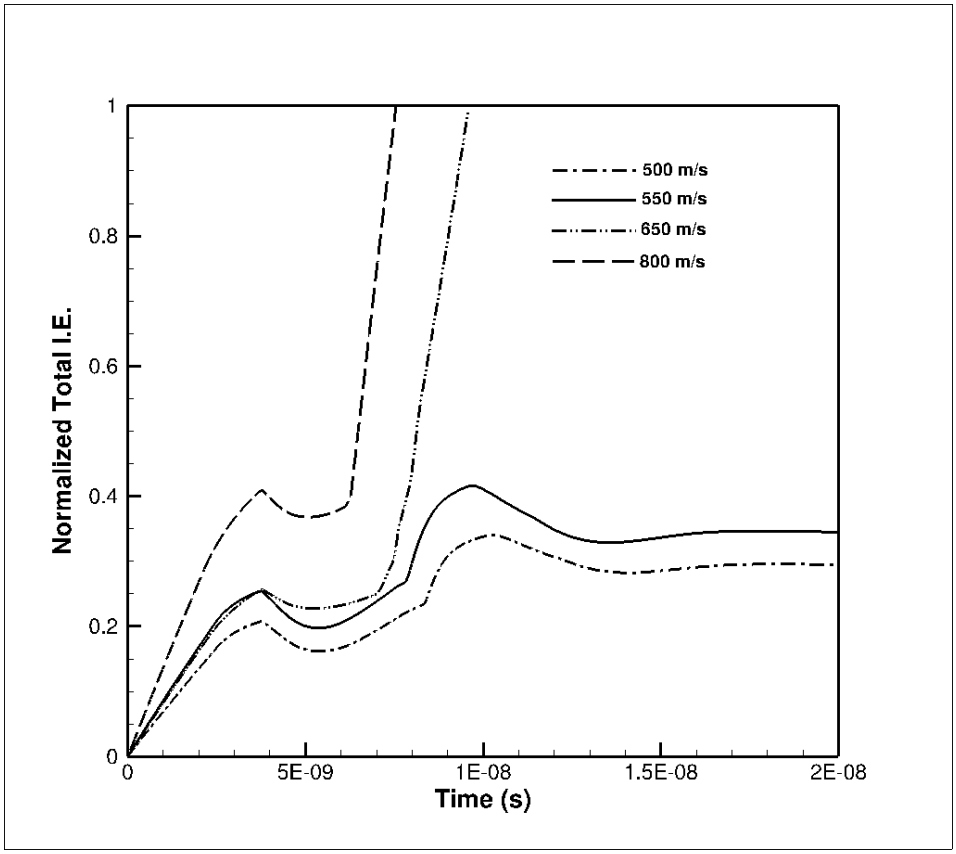


Figure 3-10: Variation of normalized total specific internal energy with time for shock speed of 550 m/s, 550 m/s, 650 m/s and 800 m/s showing ignition for the 650 m/s and 800 m/s.

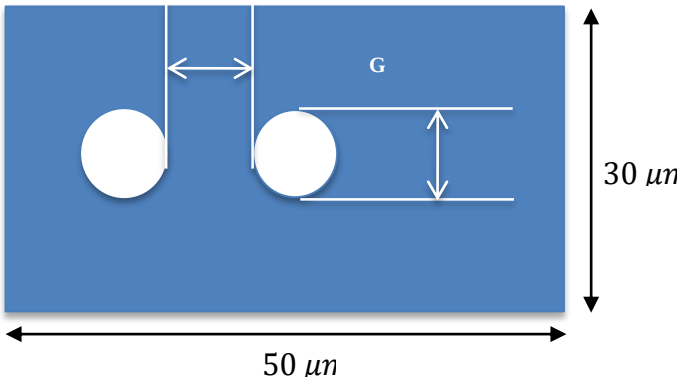


(a) Inline Voids

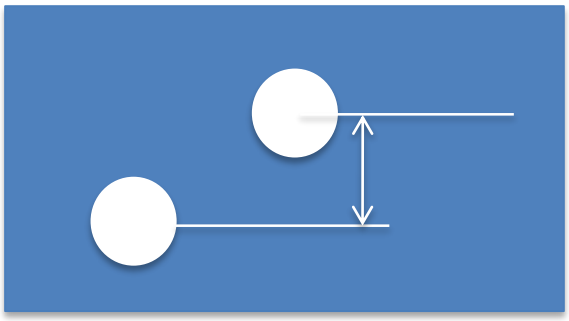

(b) Offset Voids

Figure 3-11: Domain set up showing two voids of 10 µm diameter embedded in HMX matrix of size 50 µm × 30 µm (a) Voids separated by a horizontal gap are named as inline voids (b) Voids separated by both horizontal gap and vertical offset are named as offset voids.

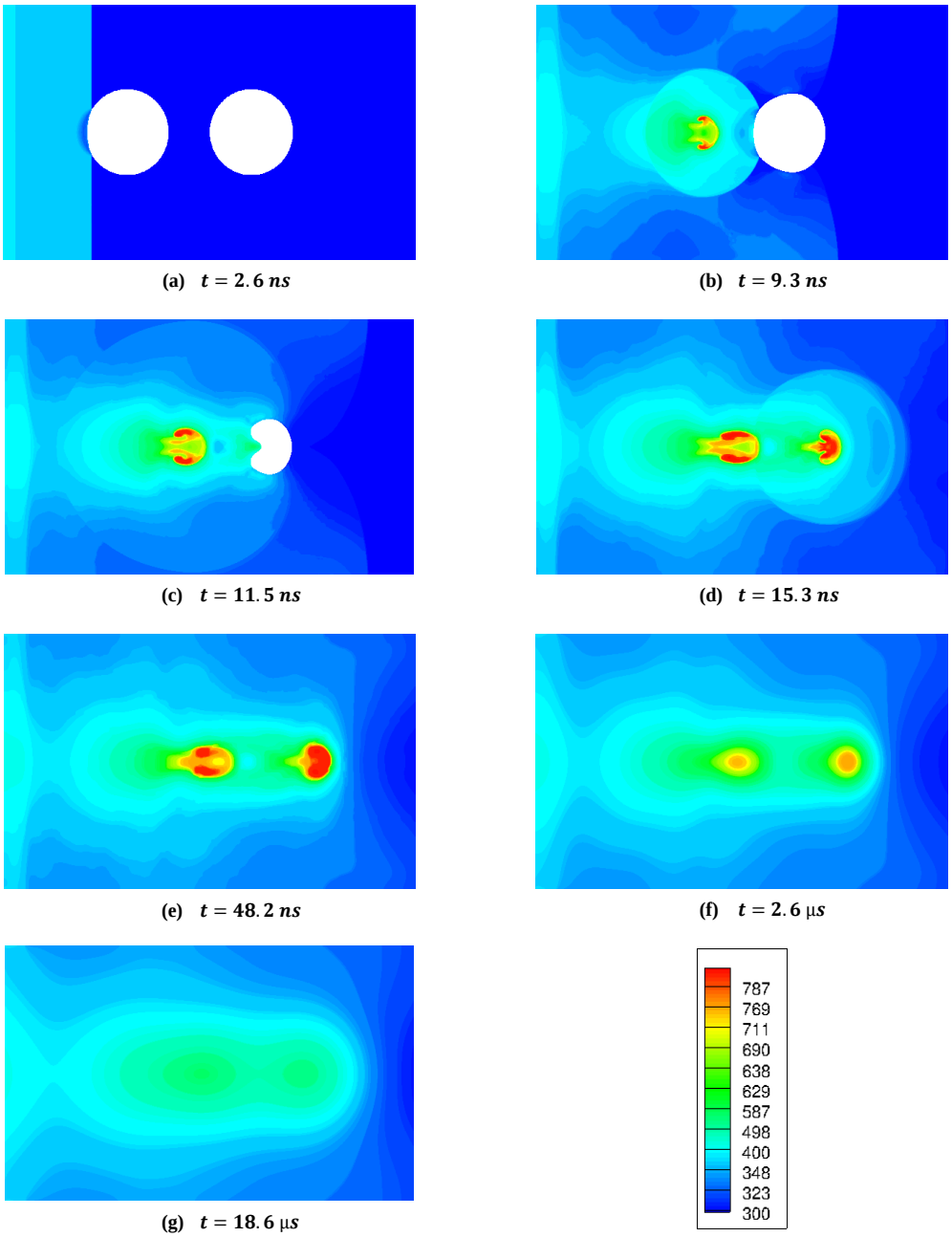


Figure 3-12: Temperature (K) contours at different stages showing collapse of inline voids leading to no reaction and ignition because of shielding effect on downstream void.

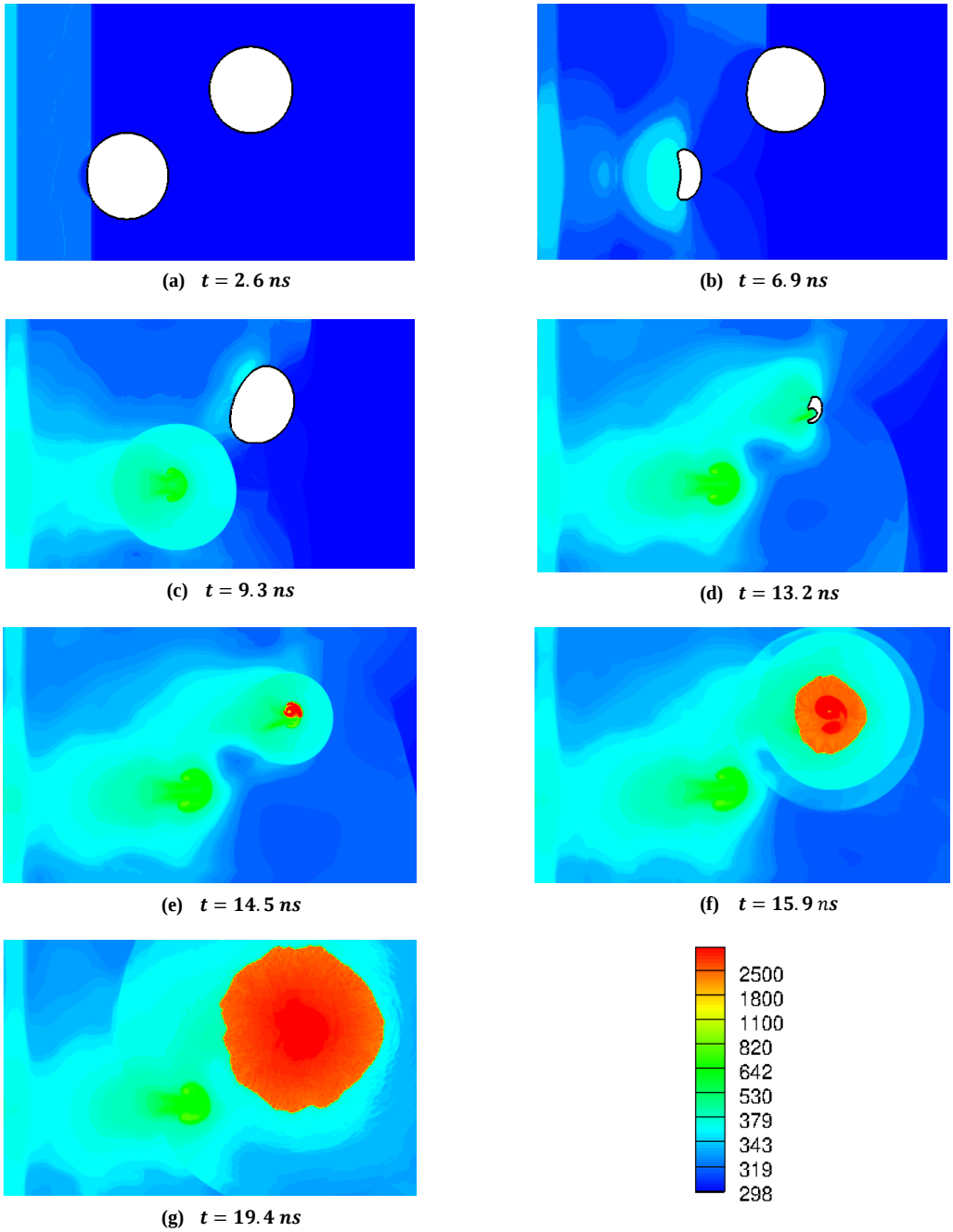


Figure 3-13: Temperature (K) contours at different stages showing collapse of voids with offset 0.5D leading to reaction and ignition at the hot spot formed at the downstream void collapse.

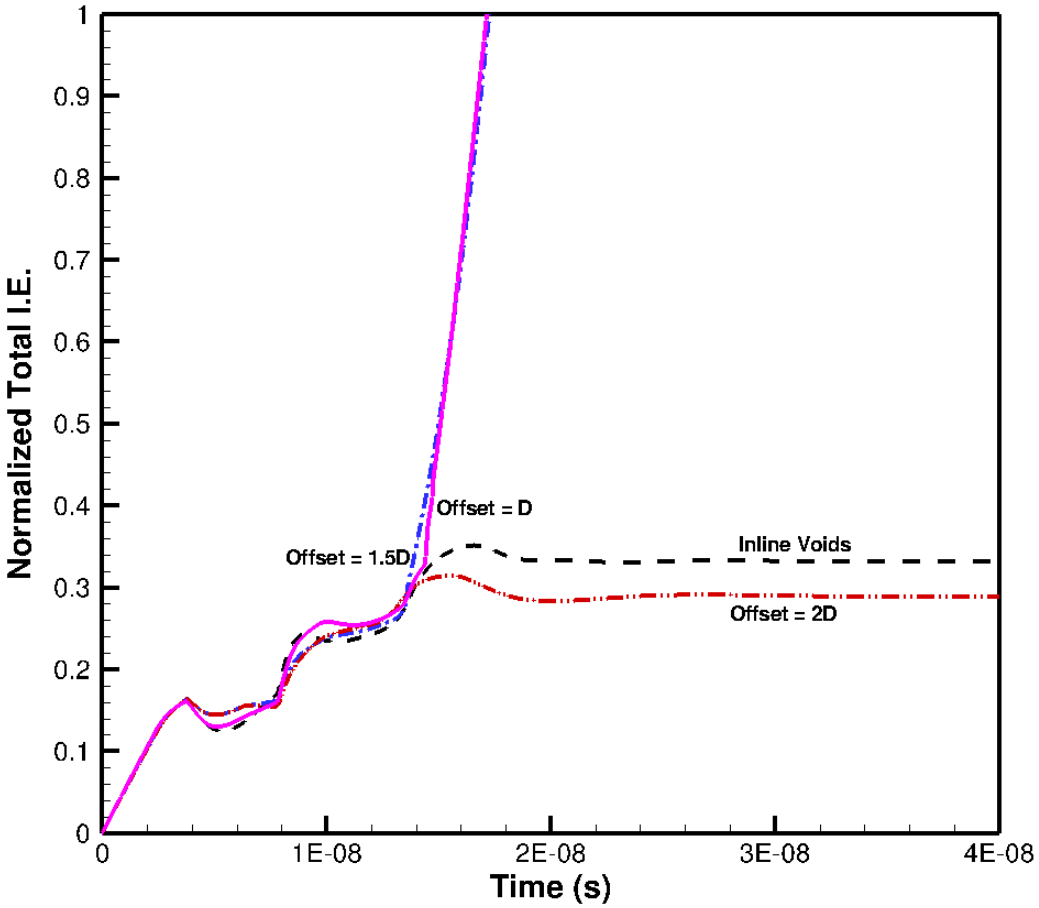


Figure 3-14: Variation of normalized total specific internal energy with time for shock speed of 550 m/s for different offset values showing ignition for offset *D* and *0.5D.*

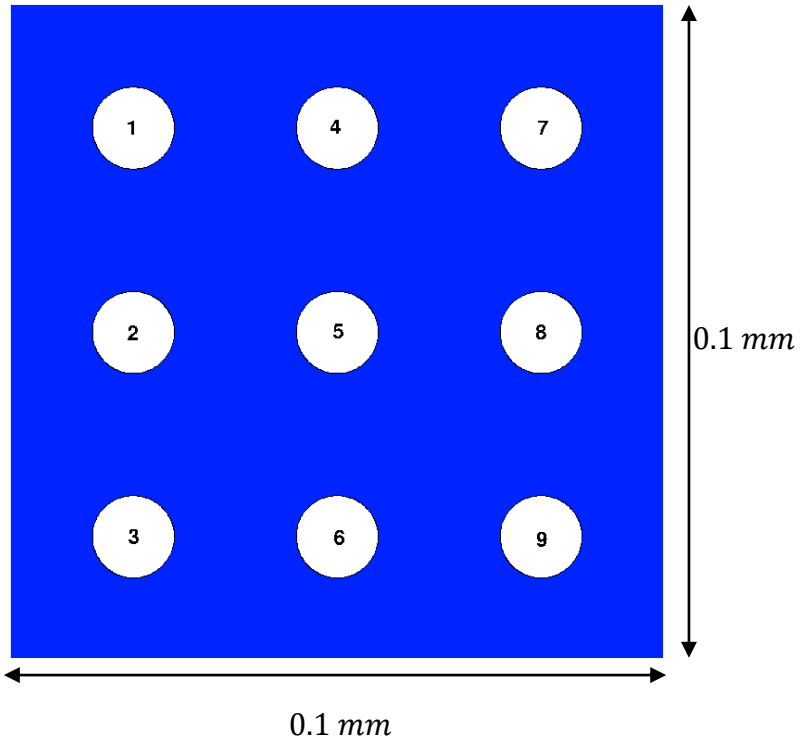


Figure 3-15: Heterogeneous HMX domain of size of 0.1 mm × 0.1 mm with 10% void volume fraction (void diameter of 10 μm). The voids are distributed in a regular order and being numbered from 1-9.

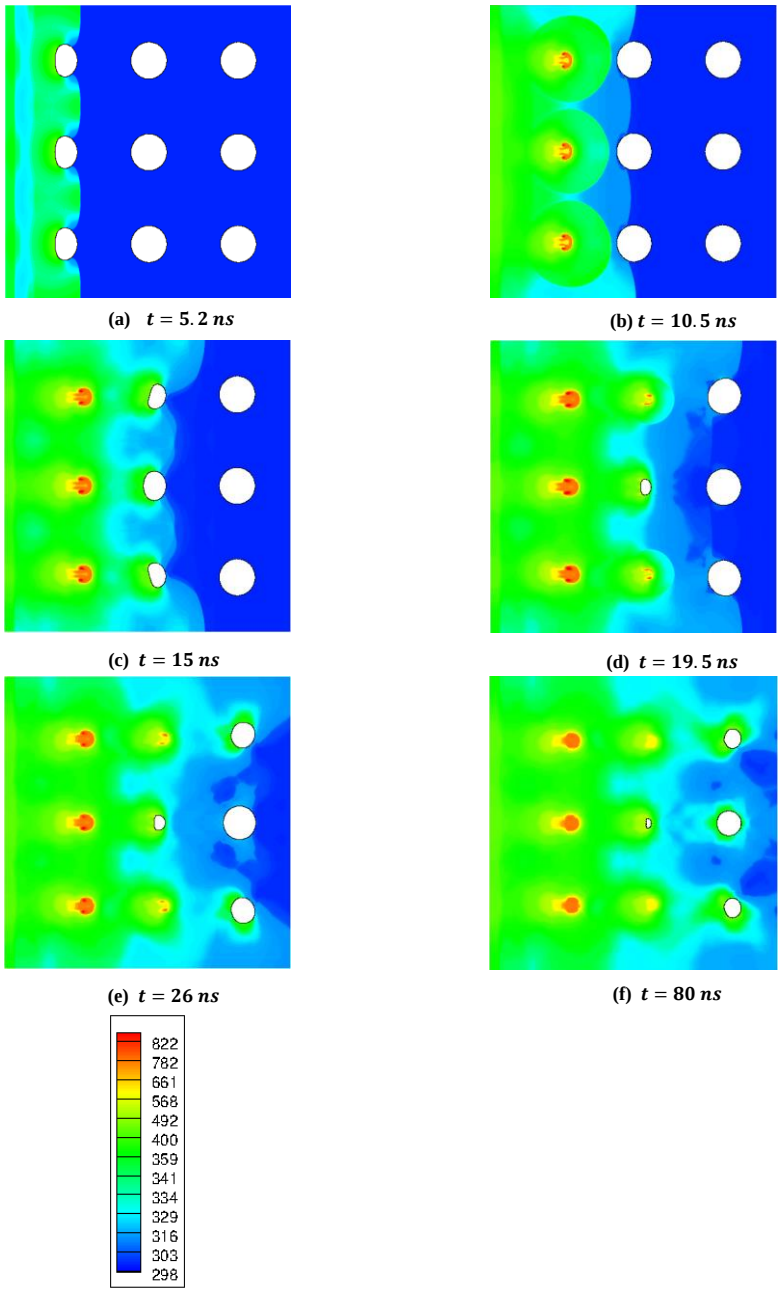


Figure 3-16: Temperature (K) contours at different times showing void collapse and void-void interaction for regularly distributed voids in HMX.

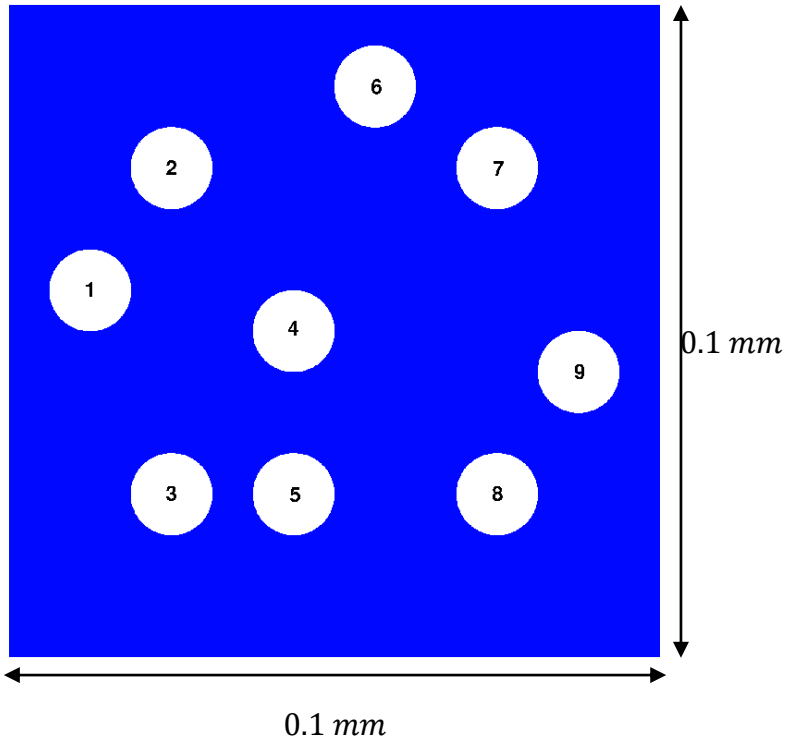


Figure 3-17: Heterogeneous HMX domain of size of 0.1 mm × 0.1 mm with 10% void volume fraction (void diameter of 10 μm). The voids are distributed randomly.

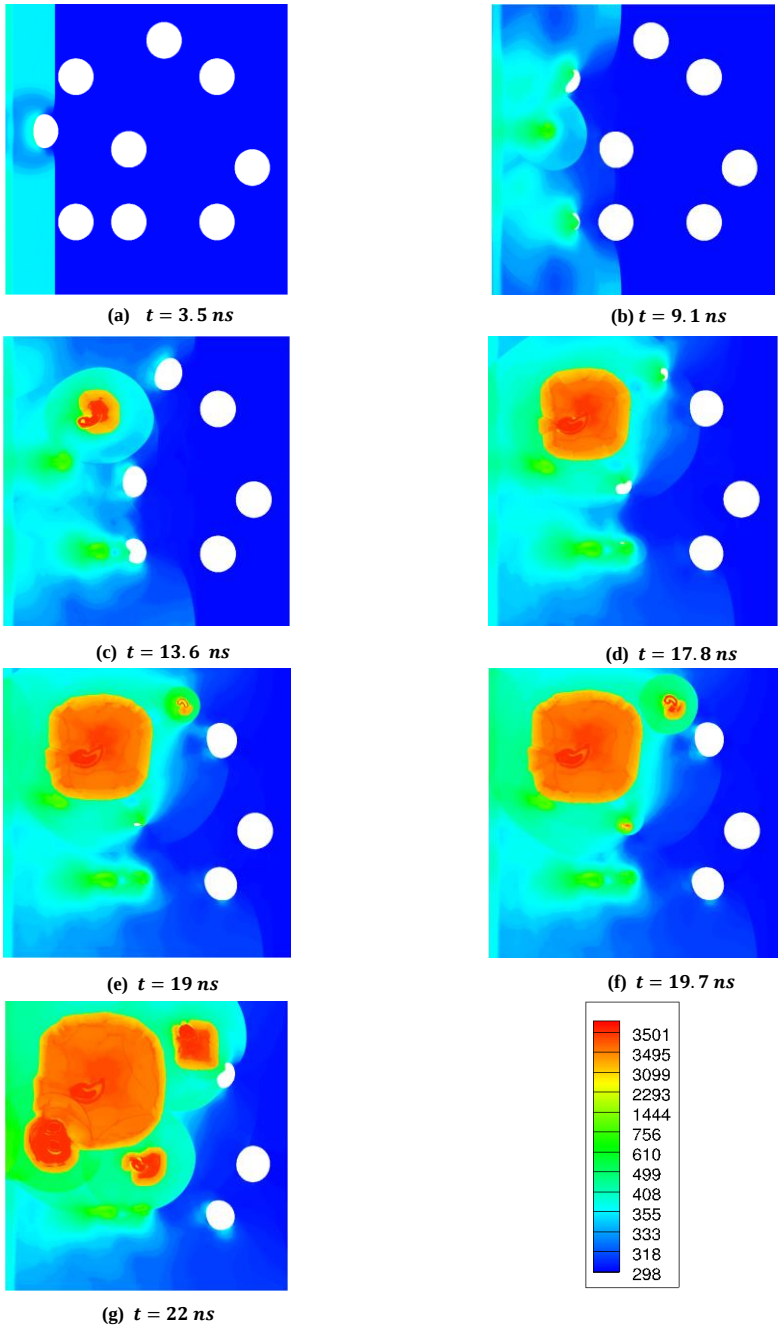


Figure 3-18: Temperature (K) contour plots at different times showing void collapse and void-void interaction for randomly distributed voids.

# CHAPTER 4

# PRESSED ENERGETIC MATERIALS UNDER SHOCK LOADING

## 4.1. Introduction

The chapter is aimed at the study of effects of microstructural characteristics of heterogeneous explosives on their shock initiation behavior. This is shown by performing mesoscale simulations on two different samples of HMX based pressed energetic materials, called Class III and Class V. These samples vary from each other in terms of the morphological characteristics of their microstructure. In general Class III consists of large grains of HMX with large variance in the size distribution while Class V consists of small grains with small variance of grain size. A detailed description of the morphological features of Class III and Class V samples are discussed in the work of Welle et. al.[5] Embedded within the current numerical framework are image processing algorithms[76] to obtain the level set representation of the imaged microstructure of the explosives. The image processing algorithms are applied to the SEM image samples of Class III and Class V explosives. The image processing framework is discussed in detail in chapter 2. Hence, the overall framework allows to perform mesoscale numerical simulations on the real geometries rather than idealized shapes.

In order to study the shock initiation behavior, the reaction initiation mechanism for HMX is modeled using Henson Smilowitz chemical kinetic law[77]. The effect of heat diffusion is also considered in this analysis. It is shown that the shock initiation behavior of Class III and Class V samples vary from each other for the same applied shock load. In the Class III sample, under the applied shock load, initiation and growth of chemical sample is observed. However, Class V sample does not ignite. The current analysis is further extended to understand the reason behind this difference in shock initiation behavior of the two samples. It is found that orientation of voids with respect to the incident shock wave direction plays a crucial role in the determination of sensitivity of the samples.

Hence, numerical experiments are performed to study the void orientation effects on initiation behavior. It is shown that there exists a range of critical angles for which reaction initiation is imminent.

## 4.2.Results

It is mentioned previously that the current analysis is focused towards study the effects of microstructural geometry on shock initiation behavior of pressed explosives. Two different types of pressed explosives, Class III and Class V are considered; SEM images of these two types of pressed explosives were obtained and segmented to obtain computational microstructures. Class III explosives have a microstructure that displays relatively large HMX crystals (Figure 4-4(a)). On the other hand, Class V explosives have a relatively uniform microstructure consisting of small HMX crystals[5] (Figure 4-1(a)). Following the analysis of the microstructural response, numerical experiments are performed to provide insights into the factors responsible for differences in shock initiation behavior of these explosive microstructures.

### 4.2.1 Shock initiation and ignition analysis of Class V pressed explosive

Class V explosives are fine-grain explosives in which HMX crystals are small and grain sizes are of the order of tens of microns. Heterogeneities in Class V explosives are present in the form of small voids. A two-dimensional sample of a Class V explosive is shown in Figure 4-1(a) and its microstructural details are discussed in the work of Welle et. al[5]. Figure 4-1(a) shows that the given sample of Class V explosive contains randomly distributed voids of different sizes. Shock loading of the given sample may lead to collapse of these voids and formation of hot spots in the mesoscale sample leading to initiation if the hot spots satisfy criticality conditions, i.e. depending on the size and the temperature of the hot spots, chemical reactions may initiate. For a specific loading condition the hot spot temperature depends on the morphological characteristics of the voids such as the size and

shape. Hence the realistic estimation of the hot spot temperature demands explicit modeling of the voids and crystals geometry. In the current work, the explicit modeling of the microstructure is performed using an image-to -computation approach as explained in chapter 2. The image processing approach is applied to the image intensity field obtained from SEM image of Class V image having 1024 ×690 pixels as shown in Figure 4-1(a). The size of the given Class V sample is 25 μm ×16 μm. The image processing algorithm generates the level set field representing the microstructure. The level set field thus obtained is superimposed on the original SEM image of Class V explosive as shown in Figure 4-1(b). Figure 4-1(b) shows that image processing algorithms are able to represent the microstructural details with desirable accuracy.

In the current analysis, a grid size of  is used corresponding to 1024 ×690 grid points. The number of grid points have been kept the same as the image resolution of 1024 ×690 pixels. The microstructure is "shock loaded" by imposing a top-hat shaped pulse at the left edge of the computational domain. The pulse produces a particle velocity of 1000 m/s for a 0.01 μs duration and is applied as shown in Figure 4-1(c). The shock analysis is performed with chemical decomposition of HMX modeled using Henson-Smilowitz chemical kinetics model[77]. Heat conduction effects have been considered in the current analysis.  Therefore the initiation of the shock-loaded sample takes place under the combined effects of hydrodynamic collapse of voids, plastic deformation and resulting heating of the crystals, chemical reactions and thermal diffusion of heat away from hotspots. The pressure contour plots from the shock analysis are shown in Figure 4-2.

Figure 4-2 shows that the small pores of the Class V explosive have collapsed under the influence of the prescribed shock load. The void collapse generates localized hot spots over a range of temperatures. The temperature range of the hot spots generated varies from 700 K-1200K and depends on void size, location and the relative position of the void in a cluster of voids. This is due to the effects of shielding and reinforcement that occurs due to void-void interactions, as shown in previous work[58]. However, this hot spot temperature

range is not sufficient in the present case to trigger chemical reactions. Therefore, eventually the hot spots cool down due to diffusion of heat to the surrounding material and no reaction is observed. The contour plots of solid β-HMX are shown in Figure 4-3. It can be observed that decomposition of solid β-HMX takes place at the hot spot locations. However no gaseous products are observed. Solid β-HMX is transformed to solid δ-HMX through an endothermic reversible reaction. The hot spots created therefore are non-critical and initiation does not occur in this Class V sample.

### 4.2.2 Shock initiation and ignition analysis of a Class III pressed explosive

In contrast to Class V explosives, Class III explosives are categorized as coarse-grained explosives where the size of the HMX crystals are greater than $100\ \mu m$. The heterogeneities in Class III explosives are present in the form of elongated voids, created because of extended cracks which separates large HMX crystals. A 2D SEM image sample of the Class III explosive is shown in Figure 4-4(a) and its microstructural details are discussed in the work of Welle et. al.[5].

The 2D SEM image is characterized by $1024 \times 690$ pixels and the corresponding physical dimension is $25\ \mu m\ \times 16\ \mu m$. The grid size of $\Delta x = 0.025 \mu m$ corresponding to $1024 \times 690$ grid points has been used in the current analysis. The same shock loading used above for the Class V explosive, i.e. $1000\ m/s$ speed and $0.01\ \mu s$ duration is used in the current analysis. The shock load is applied from the west face of the domain boundary as shown in Figure 4-4(c). The temperature and pressure contour plots from the shock analysis are shown in Figure 4-5 and Figure 4-6 respectively.

For the given shock loading, initiation of chemical reactions and ignition is observed for the Class III explosive sample. From the temperature plots shown in Figure 4-5(b), it can be observed that the collapse of the rather elongated voids in the Class III microstructure leads to the formation of extensive hot spots. Chemical reactions trigger at

some of these hotspots depending on the local temperature as shown in Figure 4-5(b-f). The chemical reactions grow from its original location into the surrounding material. This growth is strengthened by other hot spots lying in the vicinity of the reaction front. In fact, the reaction and ignition starts at multiple locations and the reaction front from these hot spots grows and combines to form a strong front as shown in Figure 4-5(f). The shock wave loads the explosive as shown by the pressure contour in Figure 4-6 and leaves behind the reacting zones in the domain. The chemical decomposition of HMX and the production of gaseous species have been demonstrated by plotting the contour plots of $\beta - HMX$ and one gas phase species ($HCN$). It can be seen from Figure 4-7 that the $\beta - HMX$ transformation takes place at the void collapse regions. In the regions where the exothermic gas phase chemical reactions are initiated $\beta - HMX$ transforms completely to the gaseous products such as $HCN, NO_2$ etc. as shown in Figure 4-7(c,e) indicating possible full-fledged ignition.

### 4.2.3 Comparison of shock initiation behavior of Class III and Class V samples

Shock loading analysis of Class III and Class V samples indicates that the morphology of voids in the microstructure can significantly affect the shock initiation behavior of the explosives. For the same prescribed loading, ignition is seen to take place at localized hot spots in Class III explosives, but not in the Class V explosive. One hypothesis for this difference in initiation response is the effect of shape, size and orientation of the voids in the two materials because it is easily seen that the microstructural geometries of Class III and Class V vary significantly from each other in all of these respects. In Class V explosives, the voids are small and short in comparison to Class III explosives where voids are large and elongated. For the loading condition specified the small voids in the Class V explosive do not create hot spots with sufficient strength to ignite on their own, while the elongated voids in Class III explosive collapse at sufficiently

high temperatures leading to initiation of chemical reactions. However, reactions are triggered at only some of the elongated voids in Class III explosive microstructure. The elongated voids where reactions initiate can be seen in Figure 4-5(c) and Figure 4-5(d). It can be observed that both the elongated voids at which reactions are initiated are oriented at a similar angle with respect to the incident shock. The first elongated void where reactions initiate as shown in Figure 4-5(c) is oriented at approximately $45°$ with respect to the incident shock and the second elongated voids shown in Figure 4-5(d) is oriented at approximately $50°$. This indicates the possibility of the dependency of shock initiation in explosives on the orientation of elongated voids. Such effects of elongated voids and their orientation have also been suggested in the work of Levesque et. al.[60]. Here it is shown that these effects can provide a plausible physical explanation for the sensitivity of the Class III sample for the tested conditions.

### 4.2.4 Numerical experiments on elongated voids at different orientations

It was shown in the previous section that the orientation of elongated voids in the microstructure can affect the sensitivity of the sample to shock loading. Hence, this section is focused on the determination of the way in which the orientation of the elongated voids influence the initiation response in a given sample of pressed energetic material.

The elongated void used in the analysis is $10\ \mu m$ long $0.5\ \mu m$ thick. As in the case of the imaged microstructure experiments presented above shock loading with $1000\ m/s$ speed and $0.01\ \mu s$ duration is applied from the west face of the domain. Six different orientations starting from $0°$ to $90°$ of elongated void have been used in the current analysis. The grid size used in the analysis is $\Delta x = 0.025\ \mu m$, which is also the same as for the previous cases.

The shock analysis on elongated voids with $45°$ and $90°$ angle with respect to the incident shock is discussed in this section. The initial configuration of the elongated void

for 90° orientation angle is shown in Figure 4-8. The temperature and pressure contour plots obtained from the shock analysis are shown in Figure 4-9 and Figure 4-10. It can be seen from Figure 4-9 that a hot spot is formed due to the collapse of the elongated void with the 90° orientation. The hot spot temperature in this case however is not sufficient to initiate chemical reactions in the time duration of the supplied shock pulse. It can be observed from the pressure plot (Figure 4-10) that the imposed shock wave interacts with the upstream void surface and generates a rarefaction wave following shock reflection from the void surface. The interaction of the rarefaction wave (which results in the lowering of temperature in the vicinity of the void) with the incipient hot spot leads to reduction in the intensity of the hot spot as shown in temperature plots in Figure 4-9(c,e). Hence, shock loading on the 90° -orientation elongated void causes no initiation of reactions. It can be expected that the effects of the rarefaction waves can be different with different orientations of the elongated void. This is because the rarefaction wave is expected to be strongest when it meets a larger area of free surface as in the 90° -orientation void above. For voids that are not oriented normal to the shock the surface area exposed to the incident shock will be lower. To explore whether this expectation indeed holds, the elongated void is placed at various orientations with respect to the incident shock. First, shock loading on an elongated void at an 45° angle with respect to the incident shock is performed. The initial configuration is shown in Figure 4-11. The temperature and pressure plots obtained from the computations are shown in Figure 4-12 and Figure 4-13 respectively. Figure 4-12 shows that for this orientation angle of 45° with respect to the incident shock reactions are triggered and grow in the domain, causing ignition. In this case, it can be observed from the pressure plot, Figure 4-13, that when the incident shock interacts with the void surface, two processes come into play. First, a rarefaction wave is generated due to the shock reflection at the free surface. Second, collapse of the elongated void takes place successively, progressing along the length of the inclined void as the incident shock arrives at these locations. Each successive collapse leads to the formation of a system of blast

waves that emanate from the collapse locations. Similar to the case of a series of voids offset[24] from each other the blast wave generated from one collapse reinforces the collapse of the void downstream. Due to this successive collapse and reinforcement, the rarefaction wave does not succeed in lowering the hot spot temperature significantly in this case as compared to the previous $90°$ orientation case. The species decomposition for the 45°inclined void can be seen in the $\beta - HMX$ (solid) and $HCN$ (gaseous species) concentration plots shown in Figure 4-14 and Figure 4-15 respectively. The solid $\beta - HMX$ transforms completely to the gaseous products during the ignition process.

To develop further the hypothesis of the dependence of initiation at elongated voids on the void orientation, the above experiment is repeated for four other angles, i.e. for voids oriented at $0°$, $15°$, $30°$ and $60°$ to obtain the range of orientation angles for which reaction will initiate. The maximum temperature obtained in the domain during the simulation can be used as a parameter to indicate the possibility of ignition. The maximum temperature variation with orientation angle is shown in Figure 4-16. It can be observed that elongated voids with orientation angle lying between $30° - 50°$ are more sensitive to ignition as compared to other angles. This is because, for that range of angles, the effect of repeated collapse of segments of the void along the length of the elongated void causes strong enough hot spots to overwhelm the cooling effect caused by the rarefaction wave that comes off the void surface.

From the above numerical studies of the response of elongated voids, it can be seen that orientation of the elongated voids with respect to the incident shock plays a crucial role in generating hot spot of sufficient strength to initiate chemical reaction. More specifically, it is the competing effects of rarefaction waves (due to unloading from compression at the void surface) and the compressive waves generated due to the (successive) void collapse that determines whether chemical reaction and ignition will take place. This explains why, in the case of the Class III sample, the presence of elongated voids at close to $45°$ orientation led to the initiation of reactions in that microstructure.

Thus, the insights obtained from the study of idealized elongated voids provide an explanation for the observed initiation behavior of the Class III and Class V samples investigated in Sections 4.2.1 and 4.2.2.

## 4.3. Conclusions

The microstructures of Class III and Class V samples vary in terms of their grain and void sizes. Class III is a coarse grained sample whereas Class V is a fine grained explosive. The voids present in Class III sample are elongated and present in the form of extended cracks. On the other hand, the voids in the Class V sample are small in size. Shock loading analysis is performed using on both samples with shock speed of 1000 m/s and pulse duration of 0.01 μs. Shock load leads to the formation of hot spots due to void collapse in both the samples. However, because of microstructural differences, shock initiation behavior of both samples varies a lot. Class III samples leads to initiation and ignition at certain localized hot spot locations. However, for the same shock load hot spot formed in Class V sample did not lead to ignition. The hot spot strength was not sufficient to start chemical reaction in Class V sample.

The current analysis is extended further to understand the reason behind shock initiation at only certain locations in Class III sample. After careful observation, it was observed that initiation of chemical reactions started at locations where the elongated voids are present at roughly 45° - 50° angle with respect to the incident shock. This led to the design of numerical experiments on elongated voids oriented at an angle with respect to the shock load. Six different angles ranging from 0° - 90° is considered in this study. The numerical experiments show that there lies a range of critical orientation angles which leads to initiation of chemical reaction in the explosive sample. The critical angle lies in between 30° - 50° range. It is observed that, the collapse of elongated voids involves two counter acting physical processes i.e rarefaction waves generated due to shock reflection from the void free surface and formation of compressive blast waves generated due to the void

collapse. It is the competition between these two effects which decides whether an elongated void will go critical or not.

The current study demonstrates that the shock initiation behavior of energetic materials is highly sensitive to the microstructure. Hence, it is very important to represent the microstructure accurately and perform shock analysis on real samples. This study also shows the orientation of elongated voids is an important factor effecting the initiation behavior of the explosives.

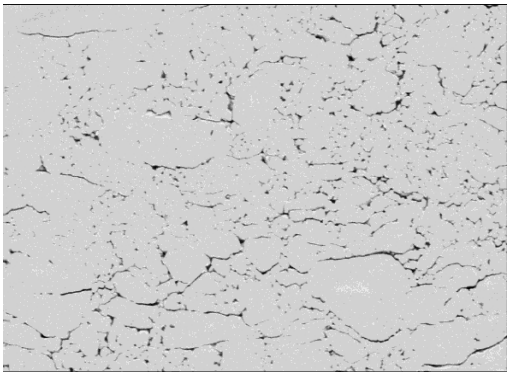

(a) SEM image of 2D section of Class V pressed explosive showing image intensity field with $1024 \times 690$ pixels

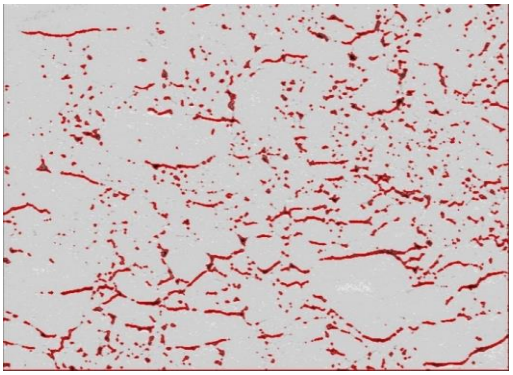

(b) Level set representation of the crystal boundaries obtained after active contour segmentation

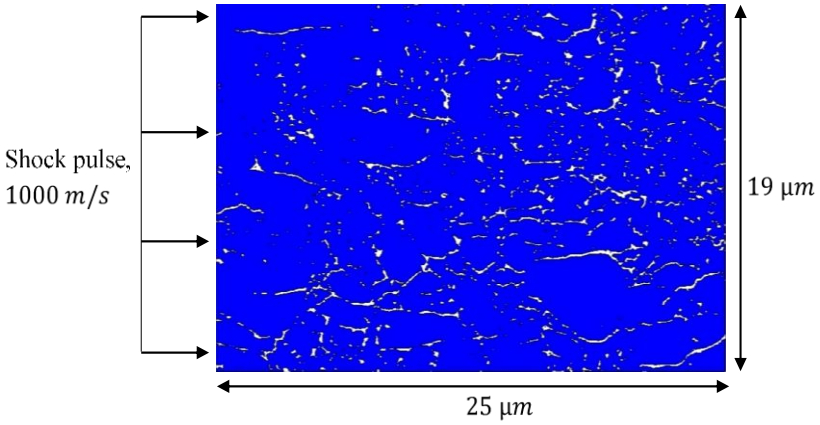


(c) Computational domain with $1024 \times 690$ grid points

Figure 4-1: Microstructural geometry of Class V pressed explosive obtained by applying active contour image segmentation algorithm on the 2D SEM image.

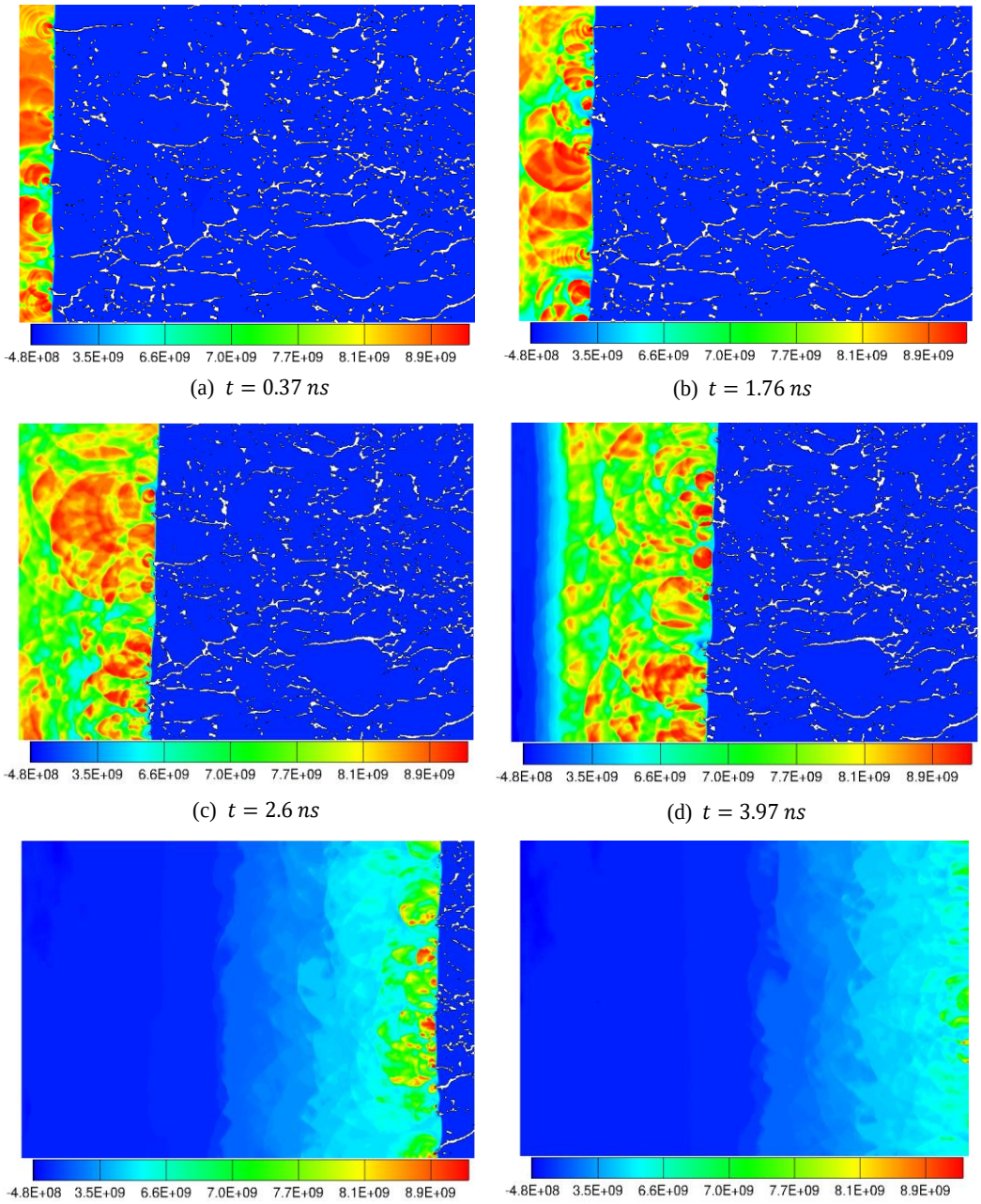


(a) $t = 0.37\ ns$ (b) $t = 1.76\ ns$

(c) $t = 2.6\ ns$ (d) $t = 3.97\ ns$

(e) $t = 4.57\ ns$ (f) $t = 5.84\ ns$

Figure 4-2: Pressure (Pa) contour plots at different time obtained from the shock analysis on Class V pressed explosive microstructure with $1000\ m/s$ shock pulse and $0.01\ \mu s$ duration.

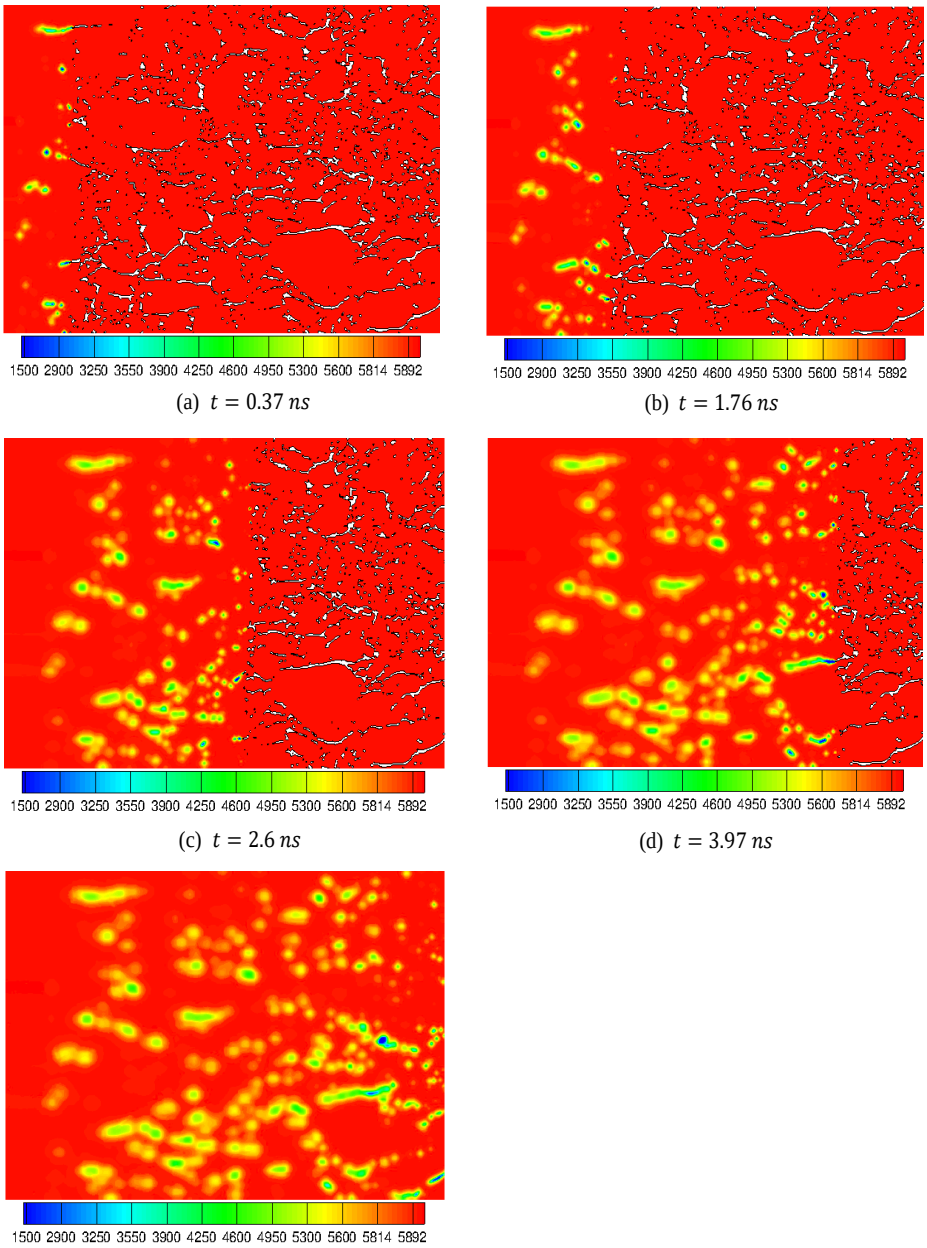


(a) $t = 0.37\ ns$ (b) $t = 1.76\ ns$

(c) $t = 2.6\ ns$ (d) $t = 3.97\ ns$

(e) $t = 5.84\ ns$

Figure 4-3: $\beta - HMX$ concentration$(mol/m^3)$ contour plots obtained from the shock analysis on Class V pressed explosive microstructure with $1000\ m/s$ shock pulse and $0.01\ \mu s$ duration. The plot shows the decomposition of solid $\beta - HMX$ to solid $\delta - HMX$ at the hot spot.

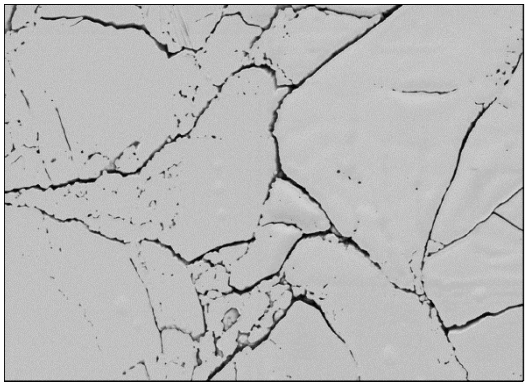

(a) SEM image of 2D section of Class III pressed explosive showing image intensity field with $1024 \times 690$ pixels

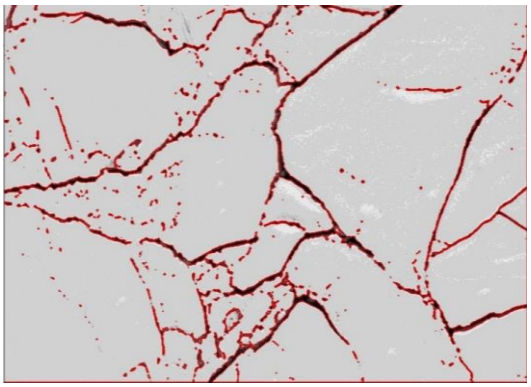

(b) Level set representation of the crystal boundaries obtained after active contour segmentation

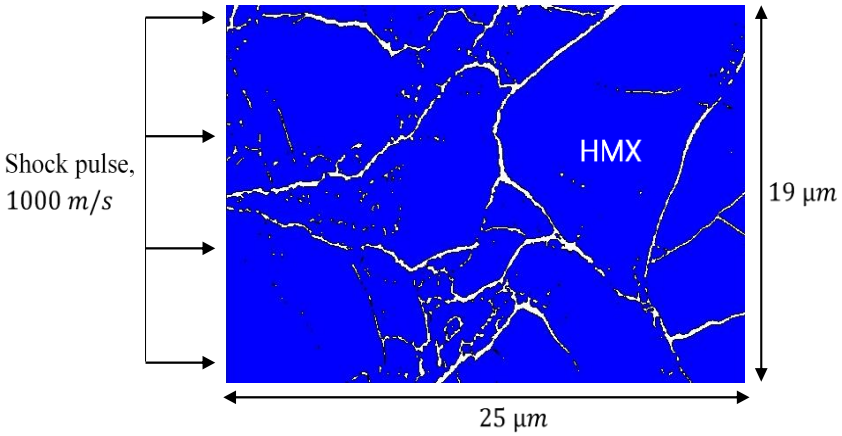


(c) Computational domain with $1024 \times 690$ grid points

Figure 4-4: Microstructural geometry of Class III pressed explosive obtained by applying active contour image segmentation algorithm on the 2D SEM image section.

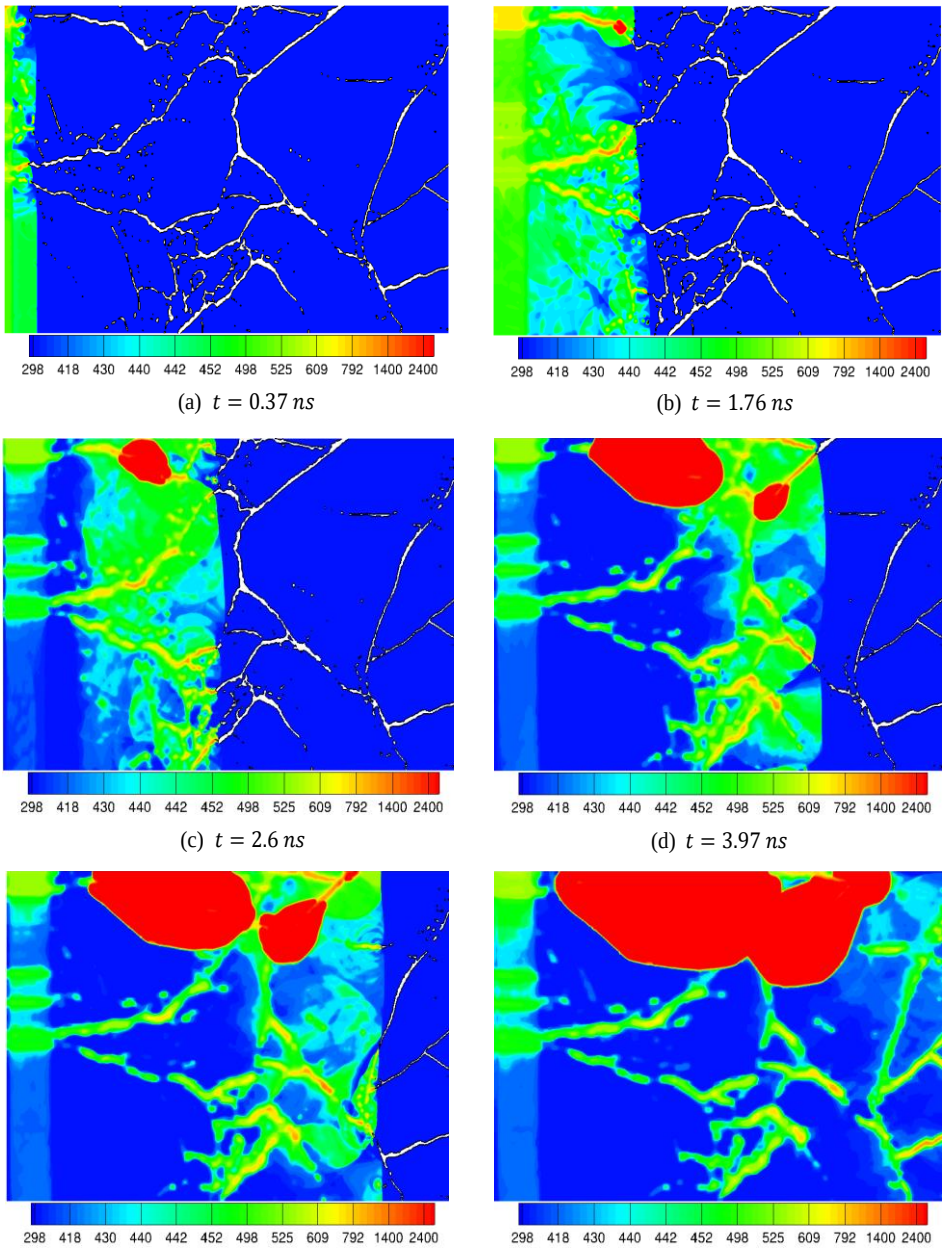


(a) $t = 0.37\ ns$ (b) $t = 1.76\ ns$

(c) $t = 2.6\ ns$ (d) $t = 3.97\ ns$

(e) $t = 4.57\ ns$ (f) $t = 5.84\ ns$

Figure 4-5: Temperature (K) contour plots obtained from the shock analysis on Class III pressed explosive microstructure with $1000\ m/s$ shock speed and $0.01\ \mu s$ duration. The plot shows shock propagation and formation of hot spots due to the collapse of extended cracks. The hot spots formed lead to initiate chemical reaction and ignition in HMX at different locations of the domain.

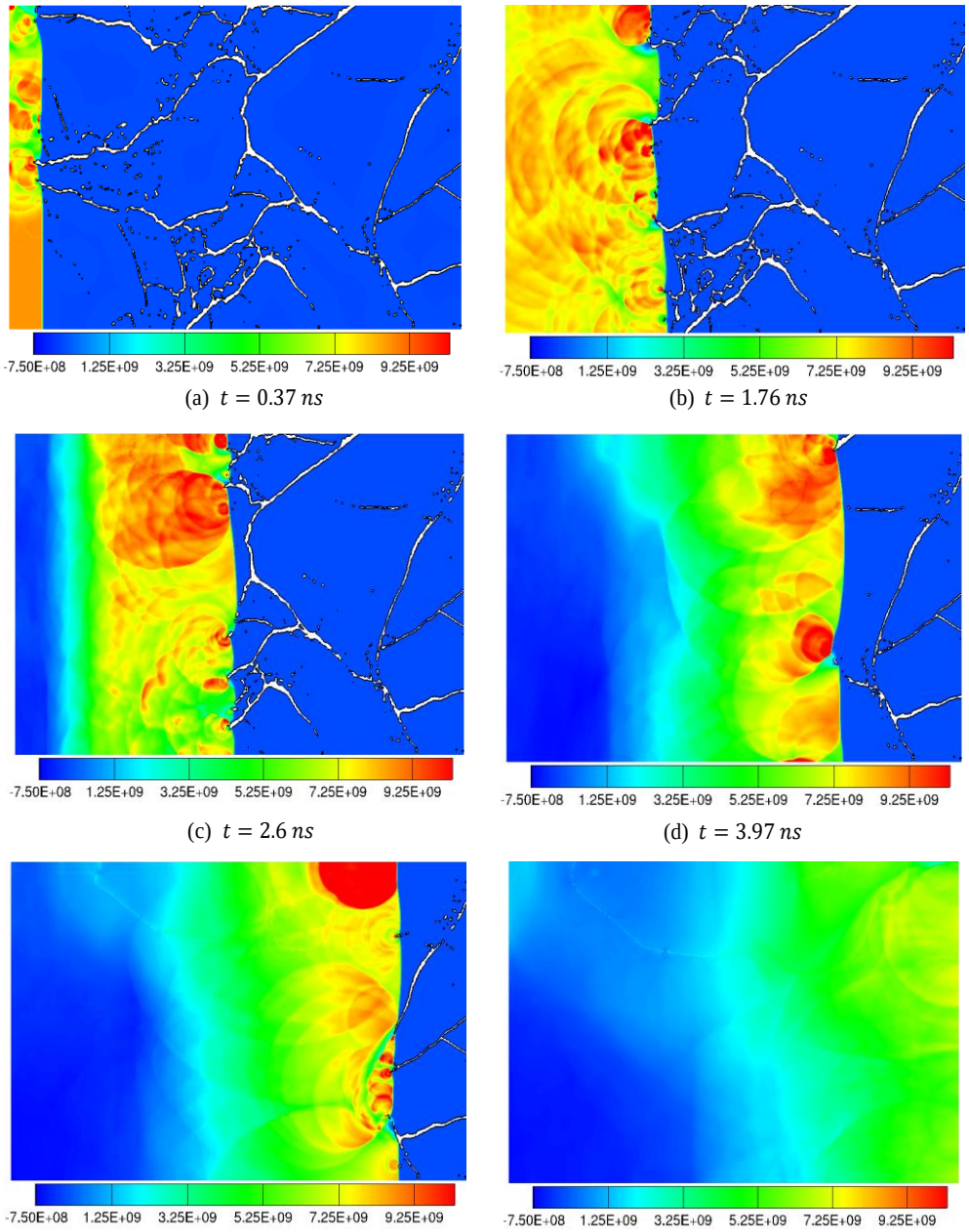


(a) $t = 0.37\ ns$ (b) $t = 1.76\ ns$

(c) $t = 2.6\ ns$ (d) $t = 3.97\ ns$

(e) $t = 4.57\ ns$ (f) $t = 5.84\ ns$

Figure 4-6: Pressure (Pa) contour plots at different times obtained from the shock analysis on Class III pressed explosive microstructure with $1000\ m/s$ shock speed and $0.01\ \mu s$ duration. Plots show shock loading on the microstructure leaving behind the field of hot spots.

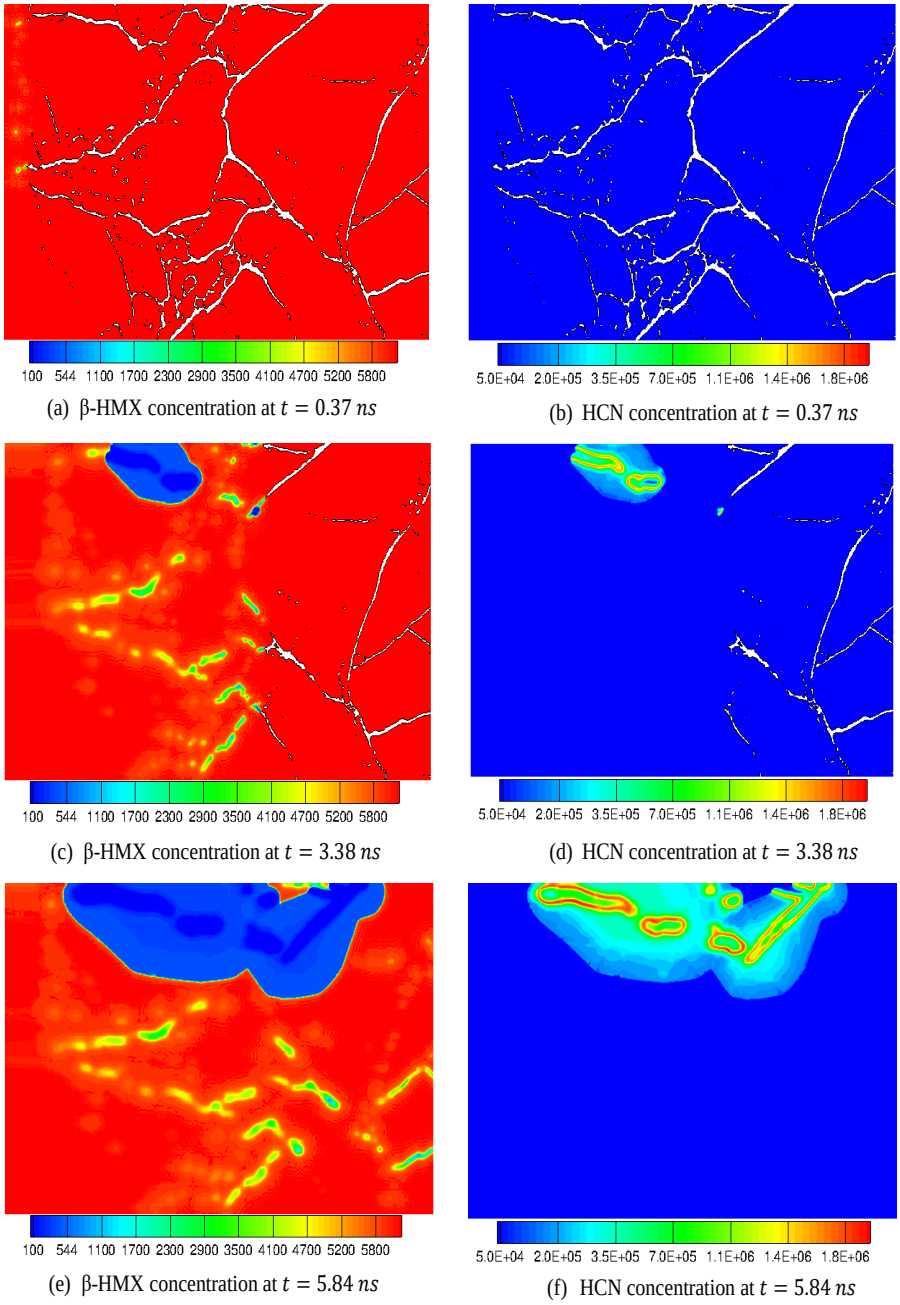


(a) β-HMX concentration at $t = 0.37\ ns$

(b) HCN concentration at $t = 0.37\ ns$

(c) β-HMX concentration at $t = 3.38\ ns$

(d) HCN concentration at $t = 3.38\ ns$

(e) β-HMX concentration at $t = 5.84\ ns$

(f) HCN concentration at $t = 5.84\ ns$

Figure 4-7: $\beta - HMX$ and HCN concentration$(mol/m^3)$ contour plots obtained from the shock analysis on Class III pressed explosive microstructure with $1000\ m/s$ shock pulse and $0.01\ \mu s$ duration. The plot shows the complete decomposition of solid $\beta - HMX$ to various gaseous products like HCN at the hot spots where ignition takes place.

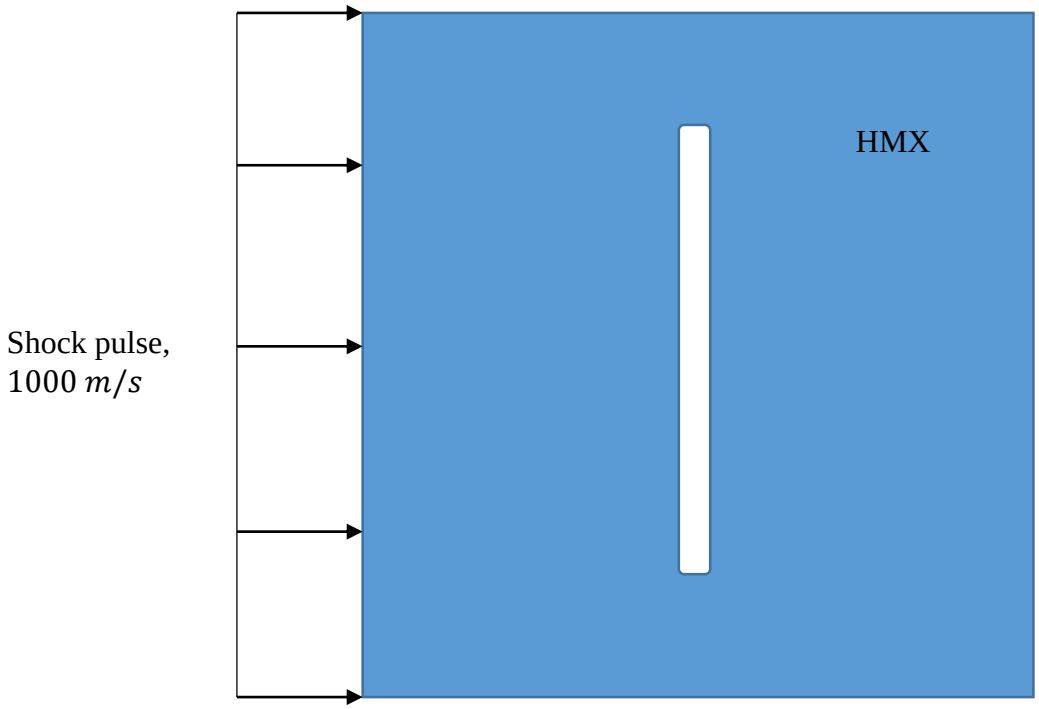


Figure 4-8: Initial configuration of elongated void in HMX aligned at an angle of 90° with respect to the incident shock loading of 1000 $m/s$ shock speed of 0.01 μ$s$ pulse duration.

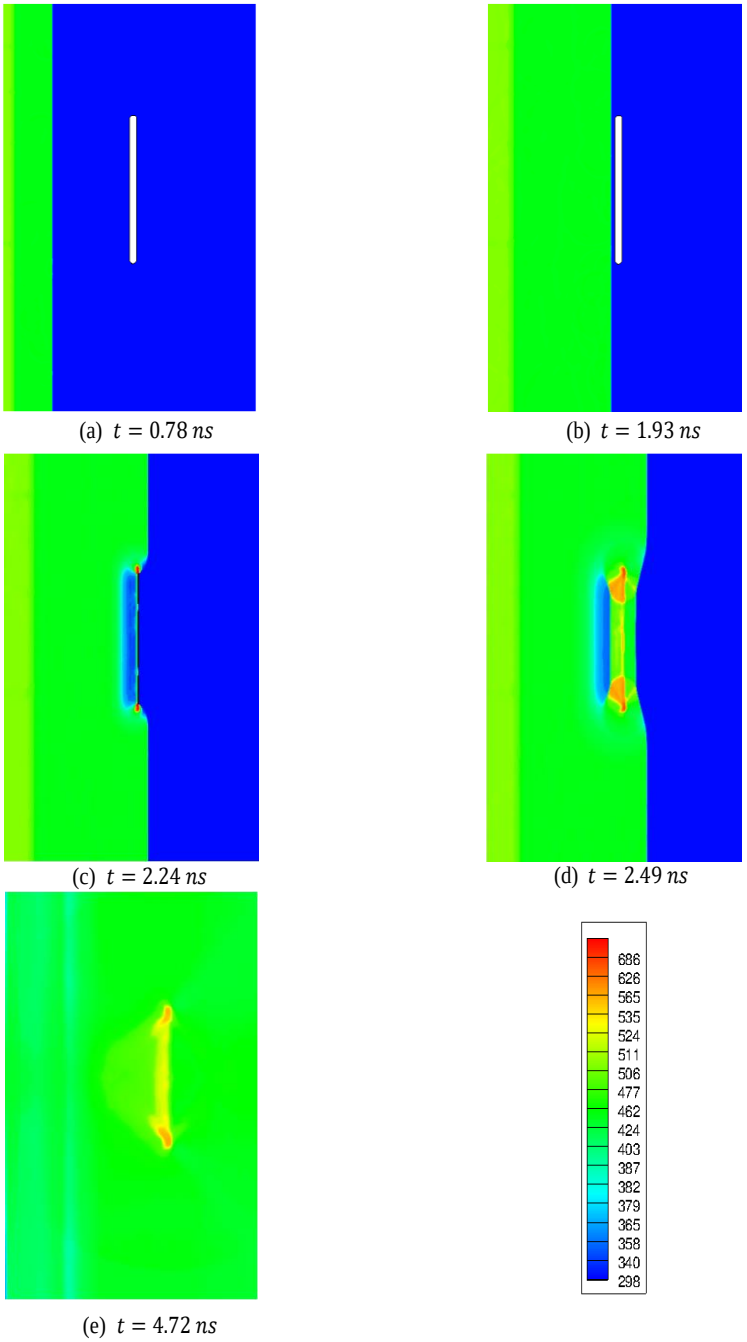


Figure 4-9: Temperature (K) contour plots obtained from the shock analysis on the elongated void in HMX with 1000 $m/s$ shock speed and 0.01 $\mu s$ duration. The elongated void is aligned 90° with respect to the incident shock. The plots show shock propagation and formation of hot spot due to the collapse of the elongated voids. The hot spot strength was not sufficient to initiate chemical reactions.

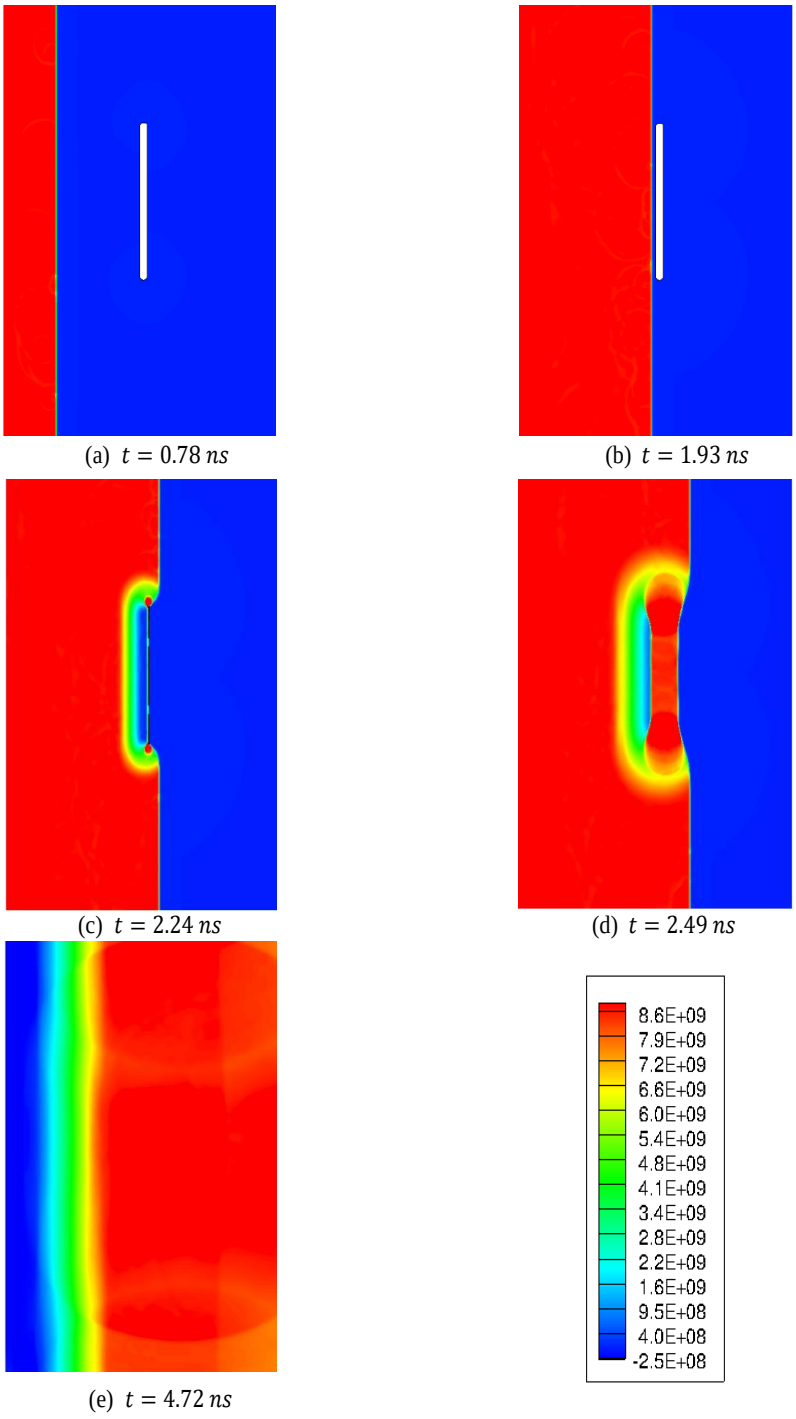


(a) $t = 0.78\ ns$ (b) $t = 1.93\ ns$

(c) $t = 2.24\ ns$ (d) $t = 2.49\ ns$

(e) $t = 4.72\ ns$

Figure 4-10: Pressure (Pa) contour plots obtained from the shock analysis on the elongated void in HMX with $1000\ m/s$ shock speed and $0.01\ \mu s$ duration. The elongated void is aligned $90°$ with respect to the incident shock. The plot shows shock propagation and formation of rarefaction wave due to the shock reflection at the free surface of the voids.

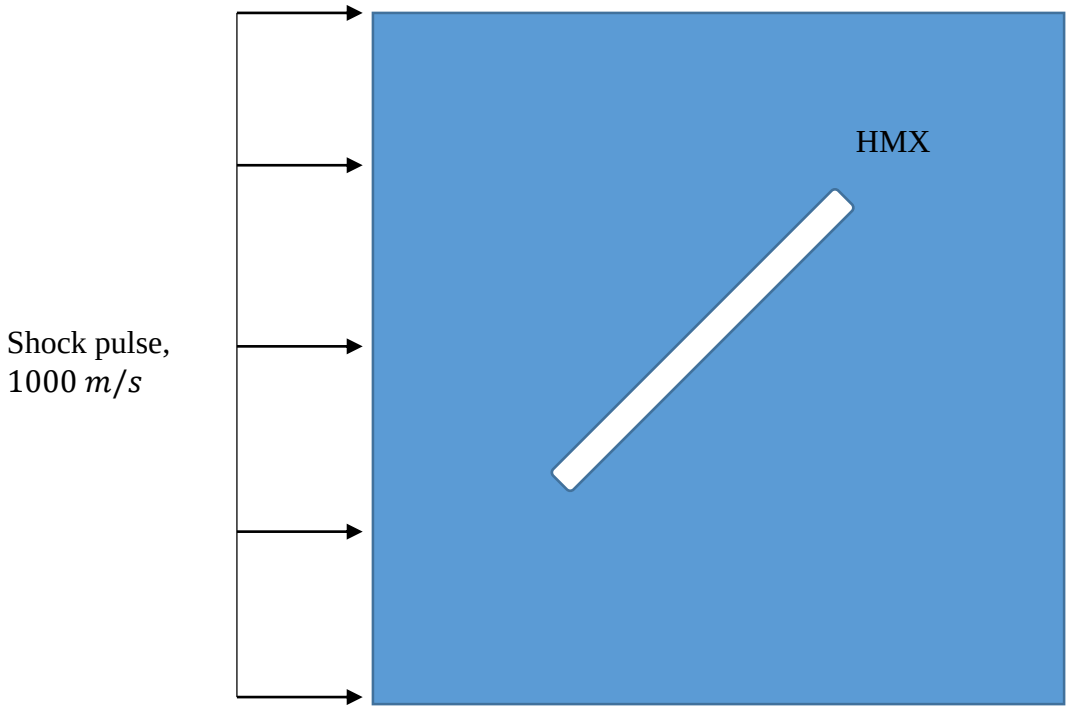


Figure 4-11: Initial configuration of elongated void in HMX aligned at an angle of $45^{\circ}$ with respect to the incident shock loading of $1000\ m/s$ shock speed of $0.01\ \mu s$ pulse duration.

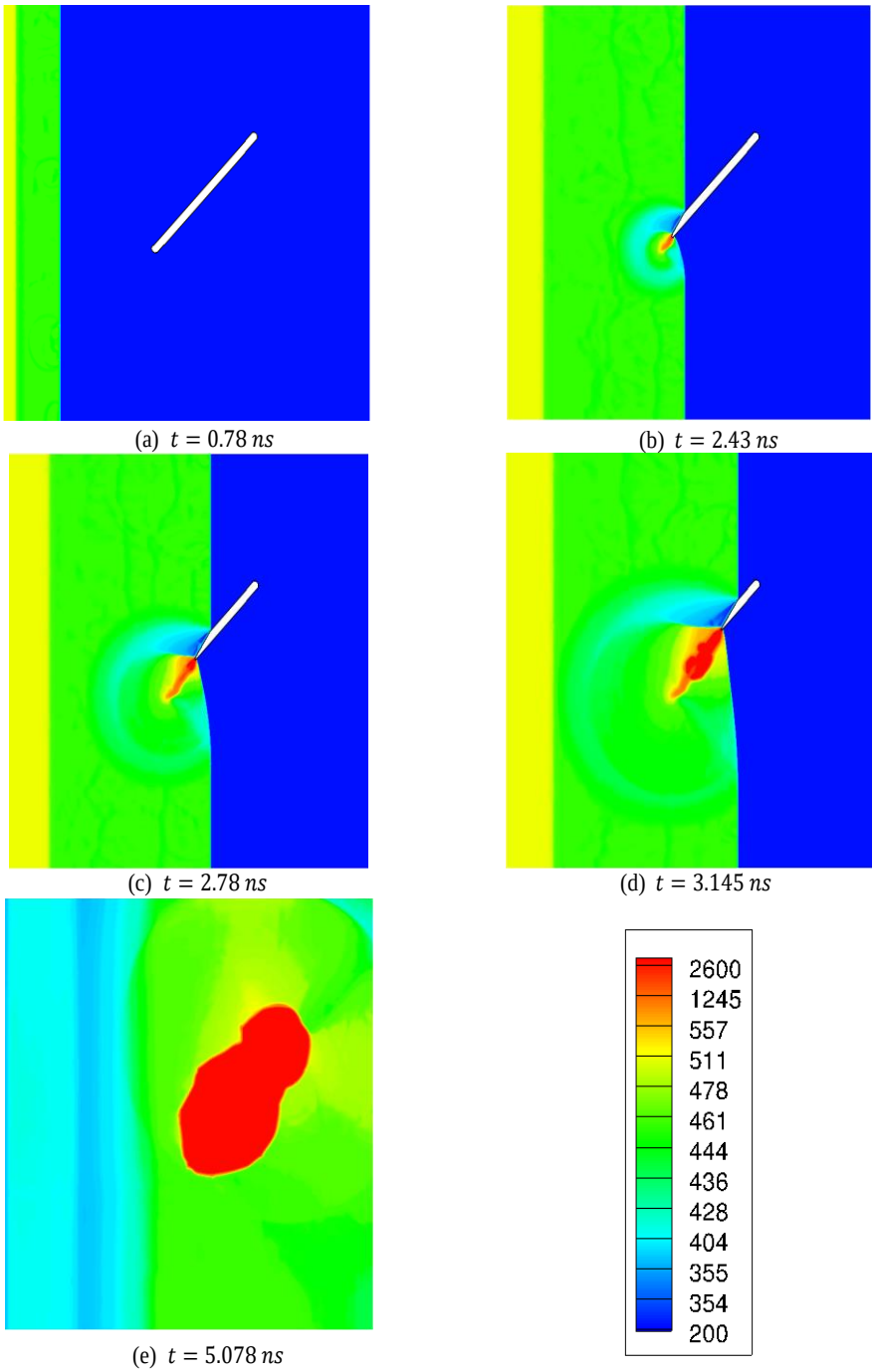


Figure 4-12: Temperature (K) contour plots obtained from the shock analysis on the elongated void in HMX with 1000 $m/s$ shock speed and 0.01 $\mu s$ duration. The elongated void is aligned 45° with respect to the incident shock. The plot shows shock propagation and formation of hot spot due to successive collapse of the elongated void leading to initiation and ignition of chemical reaction in the domain.

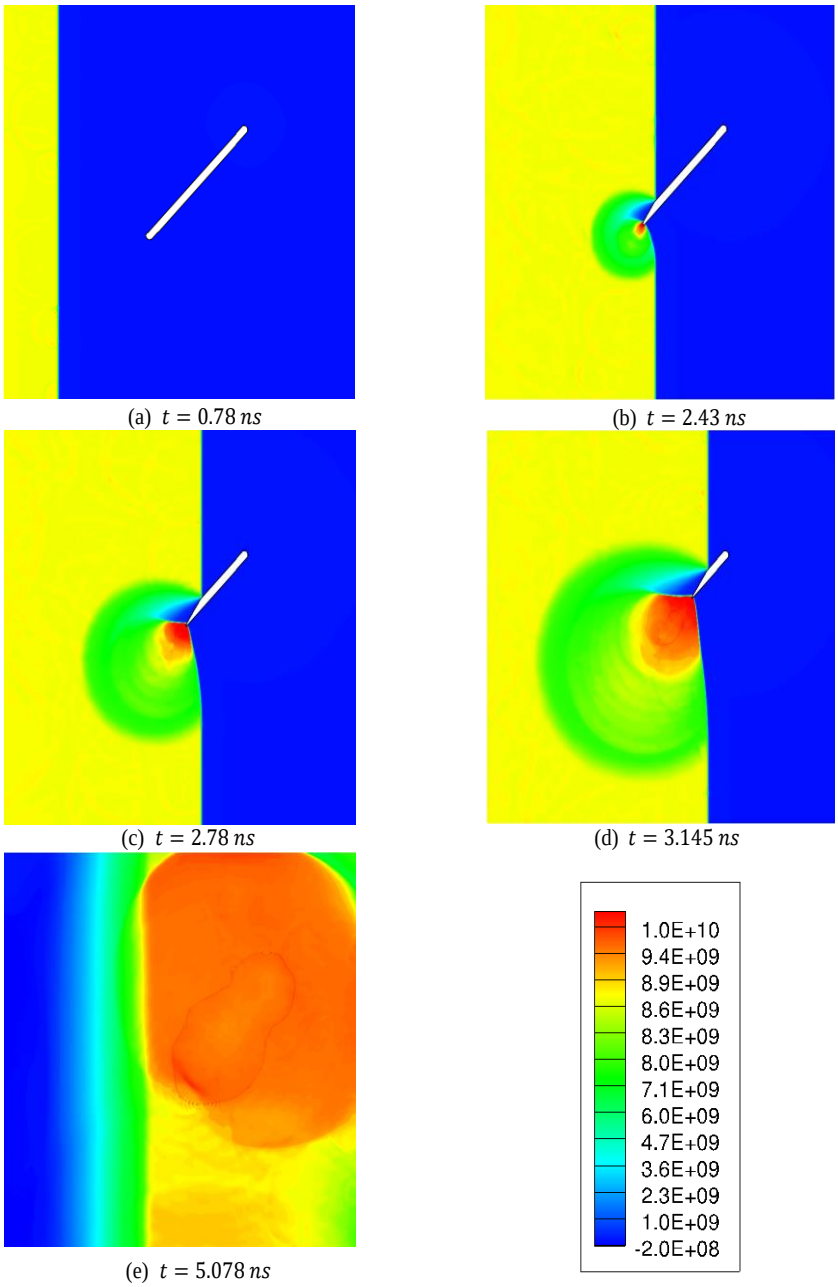


Figure 4-13: Pressure (Pa) contour plots obtained from the shock analysis on the elongated void in HMX with $1000\ m/s$ shock speed and $0.01\ \mu s$ duration. The elongated void is aligned 45° with respect to the incident shock.

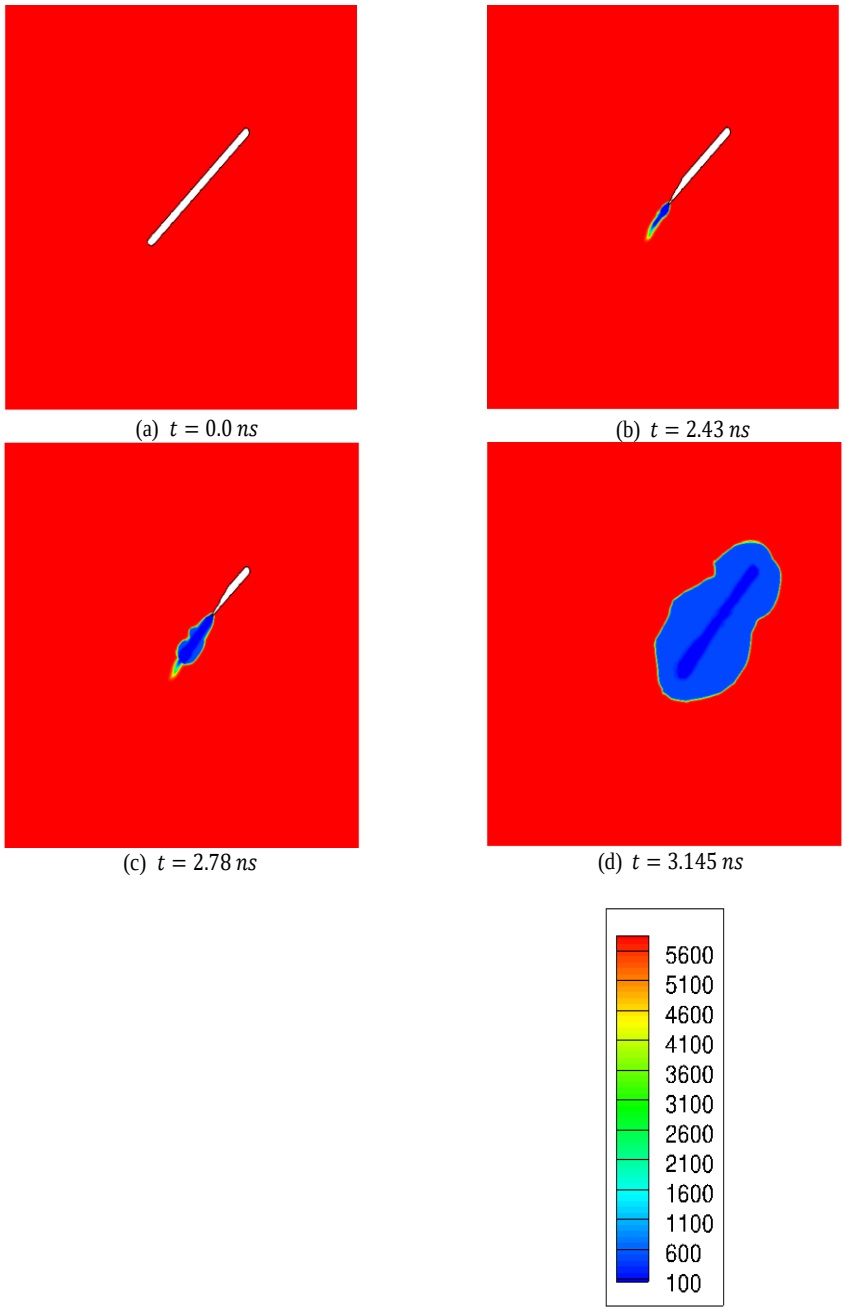


Figure 4-14: $\beta - HMX$ concentration$(mol/m^3)$ contour plots obtained from shock analysis on the elongated void in HMX with $1000\ m/s$ shock speed and $0.01\ \mu s$ duration. The elongated void is aligned 45° with respect to the incident shock. The plots show the complete decomposition of solid $\beta - HMX$ to gaseous products at the hot spots where ignition takes place.

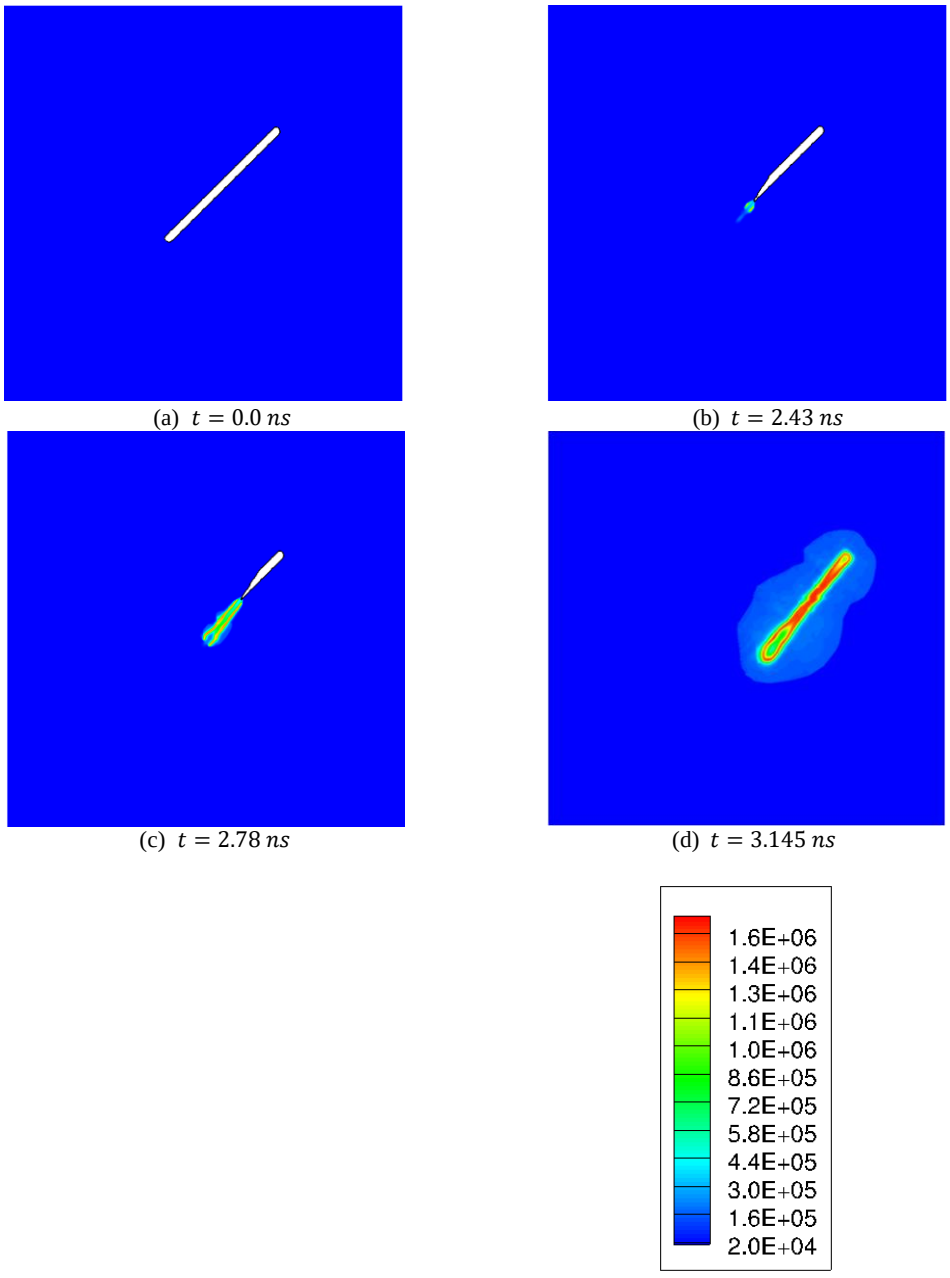


Figure 4-15: HCN concentration($mol/m^3$) contour plots obtained from shock analysis on the elongated void in HMX with 1000 $m/s$ shock speed and 0.01 μ$s$ duration. The elongated void is aligned 45° with respect to the incident shock. The plot shows the complete decomposition of solid $\beta - HMX$ to gaseous products like HCN at the hot spots where ignition takes place.

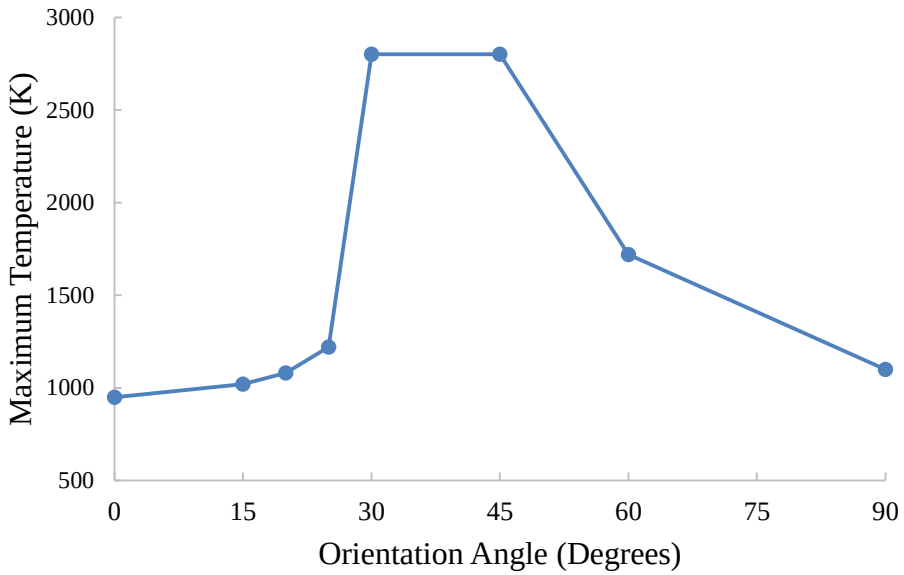


Figure 4-16: Variation of maximum temperature obtained in simulation with orientation angle of the elongated void. The orientation angle of the elongated void is measured with respect to the incident shock direction. The elongated voids with orientation angle lying between $30° - 50°$ are lying in the critical zone where reaction can initiate.

# CHAPTER 5

# SHOCK LOAD ANALYSIS ON PLASTIC BONDED EXPLOSIVES

## 5.1.Introduction

The presence of heterogeneities in energetic materials like PBX, mock sugar explosives etc. can influence its sensitivity towards shock initiation and ignition. Shock interaction with these heterogeneities leads to the formation of local high temperature zones also known as hot spots. It is important to estimate the geometrical feature of these heterogeneities for the accurate estimation of the hot spots which can effect the ignition threshold of energetic material. The current framework uses the image processing approach discussed in chapter 2 for representation of the microstructure geometry. In this work, shock analysis on the image derived geometry of the mock sugar explosive is studied in both two and three dimensions. The shock analysis is purely inert and chemical reactions are not considered in the present calculations for the sake of simplicity of the problem. Three different problems has been considered here,

1. Shock analysis on 2D mock sugar explosive under shock load of $500\ m/s$
2. 2D shock analysis on mock sugar explosives under $1000\ m/s$ shock load
3. Shock analysis on three dimensional mock explosive geometry under $500\ m/s$ shock load.

## 5.2.Two dimensional shock analysis on mock sugar explosive sample

A 2D section of the mock sugar explosive image is considered in the current analysis to perform shock analysis. The image intensity field is shown in Figure 5-1(a) and it is characterized by 1024 ×512 pixels. The image processing framework developed in the current work is used for the level set representation of the mock sugar microstructure geometry containing HMX crystals embedded in Estane binder.

Firstly, image denoising algorithm i.e. SRAD[92] in the current framework is applied on the 2D image section. SRAD removes the speckle noise present in the image and gives a smoother image as shown in Figure 5-1(b). The active contour image segmentation method[93] is then applied on the denoised image to generate the level set representation of the geometry. The level set boundary is superimposed on the original image to represent the accuracy of the geometry representation and is shown in Figure 5-1(c). However, the level set field obtained from active contour segmentation is not a signed distance function as it is a function of the image intensity field. Hence, reinitialization algorithm with subcell fix[94] is applied on the active contour level set field to obtain a signed distance field.

The physical dimension of the mock sugar geometry is 4mm×2mm. The grid spacing, $\Delta x$ used for the shock analysis is 0.004 mm. The level set field generated in the image domain is mapped to the computational domain with 1000 ×500 grid points using the bilinear interpolation algorithm. A shock pulse of 500 m/s speed and 0.04 μs duration is passed from the west of the domain boundary of the computational domain shown in Figure 5-1(d).

The density, pressure and temperature contour for shock pulse of 500 m/s is shown in Figure 5-2-Figure 5-4. It can be seen from Figure 5-2, that as shock passes through the material there is increase in the density for both HMX and estane binder due to the shock compression which leads to the shock heating of the crystals and rise in temperature as shown in Figure 5-3.

In order to demonstrate the capability of the current numerical framework of handling large deformation and high strain rate, shock pulse loading of 1000 m/s of duration 0.04 μs is applied from the west boundary of mock sugar explosive of Figure 5-1(d). The density, temperature and pressure variation plot for the analysis is shown in Figure 5-5Figure 5-7 . For 1000 m/s shock speed, the deformation of the crystal is large and the temperature rise is high due to strong compression. Also, there is localization of

energy near the HMX- estane interface which manifests in high temperature at those regions and can be seen in Figure 5-6. These regions can act as a potential site for hot spot formation and triggering chemical reactions.

## 5.3.Three dimensional shock analysis on mock sugar explosive sample

Shock analysis on a 3D geometry of mock sugar explosive is performed. The 3D sample is obtained by stacking 2D image sections of the mock sugar geometry in the physical space. The geometrical representation of mock sugar explosive is shown in Figure 5-8(a). The 3D sample is characterized by $64$ pixels in each directions. The image processing algorithms are applied on the sample to obtain the level set representation. The sample consists of speckle noises and it requires noise reduction. SRAD[92] algorithm as discussed in chapter 2 is applied on the 3D sample of mock sugar explosive for noise reduction. The results from SRAD is shown in Figure 5-8(b). It can be seen that significant noise reduction is obtained while preserving the edges of the objects present in the sample. After noise reduction, active contour algorithm[93] is used to segment the 3D geometry for level set geometrical representation. The level set field obtained after segmentation is reinitialized and mapped to the physical domain of the explosive sample. The physical dimension of the sample is $1mm \times 1mm \times 1mm$ as shown in Figure 5-8(c). The grid spacing for the computation is 0.01 mm to generate 100 grid points per dimensions. Shock wave of speed $500\ m/s$ is applied from the west face of the domain. The velocity is held constant at the west boundary. The density and temperature contour plots from the shock analysis is shown in Figure 5-9 and Figure 5-10.

Figure 5-9 shows that as shock wave load the material, there is density increase due to compression in both HMX and binder. The HMX crystals undergoes plastic deformation and performs plastic work. The temperature contour (Figure 5-10) shows the bulk increase in temperature of both HMX and binder due to compression work. However, the

temperature rise of the HMX crystals is more than binder because of plastic work involved in the deformation of the crystals. Although, there is increase in temperature in the material i.e. around 400-500 K, there are no hot spot formation involved which can creates a localized high temperature zone. It is more likely from this simulation, chemical reaction will not initiate.

From both 2D and 3D simulations, it was observed that shock loading leads to bulk heating of both HMX crystals and binder, however there are not hot spots formed. Also, even increasing the shock strength, there is not significant rise in temperature which could cause initiation of chemical reactions. This is not a consistent observation for heterogeneous energetic materials. The current inconsistent behavior prediction is related to the way image processing algorithm models the real microstructure of the geometry. The image processing algorithm is modeling the explosive samples as a two phase material, however, in the real microstructure there are voids presents too. It was observed previously, presence of voids can increase the sensitivity of the materials. Hence, the current framework needs to be improvised in order to handle 3 phase material representation using level sets.

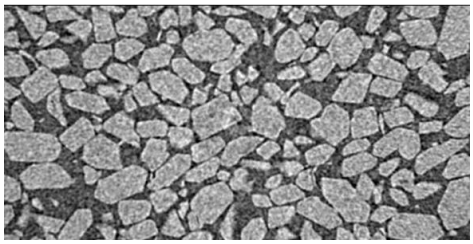

(a) Intensity field of 2D image section of mock sugar explosive

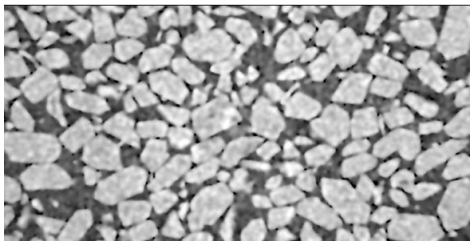

(b) Intensity field obtained after SRAD with parameter $\lambda = 1.0$

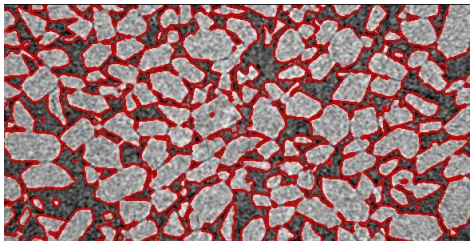

(c) Level set representation of the crystal boundaries obtained after active contour segmentation

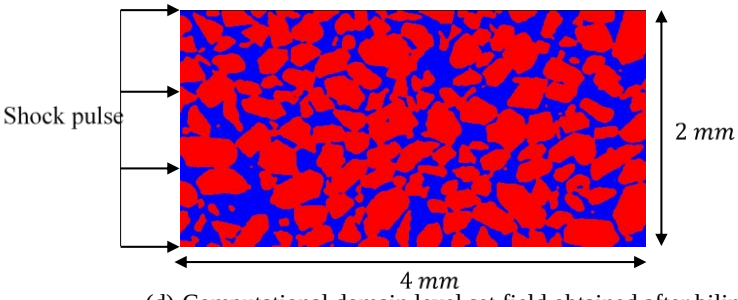


(d) Computational domain level set field obtained after bilinear mapping from the image domain level set field

Figure 5-1: Two dimensional section of the mock sugar explosive microstructure containing HMX crystals embedded in the Estane matrix represented by level set field obtained by applying SRAD, active contour segmentation and reinitialization with subcell fix algorithm on the image intensity field. The level set field is mapped back to the computational domain of size $4mm \times 2mm$ and shock pulse is applied from the west domain boundary.

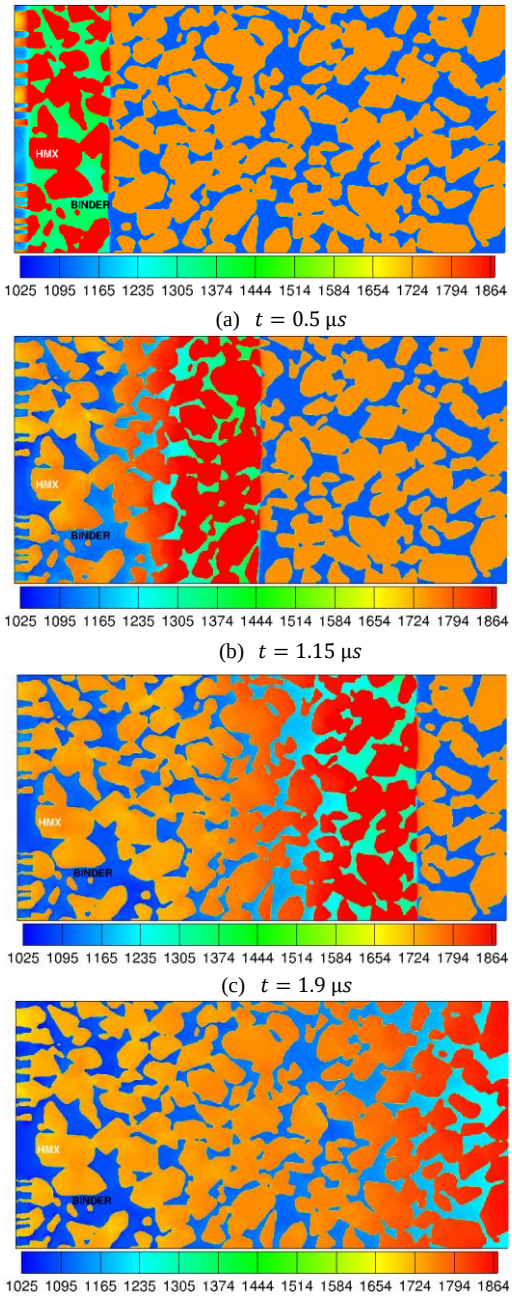


Figure 5-2: Density($kg/m^3$) variation plot at different time for the shock pulse loading of 500 $m/s$ on mock sugar explosive sample.

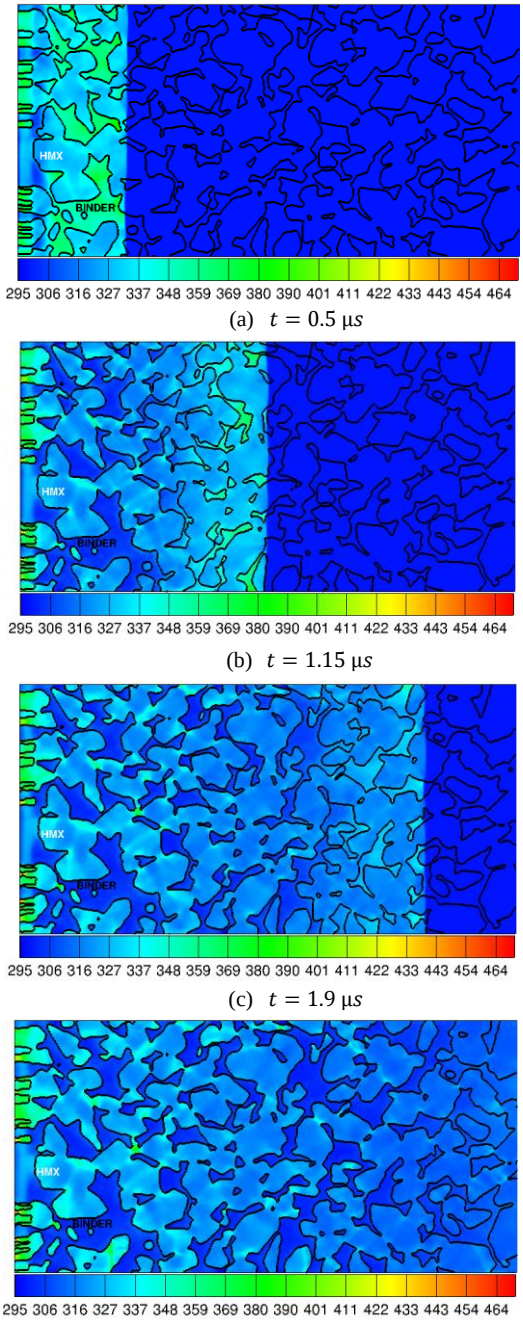


Figure 5-3: Temperature (K) variation plots at different times for the shock pulse loading of $500\ m/s$ on mock sugar explosive sample.

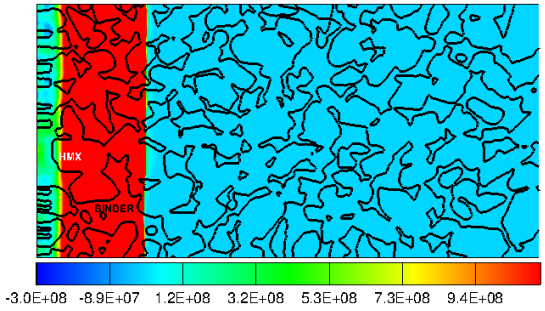


(a) $t = 0.5\ \mu s$

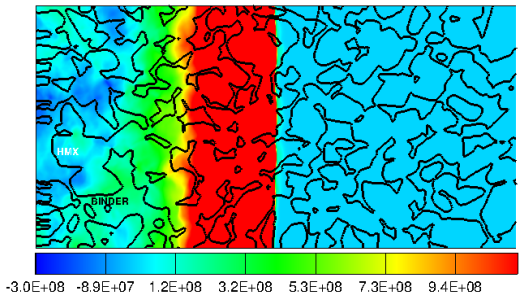


(b) $t = 1.15\ \mu s$

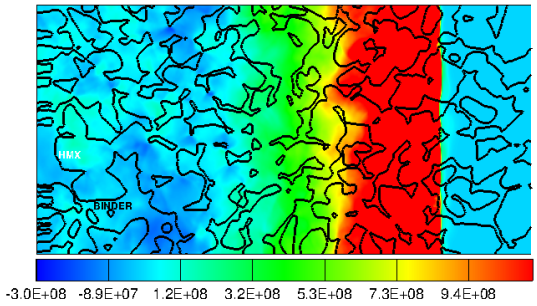


(c) $t = 1.9\ \mu s$

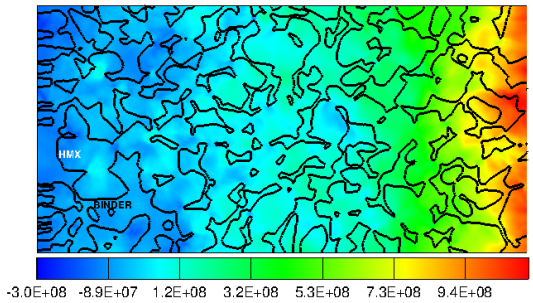


(d) $t = 2.7\ \mu s$

Figure 5-4: Pressure (Pa) variation plot at different time for the shock pulse loading of 500 $m/s$ on mock sugar explosive sample.

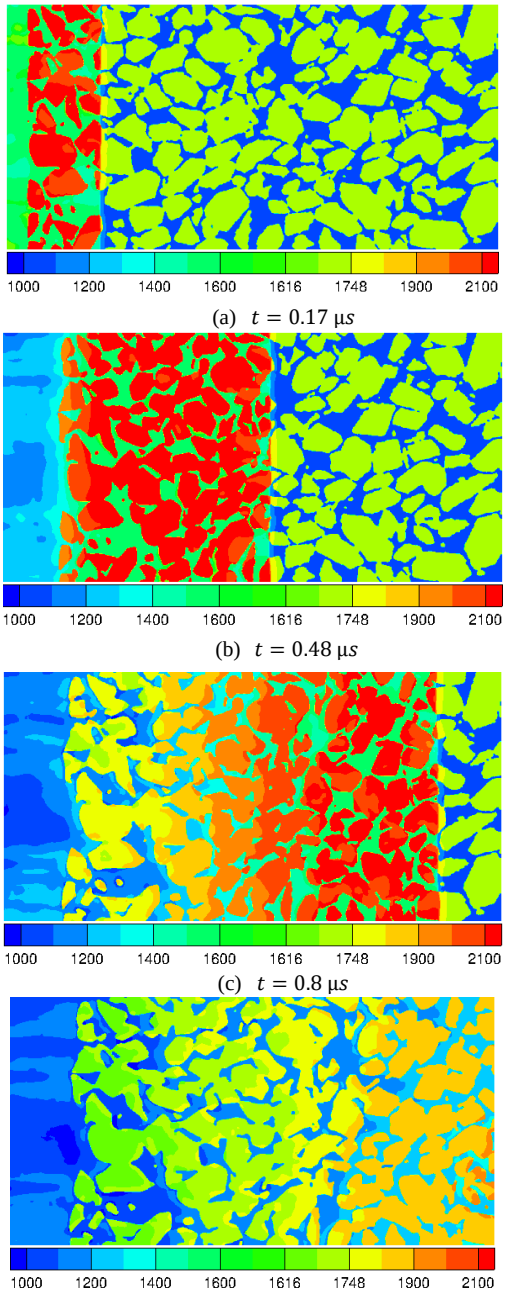


Figure 5-5: Density($kg/m^3$) variation plot at different times for the shock pulse loading of $1000\ m/s$ on mock sugar explosive sample.

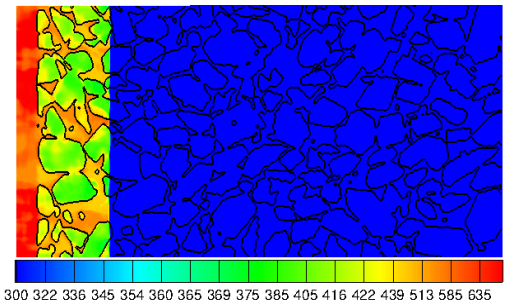


(a) $t = 0.17\ \mu s$

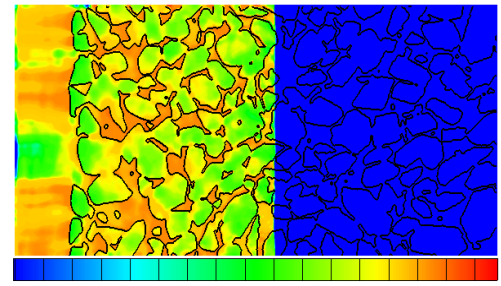


(b) $t = 0.48\ \mu s$

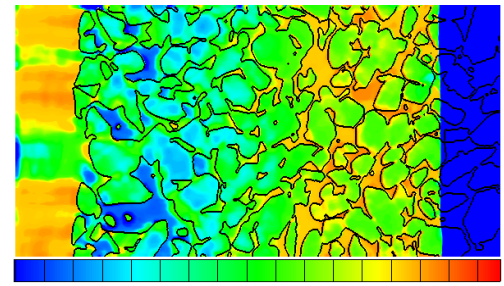


(c) $t = 0.8\ \mu s$

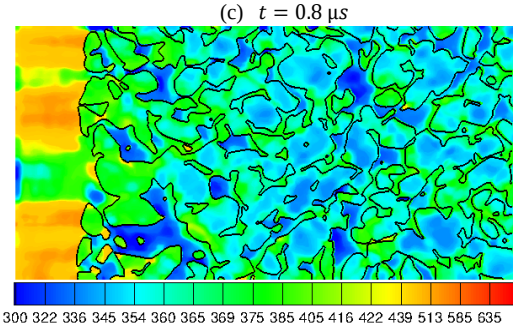


(d) $t = 1.53\ \mu s$

Figure 5-6: Temperature (K) variation plot at different times for the shock pulse loading of $1000\ m/s$ on mock sugar explosive sample.

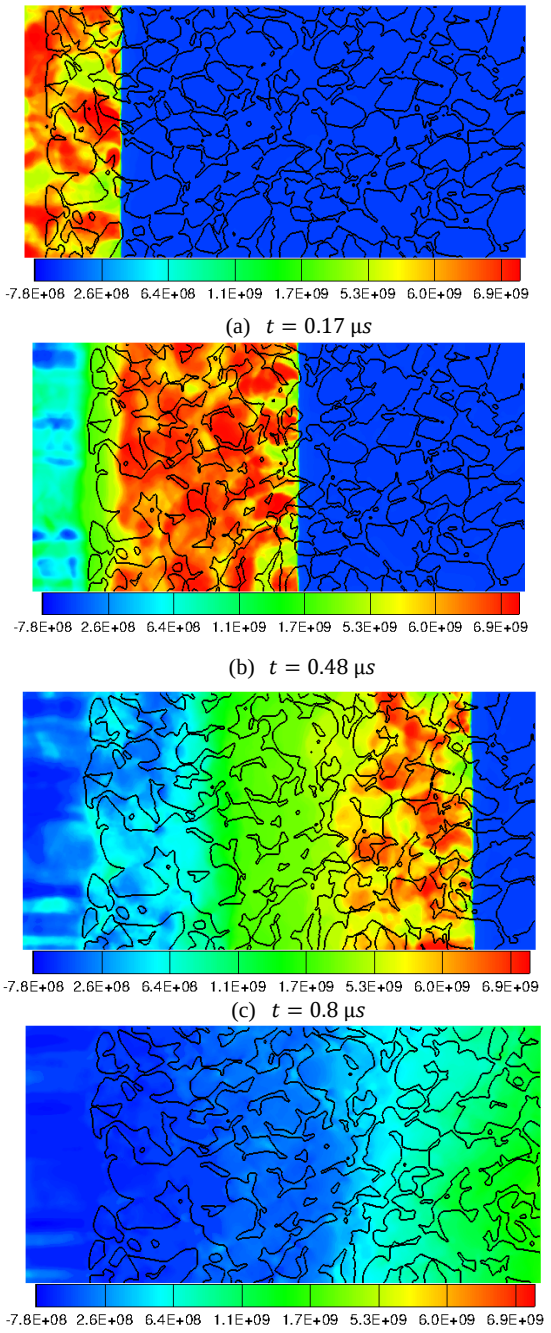


Figure 5-7: Pressure (Pa) variation plot at different times for the shock pulse loading of 1000 $m/s$ on sugar mock explosive sample.

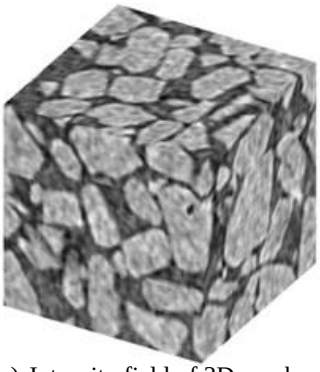

(a) Intensity field of 3D mock sugar explosive sample

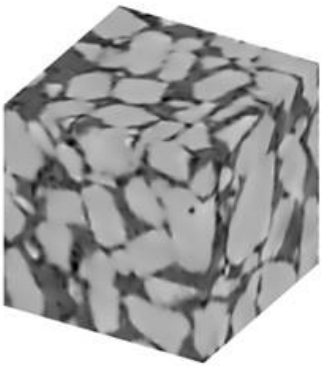

(b) Intensity field obtained after SRAD with parameter $\lambda = 1.0$

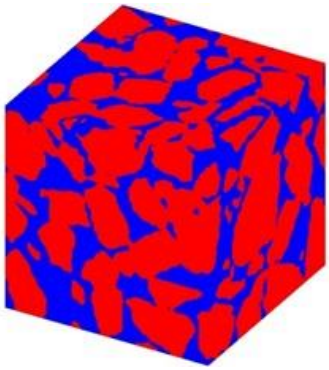

(c) Level set representation of the crystal boundaries obtained after active contour segmentation

Figure 5-8: Three dimensional geometry of the mock sugar explosive microstructure containing HMX crystals embedded in the Estane matrix represented by level set field obtained by applying SRAD, active contour segmentation and reinitialization with subcell fix algorithm on the image intensity field. The level set field is mapped back to the computational domain of size $1mm \times 1mm \times 1mm$ and shock pulse is applied from the west domain boundary.

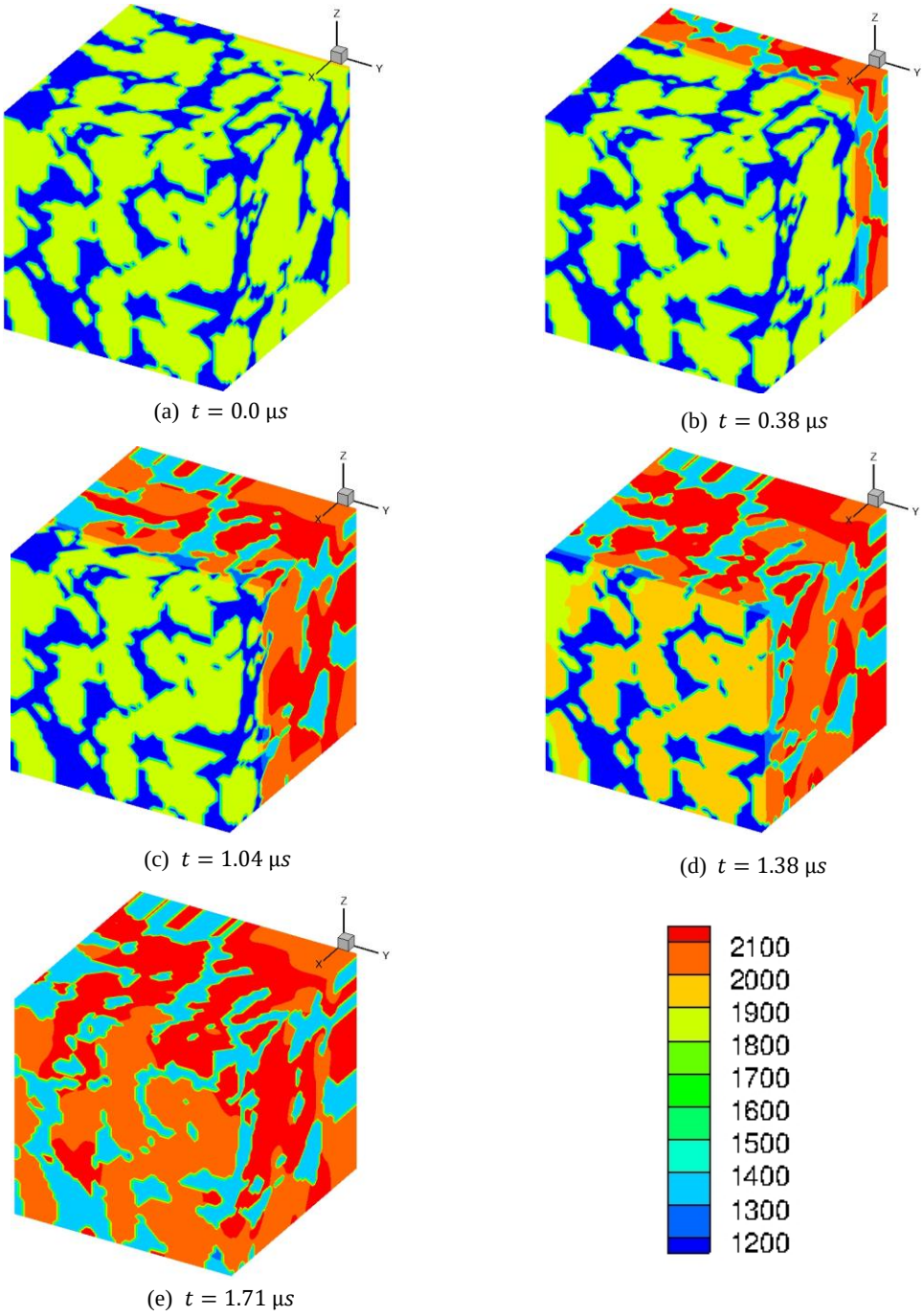


(a) $t = 0.0\ \mu s$

(b) $t = 0.38\ \mu s$

(c) $t = 1.04\ \mu s$

(d) $t = 1.38\ \mu s$

(e) $t = 1.71\ \mu s$

Figure 5-9: Density($kg/m^3$) variation plot at different time from 3D shock analysis with shock loading of 500 $m/s$ on mock sugar explosive sample.

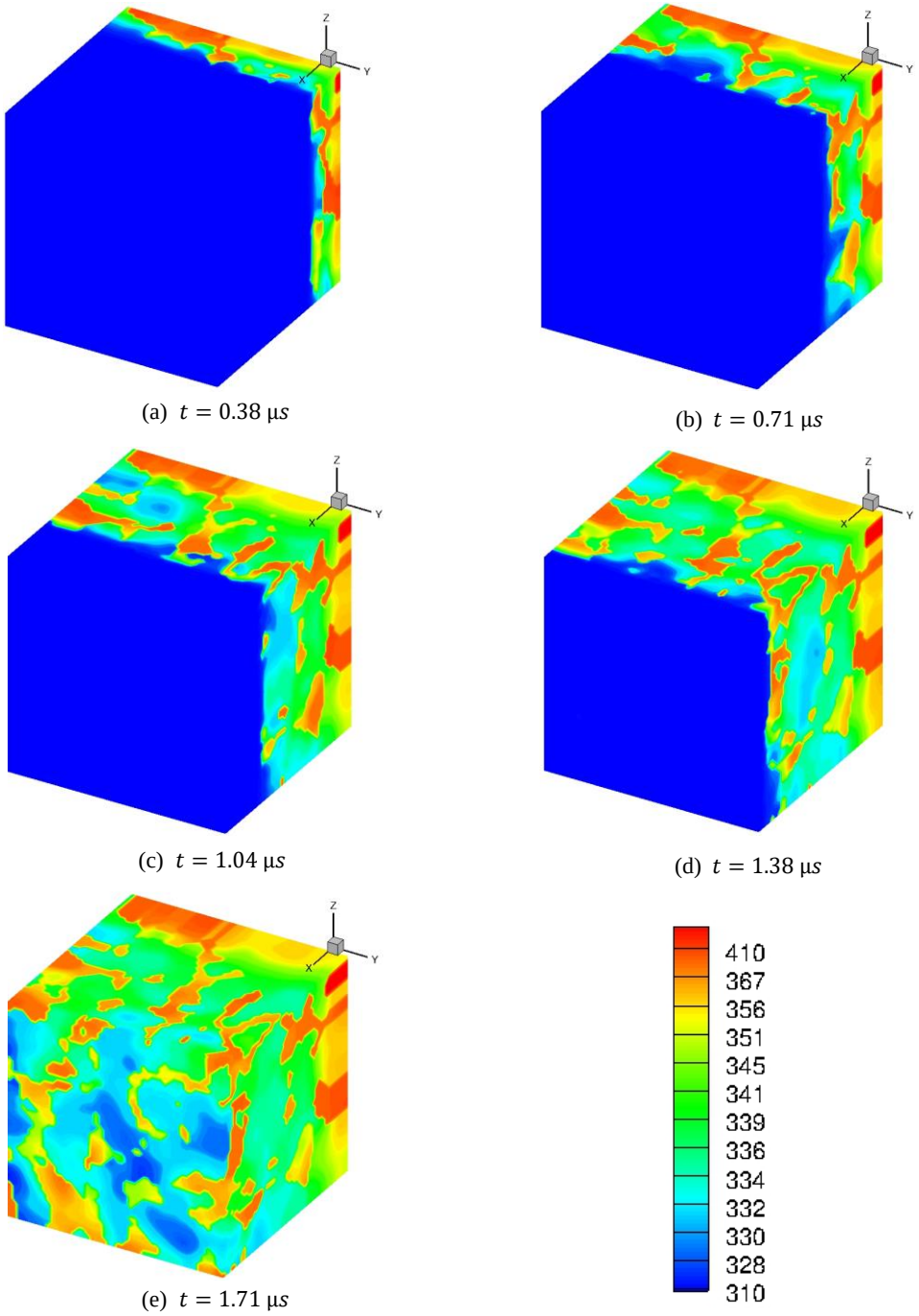


(a) $t = 0.38\ \mu s$

(b) $t = 0.71\ \mu s$

(c) $t = 1.04\ \mu s$

(d) $t = 1.38\ \mu s$

(e) $t = 1.71\ \mu s$

Figure 5-10: Temperature (K) variation plot at different time from 3D shock analysis with shock loading of $500\ m/s$ on mock sugar explosive sample.

# CHAPTER 6

# MULTIMATERIAL CONTACT IMPACT PROBLEMS

## 6.1. Introduction

High speed impact leading to large deformation, penetration and fragmentation arises in many applications including munition-target interaction[98, 99], geological impact dynamics[100, 101], shock-processing of powders[102, 103] etc. In these situations large deformations of materials are produced due to the propagation of nonlinear elasto-plastic shock waves generated due to the impact. Numerical simulation of impact problems involving multimaterial interactions demands accurate implementation of interfacial conditions at the region of impact. In Eulerian multimaterial impact formulations[104] material interface treatments assume an artificial bonding between the impacting interfaces of the adjacent materials because of the presence of a continuous normal velocity field at material interfaces. Due to this, problems in which impact, separation and sliding of materials play an important role in the dynamics are not well handled in Eulerian methods. On the other hand, Lagrangian methods handle contact and separation rather naturally because of: a) explicit tracking of interfaces, b) the presence of independent velocity fields in the interacting materials and c) the kinematic contact constraints which couple the independent fields at the impacting surface. However, in Lagrangian techniques detecting contact between surfaces can pose challenges and maintaining "good" meshes in the course of large material deformations can be onerous. Because Eulerian methods operate on fixed meshes while the materials flow through the fixed (typically Cartesian) meshes, these aforementioned difficulties with Lagrangian techniques are mitigated. Therefore, an approach that combines the desirable features of Eulerian and Lagrangian methods for handling multimaterial interactions involving contact and separation would be highly useful. This paper describes such an approach in a sharp interface Eulerian framework [72, 89, 105] that avoids problems associated with Lagrangian mesh management while clearly

delineating interacting material interfaces and applying local contact-separation conditions.

To handle the problem of large deformations, an Eulerian formulation is an appealing choice compared to a Lagrangian approach as problems related to mesh distortion and remeshing of the domain can be avoided in the Eulerian setting. However, both the formulations suffer from their own strengths and weaknesses in high strain rate problems. The relative advantages and disadvantages of both the formulations have been discussed by Anderson[106]. In the field of contact mechanics, much work has been done in the Lagrangian when compared to the Eulerian framework. In the regime of high speed impact, a two-dimensional finite contact algorithm developed by Taylor and Flanagan[107] for the PRONTO2D explicit dynamics code is a common starting point. This algorithm has the capability to handle impact and separation of materials for frictionless as well as frictional contact. The algorithm uses the master-slave approach to designate impacting bodies. It is a two-step method in which first a predictor step predicts the nodal positions, velocities and acceleration of the master body and then the corrector step calculates the force required to prevent the penetration of master body into the slave body. This model has been used in the regime of high strain rate problems as in the work of Camacho and Ortiz[108]. The Lagrangian contact algorithm by Benson and Hallquist[109] developed for DYNA2D ( a nonlinear explicit finite element software) is also well known for its capabilities to handle mechanical interaction of two bodies or self-contact in the same body. This contact algorithm has been used in the work of Batra and Stevens[110]**.** Also, Belytchko et. al.[111] proposed a new contact detection algorithm in the Lagrangian framework based on the moment method in meshfree discretization that can handle general contact situations.

In Eulerian multimaterial impact computations the treatment of contact, separation and sliding is not as well developed as in the Lagrangian case. One of the notable works by Benson[112, 113] to handle both frictionless and frictional contact in an Eulerian

framework using a mixture theory approach shows the capability of handling impact and separation of materials. The mixture theory has been used to calculate the mean stress at the interface between the interacting materials. The nonlinear contact constraint equations have been solved to impose the constraints for friction, frictionless sliding and separation. Mixture theory based approaches hinge on the proper physical treatment of the materials residing in the mixed cells and on ascribing suitable continuum models for the mixed materials. Assumptions of local equilibrium in the mixed cells must be invoked, and the problems of coexisting materials of vastly different impedances inside one element must be addressed. The work of Vitali and Benson[114-116] using extended finite element method (X-FEM) in arbitrary Eulerian Lagrangian (ALE) formulations overcomes problems associated with mixture theories in handling sliding and separation and shows the capability of handling friction and frictionless contact. In these works, the limitation of mixture theory vis-à-vis the prediction of spurious stresses in mixed material elements has been overcome by creating independent velocity fields for the impacting materials in an X-FEM framework which allows local enrichment in the mixed material elements. Frictional and frictionless sliding has been handled by obtaining independent velocity and acceleration fields in the individual interacting materials at the region of impact. Separation between the different materials has been handled by introducing void material between the impacting materials once the mean stress at the interface becomes tensile. Also, the work by Vitali et. al.[117] to impose interfacial contact conditions using extended Eulerian formulation (XEM) shows the capability of handling frictionless sliding with separation in Godunov formulations.

The approach taken in this work is different from that in Vitali and Benson in that the current formulation is purely Eulerian, i.e. no Lagrangian phase (as in ALE) is involved. The interfaces are tracked using level sets[90, 91], which means that they can be maintained in a sharp fashion, i.e. this is effectively an interface tracking approach rather than an interface reconstruction based on volume fractions. No mixture of materials at any stage of

material-material interactions is involved as the sharp interface approach maintains the materials as separate entities delineated by two individually tracked level set functions. The use of level set distance function for the representation of interfaces also simplifies the collision detection algorithm since information on distances between potentially interacting boundaries is implicitly and always available from the level set fields. Boundary conditions on the sharply separated and interacting sub-grid interfaces are incorporated implicitly using a modified ghost fluid method (MGFM)[95, 118, 119]. Since boundary conditions at the interface are satisfied implicitly using ghost fluid method (GFM), there is no need to solve additional non-linear equations to impose the contact constraints. The use of GFM to handle boundary conditions helps to create independent velocity fields in each material and frictionless sliding can be handled by coupling these fields at the interacting interfaces. In this framework, much like in the explicitly tracked Lagrangian contact formulations, separation between the materials occurs as a natural process of deformation, i.e. separation is not enforced by introducing a void phase in a mixed material but occurs simply as the consequence of evolving the sharp interfaces. This algorithm is purely local in implementation and can be used in a parallel computing framework[120] and can be easily extended to three dimensions.

In previous works [72, 73, 75, 89] simulation of multi-material impact problems involving collision between the materials followed by large deformation, penetration and fragmentation were performed. However the contact treatment was rudimentary in that once materials impacted they remained in contact in the course of further interaction. This enforced prolonged contact of the materials leads to physically unrealistic results in certain type of problems where separation between the materials plays an important role. For example, in a flyer plate impact simulation separation between the plates plays an important role in the wave physics[121]. Also, in the ricochet of a projectile from a target separation and sliding of the projectile plays a crucial role in the dynamics of both the projectile and the target[122]. Hence, to model these situations accurately appropriate

boundary conditions need to be applied along with the contact conditions at the interacting interfaces. The contact model is tested on different types of multimaterial impact problems which involves impact and separation of materials at high strain rate.

## 6.2.Results

The performance of the contact algorithm is tested for different situations involving planar and oblique impact. Three problems where the collision and separation of the materials are involved have been shown in the current work, viz;

1. Planar impact between two deformable bodies which is shown by simulating the flyer plate impact problem.
2. Planar impact between a deformable body and a rigid body which can be seen in the simulation of a Taylor Bar problem.
3. Oblique impact at 10 degree angle of attack between a projectile and a target leading to ricochet of the projectile.

### 6.2.1 Flyer plate simulation

The numerical simulation of a plate impact experiment has been used in the past to study the phenomenon of spall fracture [121, 123-125]**.** A complete description along with the experimental results for spall fracture has been given by Antoun et. al.[123]. Plate impact simulation for the study of spall fracture involves the planar impact and separation of the flyer and the target plates and hence a contact model plays an important role in capturing the wave physics accurately. In this work the flyer plate simulation has been performed without including the spall phenomenon and is therefore realistic only up to the point of incipient spall at the lower surface. The simulation is performed with the proposed contact model for three different cases in order to validate the wave propagation phenomena in the interacting materials in the period prior to and following separation of the impactor from the target. In the first case, the acoustic impedance of the flyer plate is less than that of target plate; in the second case the flyer plate is of higher acoustic

impedance and in the third case the acoustic impedance of the flyer and the target plates are the same. The interaction of the shock waves in these three cases has been discussed in the following.

6.2.1.1 Acoustic impedance of the flyer plate is less than target plate

In this case the acoustic impedance of the flyer plate (Aluminum) is less than the target plate (Copper). The details regarding the plate's geometric configuration , material properties and the flyer plate velocity have been taken to simulate experimental data(experiment B-61)[126]. The plates are cylindrical in shape as shown in Figure 4-1(a); this allows use of the axisymmetric computational geometry as shown in Figure 4-1(b). The simulation duration is$10\ \mu s$. The dimensions of the plates along with the impact velocity are tabulated in Table 6-1.

As shown by theoretical analysis of the wave propagation phenomena in flyer plate impact[123] **,** after the impact takes place shock waves of equal magnitude are generated in both plates. The shock wave in the flyer plate travels into the impactor and interacts with its free surface; due to this interaction, reflection of the wave at the free surface of the flyer takes place which gives rise to the formation of a returning rarefaction wave. This rarefaction wave passes through the flyer plate and interacts with the impacted surface which leads to the formation of tensile stress conditions at the impact interface. Due to this tensile state at the impacted interface the separation of flyer from target plate takes place as seen in Figure 6-2(b). The configurations of the plates before and after the simulation are seen in Figure 6-2 which shows that the contact model was able to handle the impact and separation of the materials.

To validate the results obtained from the simulation, the bottom free surface velocity at a point which is $10\ mm$ from the center of the target plate is compared with available experimental results. The plot is shown in Figure 6-3. The peak velocity at the bottom free surface of the target plate matches well with the experimental data. The graph

has been plotted till $t = 0.3\ \mu s$ because after this the effect of spall fracture comes into play. Since we are not using a damage model to study spall fracture in this work the free surface velocity profile obtained from the current work deviate from the experimental results after $t = 0.3\ \mu s$. Grid convergence study has been performed using four different grid sizes viz.,$\Delta x = 0.2mm,\ 0.1mm\ 0.05\ mm$ and $0.03\ mm$ respectively. The bottom free surface velocity for the grid sizes of $\Delta x = 0.1mm, 0.05\ mm$ and $0.03\ mm$ at a point $10\ mm$ from the center of the plate has been shown in Figure 6-4 along with the experimental results. This shows the convergence of the contact model as the grid is refined. Also, the peak velocity at the bottom free surface has been considered to calculate an error measure for the four different grid sizes. The error measure is defined as

$$\varepsilon = \frac{\left|V_{coarse} - V_{finest}\right|}{V_{finest}} \tag{6.61}$$

where, $V_{coarse}$ is the peak velocity at the bottom free surface for the coarse grid and $V_{fine}$ is the peak velocity of the finest grid with a grid spacing of $0.03\ mm$ in this case. The four different grid sizes of $\Delta x = 0.2mm, 0.1\ mm,\ 0.05\ mm$ and $0.03\ mm$ have been considered. The error measure plot with different grid sizes has been shown in Figure 6-5. As seen in the figure the error in calculated bottom surface velocity converges with grid refinement with a near second-order convergence behavior.

6.2.1.2 Acoustic impedance of the flyer plate is greater than target plate

The contact treatment is tested next for the case where the acoustic impedance of the flyer plate is greater than the target plate. The impact velocity and plate dimensions remain same as the previous case, but now the flyer plate is Copper and the target plate is Aluminum. The stress-velocity diagram [123] shows that in this case the impacting interface maintains a compressive state throughout the impact and hence both plates should remain in contact and no separation of target and flyer plate is expected. The wave physics

involved in this situation is different from the previous one and thus the ability of the present algorithm to accurately portray expected physical behavior is demonstrated through this case.

After the impact takes place an initial shock wave of equal magnitude is generated in both target and projectile in order to maintain the stress and velocity continuity at the impacted interface and denoted as shocks S(Cu) and S(Al) in Figure 6-6(a). As the thickness of the flyer plate is less than the target material, the shock wave in the projectile, i.e**.** S (Cu), travels upward and interacts with the free boundary of the flyer plate where it is then reflected as a release wave. This release wave returns to the impact surface and interacts with the target again to generate a shock wave in the flyer plate and a rarefaction wave in the Aluminum target plate as shown in the Figure 6-6(b). The wave reflection at the free surface of the Copper flyer plate and its interaction with the impacted surface leads to the generation of successive rarefaction waves in the target, i.e. R2, R3 etc. shown in Figure 6-6(c) and Figure 6-6(d). These rarefaction waves eventually unload the target material to equilibrium. During the course of these interactions the flyer and target never separate, as expected from the physics of the problem[123].

6.2.1.3 Acoustic impedance of the flyer plate is equal to target plate

Previous studies of attenuation of shock waves in solids have been conducted for flyer plate impact[127, 128] with the use of the same material for the flyer and the target plates. In this situation, first a shock wave is produced in both flyer and target due to the impact which is the same as in the previous two situations. Once the shock wave propagates into the flyer plate and reaches the rear free surface of the flyer, it reflects as a rarefaction wave which propagates towards the target and unloads the flyer plate to zero stress state. Once this rarefaction wave reaches the impacted interface, it passes through the interface completely because both the materials are of equal impedance. Now, the rarefaction wave

moves through the shock compressed portion in the target plate and it eventually overtakes the initial shock front and leads to the attenuation of the shock wave.

In order to capture this wave physics of attenuation of shock waves, numerical simulation has been performed for the impact between Aluminum-Aluminum plates. The dimension and impact velocity is taken from the work by Fowles[129] in order to compare the simulation results. The variation of peak pressure with the target plate location is shown together with the numerical results from[129] in Figure 6-7. As can be seen in the figure the computed and theoretical values are in good agreement through the wave interaction process.

It is evident from the results above that the shock wave attenuates while traveling in the target plate. The attenuation begins after the wave has travelled a certain distance inside the material. This is in agreement with the expected physics since the attenuation is caused by the rarefaction wave which returns from the free surface of the flyer plate and catches up with the shock wave in the target plate. This case demonstrates that the contact algorithm is able to handle wave interactions at the interfaces accurately.

### 6.2.2 Taylor bar impact simulation

The simulation of Taylor bar impact is performed in order to assess the performance of the proposed contact model in the situation where a deformable body collides with a rigid body. The bar is made of Tungsten heavy alloy and the test configuration and dimension of the bar is shown in Figure 6-8. The dimension and impact speed of the bar as shown in Figure 6-8 have been taken from the work by Batra and Stevens[110]. The grid spacing of $\Delta x = 0.1\ mm$ has been used for this problem in both the directions; this grid spacing has been used to yield a grid independent solution for the current simulation.

The Taylor bar impact simulation results in the deformed configuration shown in Figure 6-9; contours of effective plastic strain are also shown in the figures. It is evident that due to the development of tensile stress conditions and upward velocity at the bottom

of the bar along the outer periphery, the ends of the bar lift off the rigid target and curl upward. The bar radius at the foot and maximum equivalent plastic strain at time $10$ μs and $50$ μs for present calculation have been compared with the solutions obtained from Batra and Stevens[110] and is shown in Table 6-2. Also, the contours of effective plastic strain at time $50$ μs for current simulation and solutions obtained from Batra and Stevens[110] is shown in Figure 6-10. The numerical results are in good agreement. This shows the capability of the proposed contact model to handle the collision and separation of a deformable body over a rigid surface.

### 6.2.3 Oblique impact between two deformable bodies

The problem involving an oblique impact of two bodies is important in practical applications. The phenomenon of ricochet of a projectile over the target has been analyzed in the past to simulate the oblique impact problem[122, 130]. When ricochet results in the situation depicted in Figure 6-11, there is a sustained interaction between the projectile and the target throughout which the projectile is deflected away and separates from the target. Thus, this case is a stringent test of the ability of the current contact scheme to effect contact-separation behavior in the present sharp interface Eulerian setting. In order to assess the ability of the contact algorithm to handle oblique impact situations and to capture ricochet phenomena, a high strength steel projectile is impacted on a Tungsten heavy alloy (WHA) target. The angle of impact is $10°$ and the impact velocity is$1000\ m/s$. The length to width ratio for the projectile is $10.7$ as used in previous work [122]. The grid spacing is $0.2$ *mm* for this simulation. The configuration for the simulation is shown in Figure 6-11. The deformation of the projectile at different times is shown in Figure 6-12.

In this case the contact model is able to predict the sliding between the projectile and the target and the lift-off of the projectile from the target. From Figure 6-13 it can be seen that there is only a modest change in the horizontal velocity during the entire process which explains why momentum loss of the projectile in this case is not significant. The

vertical velocities developed due to the impact and ricochet interaction are small compared to the horizontal velocity. Also, the angle with which projectile leaves the target surface is found out to be approximately 9° for the present angle of incidence of 10°. Hence, the angle with which projectile impacts the target is almost the same with which it leaves, which shows the capability of the contact model to handle impact, sliding and separation in the case of inclined impact.

## 6.3. Conclusions

A frictionless contact algorithm for a well-established sharp-interface Eulerian high speed multi-material solver is implemented to handle impact and separation of materials. The advantage of the model lies in its ease of implementation; in contrast to Lagrangian contact treatments search operations for detecting collisions are simplified by the use of level sets and no local constraints to prevent interpenetration through penalty-type force application is necessary to separate interfaces. Since the framework is Eulerian difficulties associated with carrying meshes through the material interactions, managing meshes to retain solution accuracy and stability and detecting contact between interacting surfaces are circumvented. The contact conditions are handled by implicitly satisfying the interfacial conditions on the parts of the interacting material interfaces that are in contact using a modified Ghost Fluid Method. Use of a sharp interface treatment obviates the need to develop special treatments for materials that coexist within a grid cell. Such subgrid material pairs are always maintained as distinct entities separated by sharp interfaces. The results obtained from our numerical simulations match well with experimental data where available and with other numerical simulations. Using the contact model, it is demonstrated that the wave physics involved in flyer plate impact cases have been captured accurately for material pairs of various impedances. The contact algorithm is shown to handle contact with rigid solids in the case of a Taylor bar impact. Finally, oblique impact of a projectile on a target at an $10^{\circ}$ angle of impact has been studied using the present contact algorithm

and its capability for handling sliding and separation has been shown. The study of ricochet of a projectile obliquely impact a target plate is the subject of ongoing work along with the extension of the algorithm in a three-dimensional parallel computing framework.

.

Table 6-1: Material, dimensions and impact velocity of the flyer and target plates[126].

| Plate | Material | Diameter (mm) | Thickness (mm) | Impact Velocity (m/s) |
|---|---|---|---|---|
| Flyer plate | Aluminum | 120 | $t_1 = 2$ | 450 |
| Target plate | Copper | 120 | $t_2 = 15$ | - |

Table 6-2: Comparison of deformed bar radius and maximum equivalent plastic strain at time 10 μs and 50 μs.

| Time | | Current Simulation | Batra and Stevens[110] |
|---|---|---|---|
| $t = 10\ \mu s$ | Taylor Bar Deformed Radius (mm) | 6.2 | 6.1 |
| | Maximum Equivalent Plastic Strain | 0.50 | 0.49 |
| $t = 50\ \mu s$ | Taylor Bar Deformed Radius (mm) | 8.3 | 8.1 |
| | Maximum Equivalent Plastic Strain | 2.27 | 2.20 |

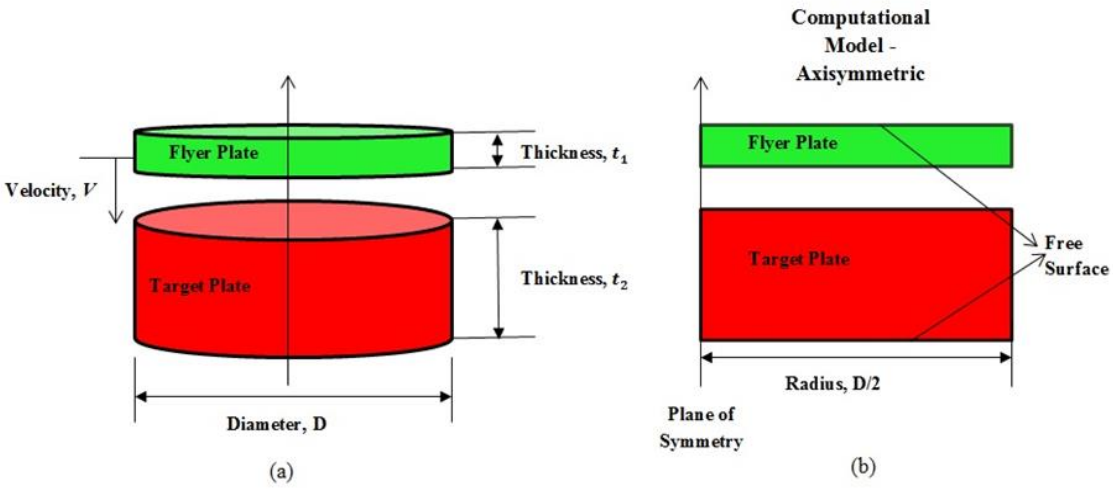


Figure 6-1: (a) Geometrical sketch of the plate impact experiment, (b) Computational geometry over which simulation is performed.

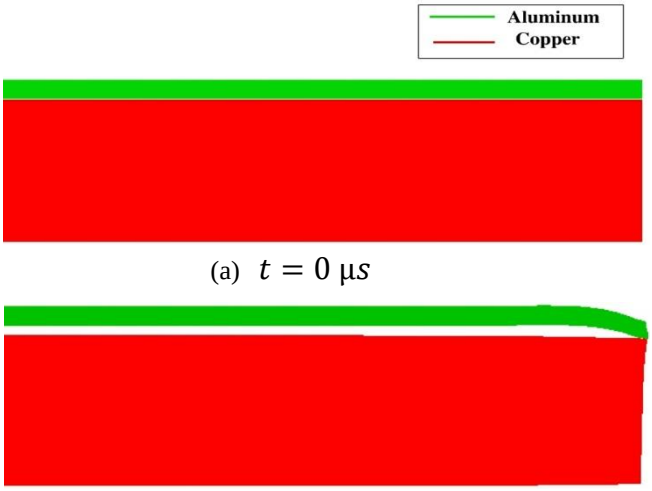


(a) $t = 0\ \mu s$

(b) $t = 7\ \mu s$

Figure 6-2: Separation of flyer and target plates after the impact due to the development of tensile stress state at the impacted interface.

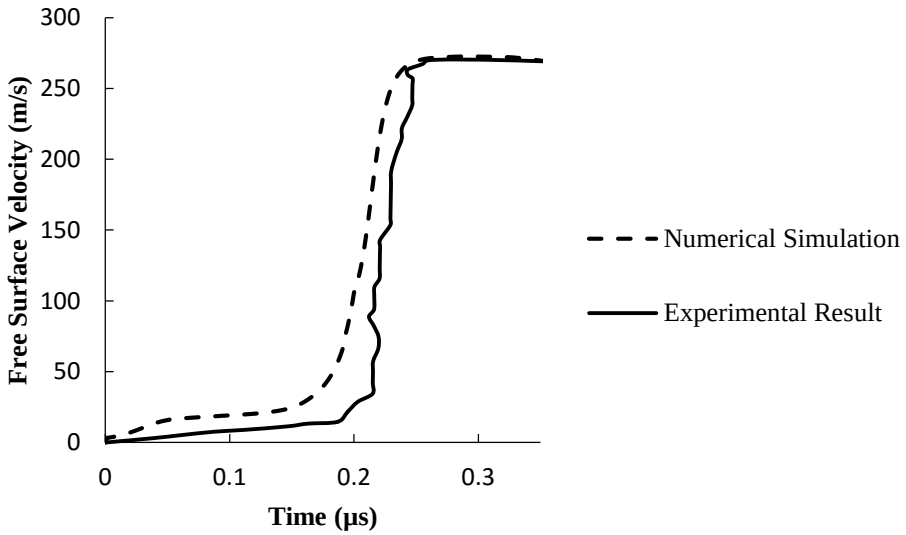


Figure 6-3: Free surface velocity plots of the target plate vs. time from numerical simulation and experimental results[126].

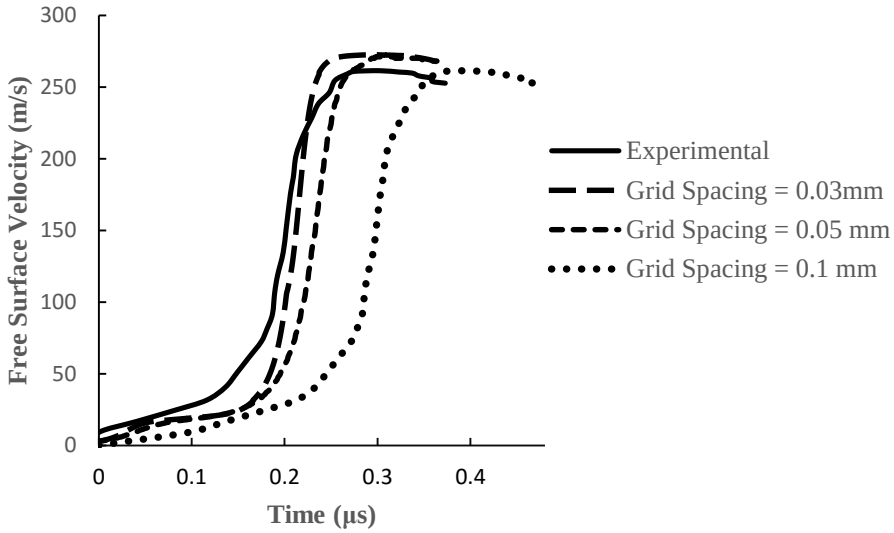


Figure 6-4: Free surface velocity plots of the target plate vs. time from numerical simulation for three different grid sizes of 0.1 $mm$, 0.05 $mm$ and 0.03 $mm$ along with the experimental results.

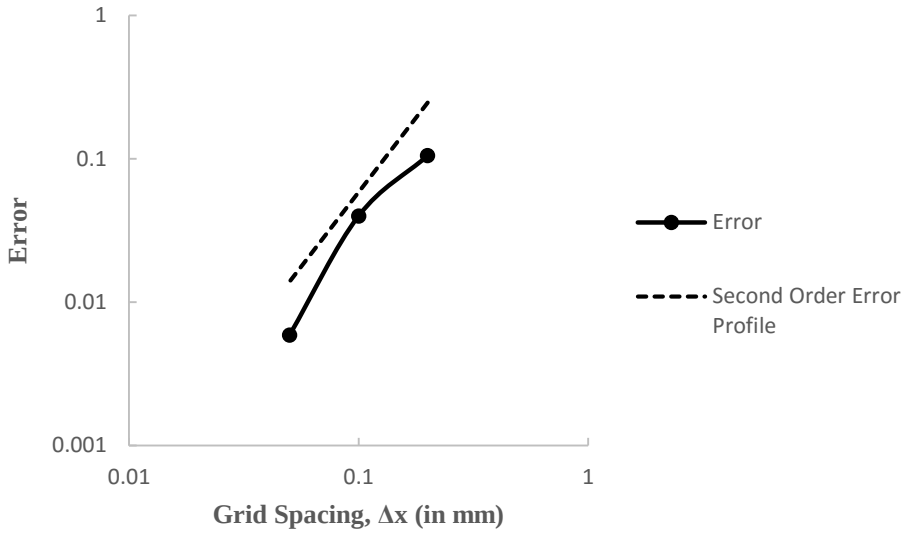


Figure 6-5: Error measure plot of the peak bottom surface velocity of the target plate with four different grid sizes of 0.2 $mm$, 0.1 $mm$, 0.05 $mm$ and 0.03 $mm$ with the second order error estimate plot.

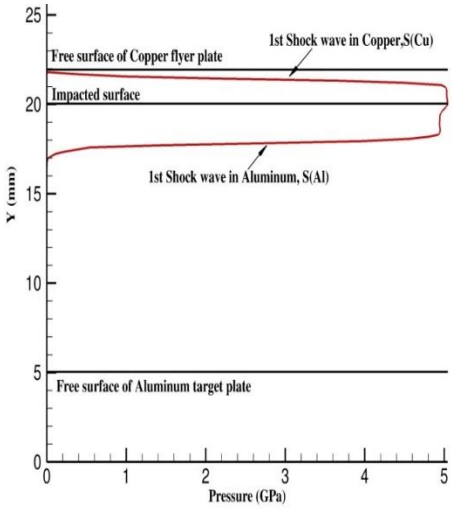


(a) Impact between Copper flyer plate and Aluminum target plate produces shock wave S(Cu) and S(Al) at $t =$

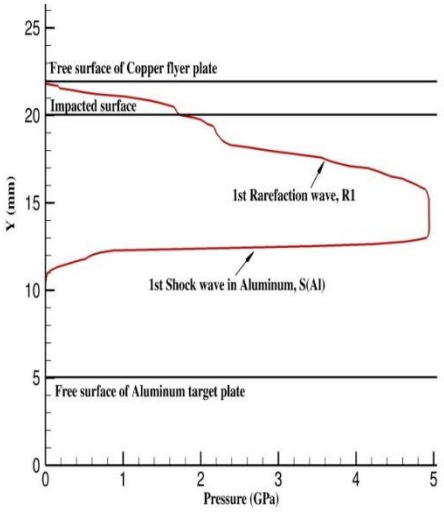


(b) Shock wave S(Cu) after reflection from its top free surface interacts at the impacted surface and produces the first rarefaction R1 in the Aluminum plate at $t = 1.5\ \mu s$

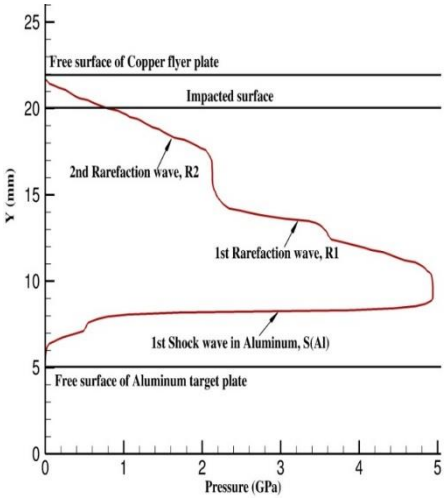


(c) The impacted surface maintains a compressive stress state which leads to the successive generation of second rarefaction wave R2 inside the

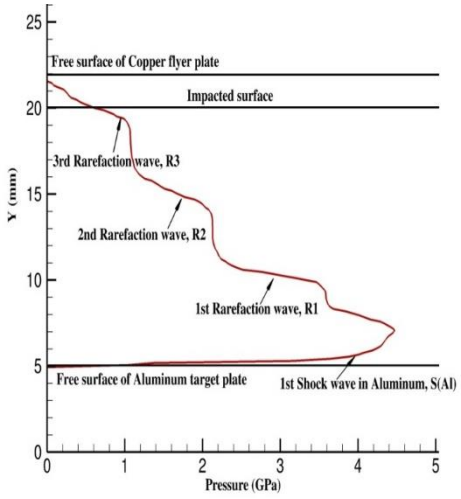


(d) The interaction of the wave in the Copper flyer plate with its free surface and the impacted surface produces successive rarefaction wave R3 which unloads the

Figure 6-6: Wave interaction inside the target plate when impacted by a hard impactor plate at a speed of $450\ m/s$, shows gradual decrease in the magnitude of pressure wave while travelling inside the target plate after the impact which leads to unloading of the target plate.

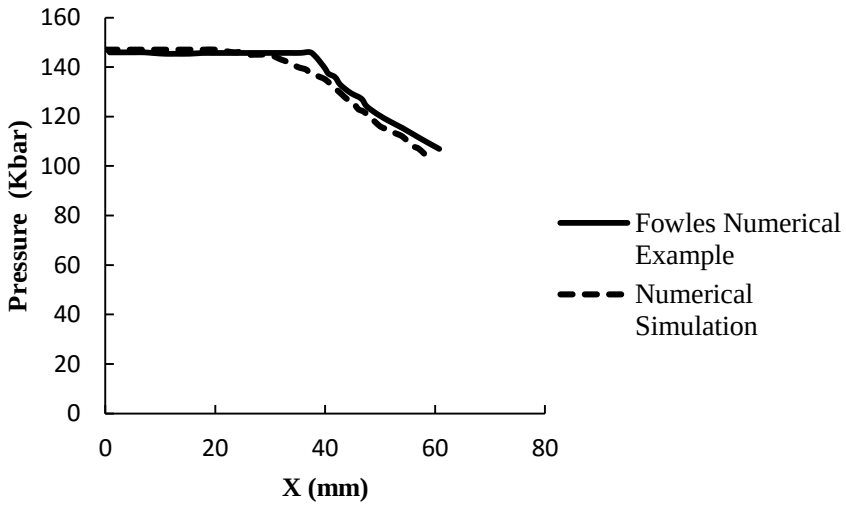


Figure 6-7: Variation of peak pressure at the shock front as a function of the distance travelled by the shock wave in the target plate.

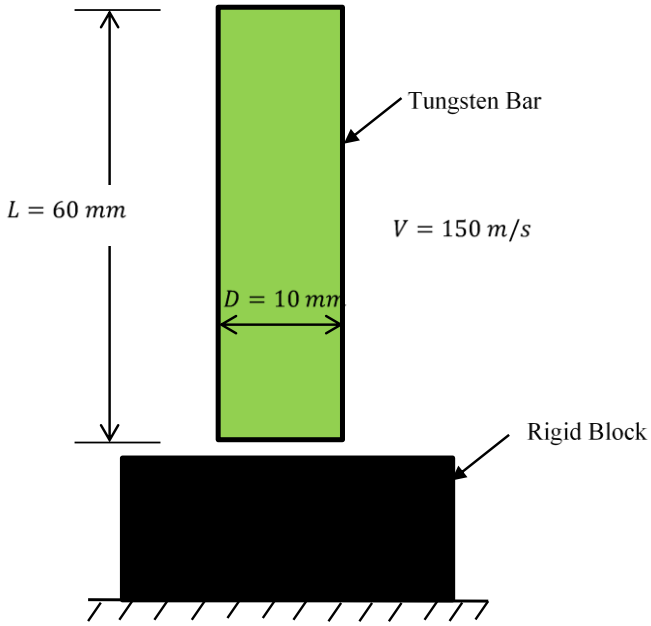


Figure 6-8: Initial configuration for the simulation of Taylor bar impact problem on a rigid block with a speed of $150\ m/s$.

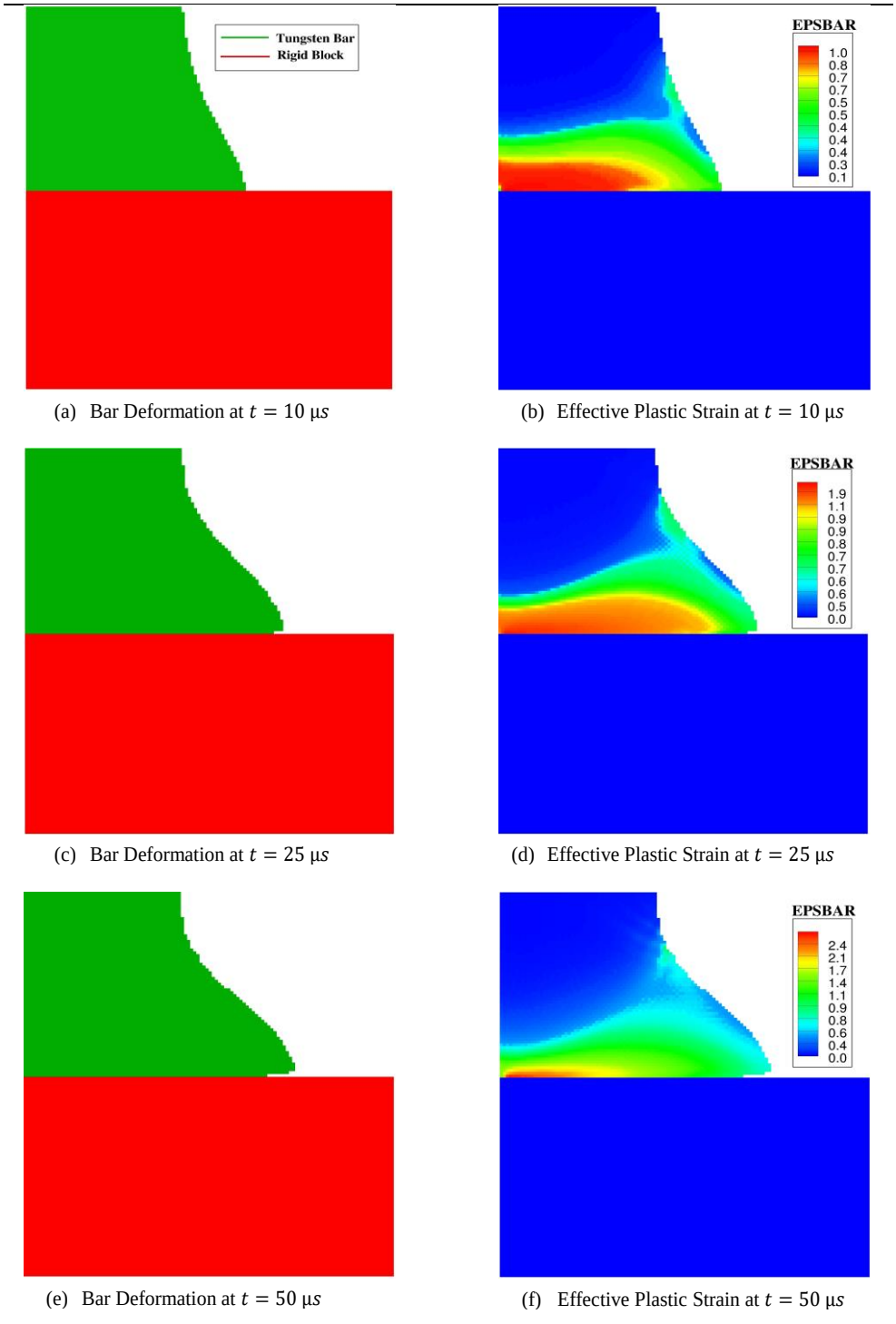


(a) Bar Deformation at $t = 10\ \mu s$

(b) Effective Plastic Strain at $t = 10\ \mu s$

(c) Bar Deformation at $t = 25\ \mu s$

(d) Effective Plastic Strain at $t = 25\ \mu s$

(e) Bar Deformation at $t = 50\ \mu s$

(f) Effective Plastic Strain at $t = 50\ \mu s$

Figure 6-9: Taylor bar deformation profile and effective plastic strain at different time intervals for the axisymmetric impact of Tungsten bar on a rigid block at a speed of $150\ m/s$.

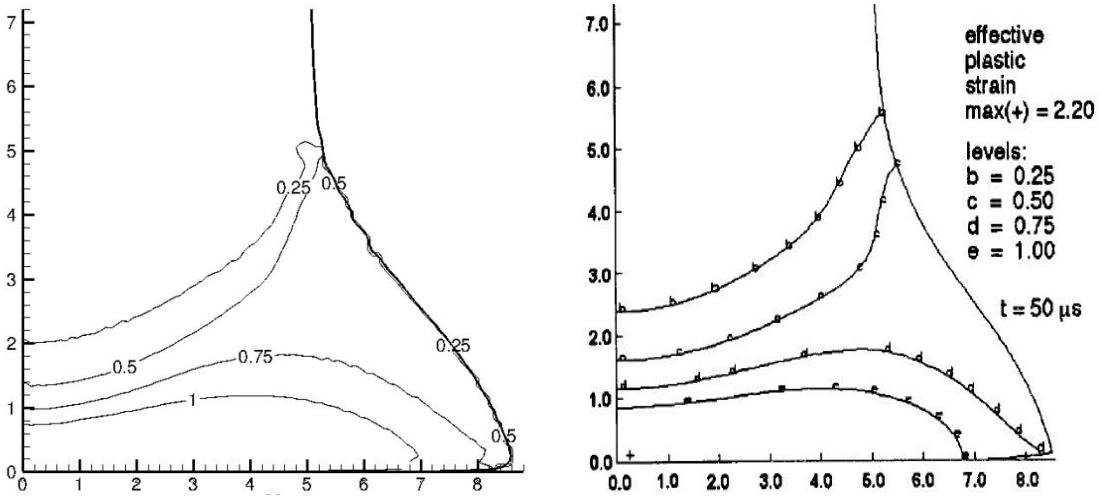


(a) Current Simulation

(b) Batra and Stevens[110]

Figure 6-10: Comparison plot of contours of effective plastic strain at $t = 50\ \mu s$ with the work of Batra and Stevens.

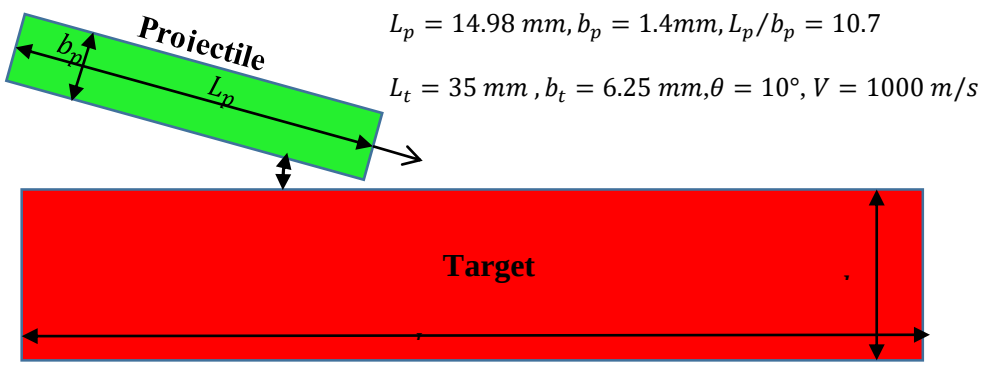


Figure 6-11: Configuration for the simulation of oblique impact of projectile over the target at 10° angle of attack.

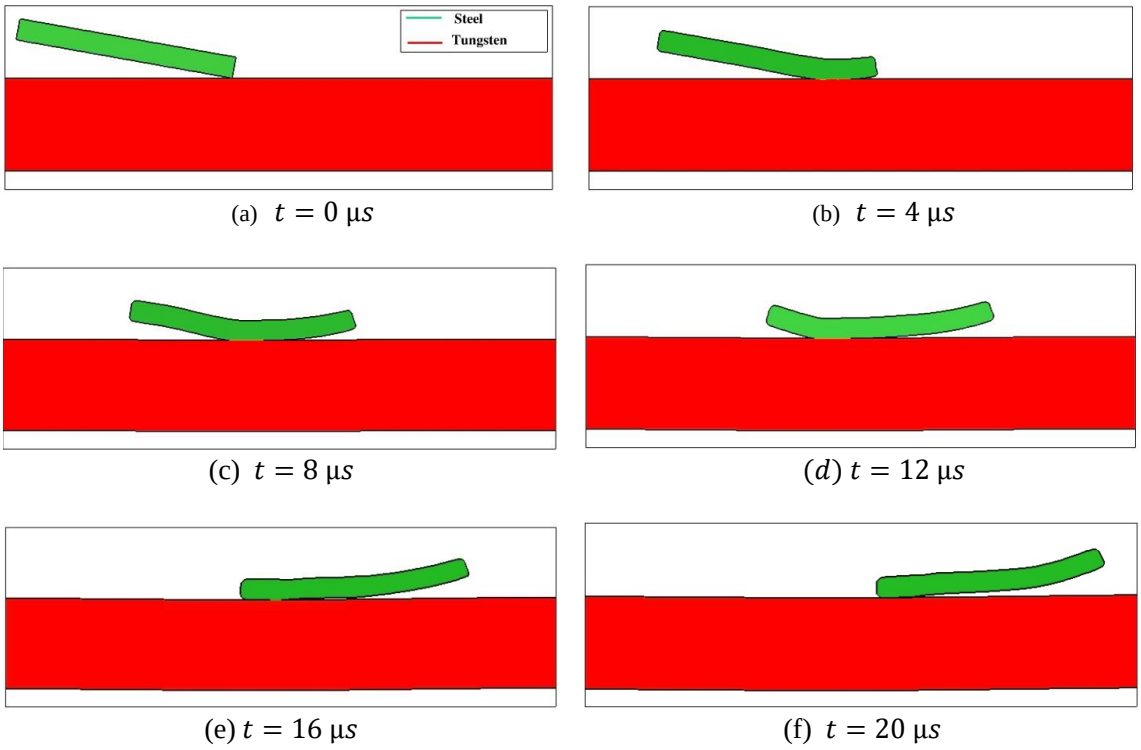


(a) $t = 0\ \mu s$ (b) $t = 4\ \mu s$

(c) $t = 8\ \mu s$ $(d)\ t = 12\ \mu s$

(e) $t = 16\ \mu s$ (f) $t = 20\ \mu s$

Figure 6-12: Ricochet of high strength steel projectile over a tungsten target at 10° angle of attack with a speed of 1000 m/s.

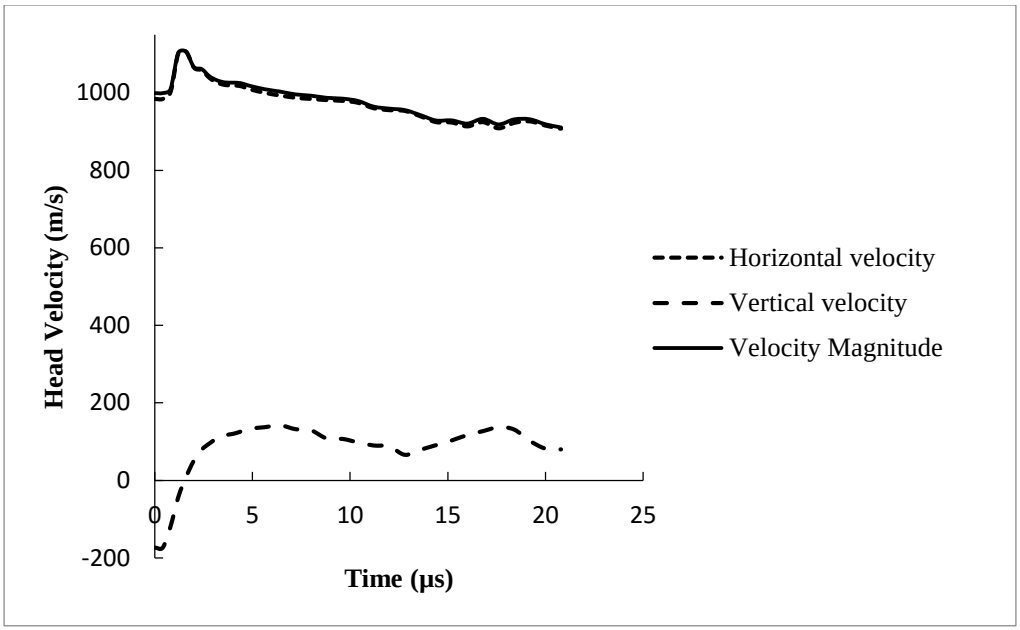


Figure 6-13: Variation of steel projectile head velocity with time of high strength steel projectile.

CHAPTER 7

# FLYER PLATE LOAD ANALYSIS ON PRESSED ENERGETIC MATERIALS

## 7.1.Introduction

In chapter 4, shock analysis on two different samples of HMX based pressed energetic material (Class III and Class V) is performed. The previous analysis was aimed towards understanding the effects of microstructure on initiation behavior of pressed explosives. For the Class III and Class V samples, experimental results are available from the work of Welle et. al.[5] and the results are shown with James threshold initiation curve. The current work is aimed to compare the numerical results obtained from the shock analysis of pressed energetic samples using current framework with the experimental results of Welle et. al.[5]. For direct numerical comparison with the experiments, it is important that computational modeling should reflect the experimental set up. The experiments performed using Welle et. al.[5] uses flyer plate experiments to apply shock load on the explosive material. Hence, computation model for shock analysis should include flyer plate impact experiments on the pressed explosives.

The frictionless contact and separation algorithm developed in chapter 6 is used to model the flyer plate experiments for pressed energetic samples.

## 7.2.Flyer plate simulation for Class III sample

Shock analysis using flyer plate impact is performed for Class III pressed explosives. The microstructure of the Class III sample is represented using level set method as discussed in chapter 4. Image processing algorithm are employed on the SEM image of Class III sample. The methods to obtain the level set geometry of microstructure is same as it was discussed in chapter 4. The Class III sample is the target material in the current simulation which is impacted using a flyer plate made of kapton material. The material

properties for kapton is obtained from the work of Tarver et. al.[131]. The flyer speed for the current simulation is $3\ km/s$. The dimension of the Class III sample used in the previous analysis was $25\ \mu m \times 16 \mu m$. The dimension of the target plate is selected to be more than the Class III sample original dimension in order to avoid boundary effects arises due to free surface. The dimension for Class III target plate are $25\ \mu m \times 20 \mu m$ and flyer plate dimensions is $8\ \mu m \times 20 \mu m$. The current analysis includes reactive capability for HMX using the Henson Smilowitz model[77].

Figure 7-1 shows the temperature contour obtained from the flyer plate simulation of class III sample. It can be seen kapton flyer impacts the Class III sample and it leads to shock wave propagation in the target (Class III) material. As shock wave propagates in the explosive sample, its interaction with the voids leads to collapse and formation of hot spots. The hot spot temperature is sufficient to initiate chemical reaction at different location as shown in Figure 7-1. For $3\ km/s$ flyer speed, Class III sample leads to initiation and growth of chemical reaction.

### 7.3.Flyer plate simulation for Class V sample

Flyer plate load analysis is performed on Class V sample. The flyer plate is made of kapton material. The microstructural geometry of Class V sample is represented using level set field. The level set field is obtained using the image processing algorithm applied on the SEM image of Class V sample. The dimensions of the flyer plate are $8\ \mu m\ \times 20 \mu m$. The target plate dimensions are $25\ \mu m\ \times 20\ \mu m$. The flyer speed is $3\ km/s$.

The temperature contour obtained from the flyer plate analysis on Class V sample is shown in Figure 7-2. It can be seen that, flyer plate impact on the target material loads the target material. The shock wave propagation in the Class V sample, leads to collapse of voids present in the microstructure and eventually formation of hot spots. The hot spots thus formed are not able to initiate chemical reactions in the material.

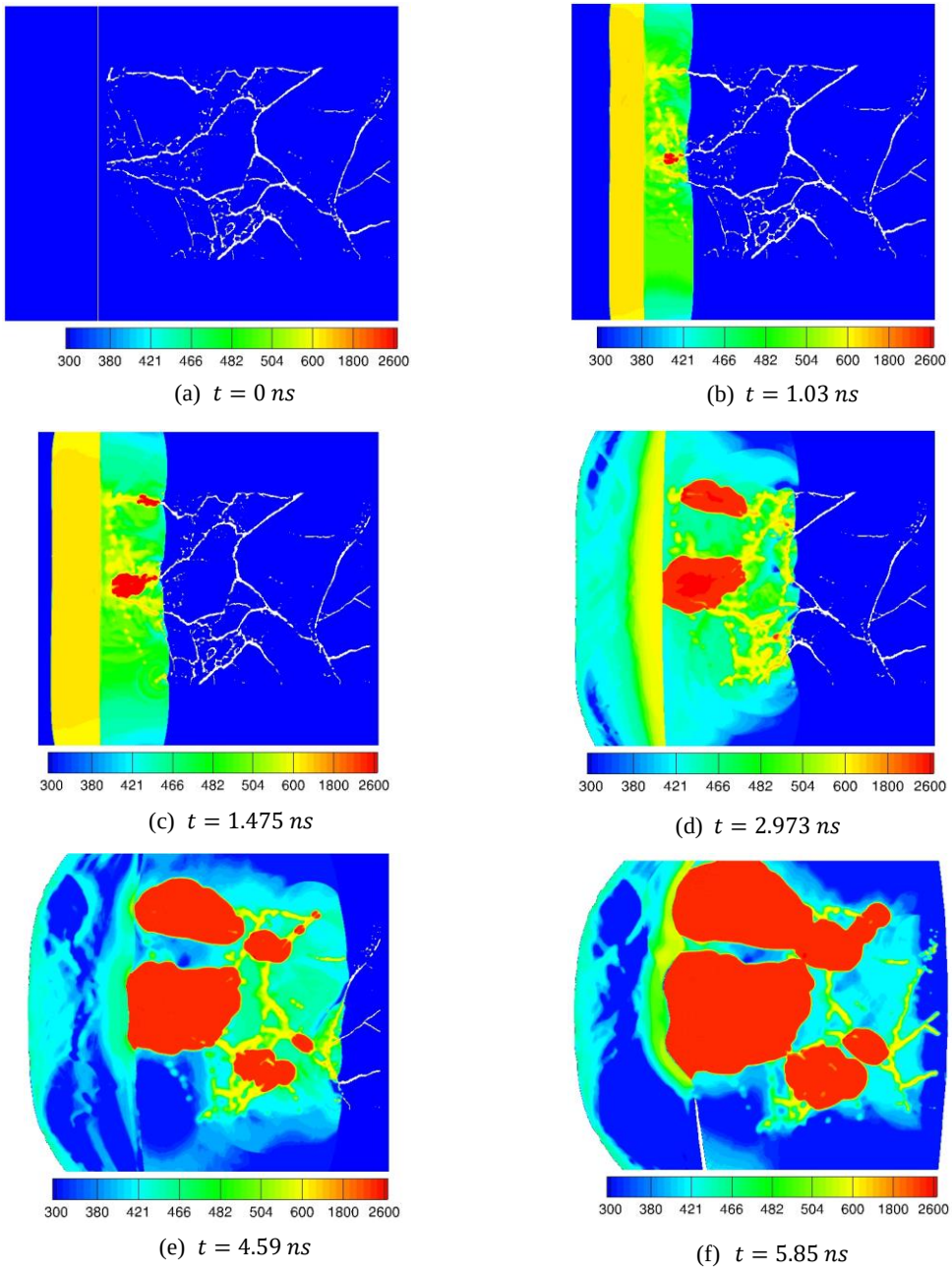


(a) $t = 0\ ns$ (b) $t = 1.03\ ns$

(c) $t = 1.475\ ns$ (d) $t = 2.973\ ns$

(e) $t = 4.59\ ns$ (f) $t = 5.85\ ns$

Figure 7-1: Temperature (K) contours obtained from flyer plate load analysis of Class III pressed energetic sample. The flyer speed is 3 $km/s$. Class III sample leads to initiation of chemical reaction in the material.

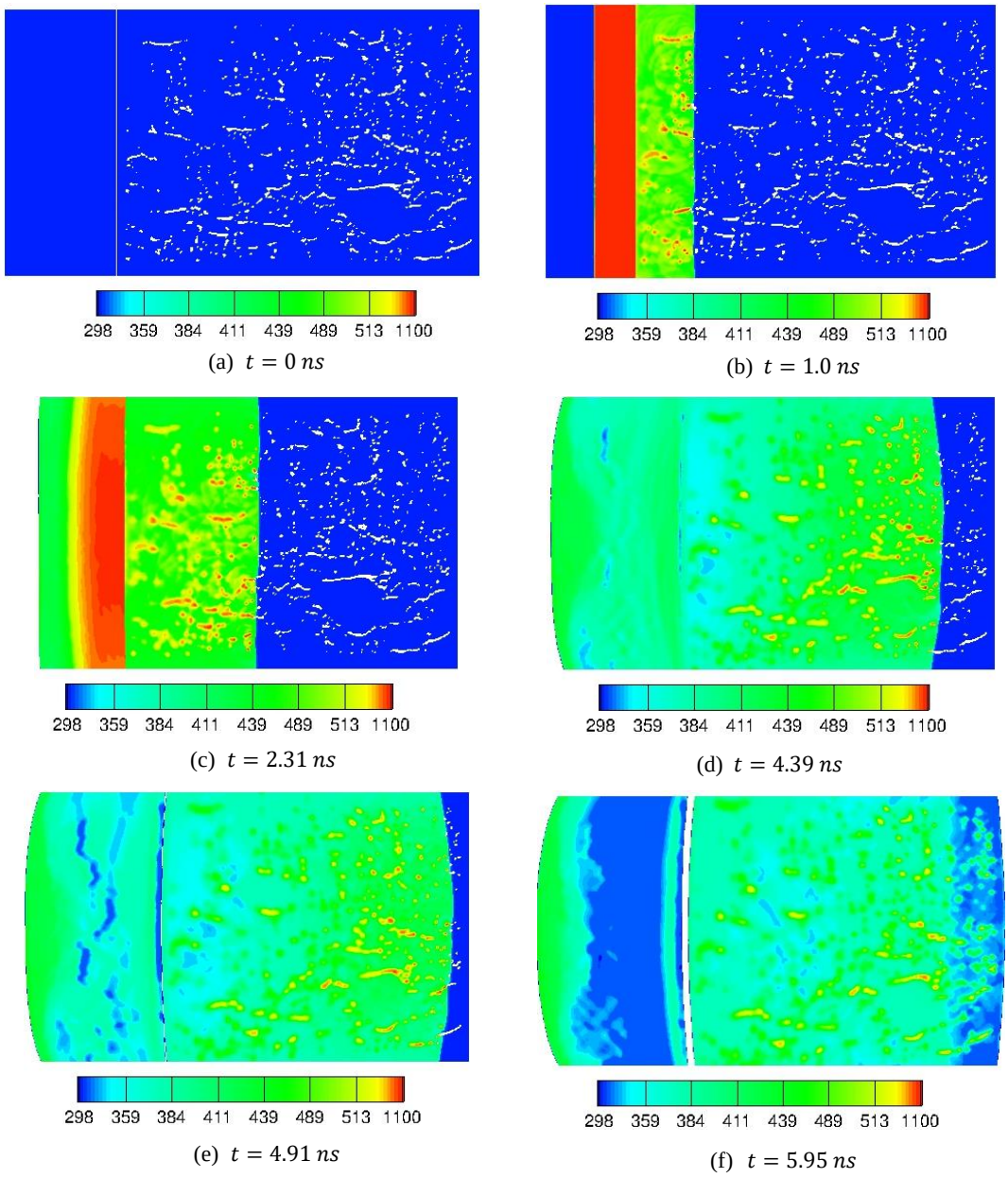


Figure 7-2: Temperature (K) contours obtained from flyer plate load analysis of Class V pressed energetic sample. The flyer speed is 3 $km/s$.

# CHAPTER 8

# CONCLUSIONS AND FUTURE WORK

## 8.1. Contribution of the thesis

A numerical framework for mesoscale computation on heterogeneous energetic materials like plastic bonded explosives (PBX), pressed explosives etc. has been developed. The numerical framework is based on Eulerian Cartesian grid-based massively three dimensional solver combined with a level set based image processing machinery to characterize the real microstructure of the explosives. In past, the numerical framework has been shown to be efficient in capturing shock propagation and handling large deformation, collapse and fragmentation arising in multimaterial impact situation. This work advances the numerical framework used in the past work to develop a numerical framework for performing mesoscale simulations on heterogeneous energetic materials by addressing the following challenges:

1. This work identifies various reasons that can lead to the initiation of chemical reactions and ignition in heterogeneous energetic materials in the high shock load regime. The reasons considered in this work are void collapse, shock heating of the HMX crystals and plastic deformation of HMX. The importance of each of these factors on shock initiation in energetic materials are discussed in detail by performing reactive mesoscale simulations.
2. The development of a general image processing framework to characterize the real geometry of the explosive material and generating level set fields consistent with the flow solver to describe the microstructural details of the explosive geometry is one of the challenging tasks of this work. The image processing framework is applied on various samples of explosives and is tested on various types of image formats. The image to computation approach for mesoscale simulation on explosives allows for accurate prediction of hot spot location and its strength. This framework is developed independently so that it can be merged with any flow solver which utilizes level set to describe the

geometries. One of the potential application areas is handling of medical images to perform computations on them directly.

3. The seven step chemical kinetic law for HMX decomposition given by Henson-Smilowitz is incorporated in mesoscale computation of HMX based explosives for the shock initiation and ignition study. The chemical kinetic equations are solved using $5^{th}$ order Runge Kutta Fehlberg method and the chemical species are advected with the flow using Strang splitting approach. The chemical reaction model is parallelized in the current framework using MPI libraries. The chemical kinetic law with the current numerical framework is able to predict the ignition sites in the domain based on the local hot spot conditions.

4. An algorithm for the treatment of contact and separation of material interfaces is being developed in the current work. The advantage of the model lies in its ease of implementation; in contrast to Lagrangian contact treatments, search operations for detecting collisions are simplified by the use of level sets and no local constraint conditions to prevent interpenetration through penalty-type force application is necessary to separate interfaces. Because the framework is Eulerian difficulties associated with carrying meshes through the material interactions, managing meshes to retain solution accuracy and stability and detecting contact between interacting surfaces are circumvented. The contact conditions are handled by implicitly satisfying the interfacial conditions on the parts of the interacting material interfaces that are in contact using a modified Ghost Fluid Method. Use of a sharp interface treatment obviates the need to develop special treatments for materials that coexist within a grid cell. Such subgrid material pairs are always maintained as distinct entities separated by sharp interfaces. The results obtained from numerical simulations form various multimaterial impact problems considered matches well with experimental data and with other numerical simulations. In shock initiation study of energetic materials, it has been seen that the intergranular friction between the HMX crystals due to impact can lead to the formation of hot spots which in turn can lead to

ignition. Hence, the modeling of such events for energetic materials can be handled using this contact model with addition of frictional law.

5. Void collapse is considered as a predominant reason for shock initiation and ignition in heterogeneous energetic materials. This work characterizes shock initiation and ignition criterion in HMX due to void collapse using the Henson-Smilowitz chemical decomposition law. Various factors such as shock strength and void volume fraction in the heterogeneous HMX has been identified that can significantly affect shock initiation and ignition behavior of the explosive. Also, this study is able to develop an internal energy based ignition threshold criterion for HMX which depends on shock speed and void positioning.

6. The framework developed is also used to study the shock initiation behavior of plastic bonded explosive and two categories of pressed explosives i.e. Class III and Class IV. The shock analysis is performed on the real microstructures by performing image processing algorithms on the microstructural images obtained from Chris Molek and Eric Welle from EGLIN AFB, Florida. The current framework is able to predict the imitation of chemical reaction and ignition in these explosives. Apart from the simulation on the real geometries, in order to understand the behavior of the pressed explosives, numerical experiments on elongated voids are designed. The numerical experiments point out that the orientation of the elongated voids with respect to the incident shock plays an important role in determination of which location in the pressed explosives can be critical to the shock loading.

## 8.1. Future work and extensions

The framework developed in this work can be used to explore many directions. The work here can be extended in following ways:

1. The image processing framework used in the current work is shown to be verified for many geometries in the past work[76]. However, the image framework is capable of

modeling only two phase materials. For example, it was shown that for PBX microstructure, HMX crystals and polymeric binder can be represented accurately using the current approach. This framework cannot be used to characterize materials with more than two phase which is required for PBX type materials where HXM crystals, polymeric binders and voids are present in the microstructure. Hence, the current image processing algorithm needs to be improvised for characterizing materials having more than two phases.

2. The Henson-Smilowitz chemical kinetic law for HMX decomposition used in the current work is the most recent and sophisticated model available in HMX literature. However, it is observed in the current work that this model does not conserving the enthalpy of the reacting system and this gives rise to predicting unrealistically high temperature when ignition takes place. Hence, other existing decomposition laws i.e. Tarver's four equation decomposition law needs to be implemented in the current framework which can leads to physical realistic temperatures after ignition. Also, due to the lack of experimental data on shock initiation and ignition, it would be interesting to compare shock initiation results obtained from various decomposition laws of HMX.

3. It is known that inter-granular friction between HMX crystals can acts as important mechanism in the formation of hot spots and hence it is important to model the interfacial condition arises due to frictional contact. The frictionless contact and separation algorithm developed in current work needs to extended to include frictional model which handle inter-granular frictional contact of HMX crystals.

4. The numerical framework developed has been shown to be validated and verified for various multimaterial contact and impact problems[72, 89] and inert void collapse simulations[58] in past using the available experimental data and other numerical simulations. However, due to the lack of shock initiation experimental data on heterogeneous energetic materials the simulation results from mesoscale computation on

PBX and pressed explosives in the current work has not been validated. Hence, gathering experimental data and validating existing results is one of the works in progress.

# REFERENCES


1. Handley, C.A., *Numerical modelling of two HMX-based plastic-bonded explosives at the mesoscale*. 2011, University of St Andrews.

2. James, H., *An extension to the critical energy criterion used to predict shock initiation thresholds.* Propellants, explosives, pyrotechnics, 1996. **21**(1): p. 8-13.

3. Asay, B., *Shock Wave Science and Technology Reference Library, Vol. 5: Non-Shock Initiation of Explosives*. Vol. 5. 2009: Springer Science & Business Media.

4. Mas, E., et al. *A viscoelastic model for PBX binders*. in *AIP CONFERENCE PROCEEDINGS*. 2002. IOP INSTITUTE OF PHYSICS PUBLISHING LTD.

5. Welle, E., et al. *Microstructural effects on the ignition behavior of HMX*. in *Journal of Physics: Conference Series*. 2014. IOP Publishing.

6. Fickett, W. and W.C. Davis, *Detonation: theory and experiment*. 2012: Courier Corporation.

7. Ramsay, J. and A. Popolato, *Analysis of shock wave and initiation data for solid explosives*. 1965, Los Alamos Scientific Lab., Univ. of California, N. Mex.

8. Gustavsen, R., et al. *Initiation of EDC-37 measured with embedded electromagnetic particle velocity gauges*. in *SHOCK COMPRESSION OF CONDENSED MATTER-1999*. 2000. AIP Publishing.

9. Mulford, R.N. and D.C. Swift, *Mesoscale modelling of shock initiation in HMX-based explosives.* Shock Compression of Condensed Matter, 2001: p. 415-418.

10. Baytos, J.F., T.R. Gibbs, and A. Popolato, *LASL explosive property data*. Vol. 4. 1980: Univ of California Press.

11. James, H., *Critical energy criterion for the shock initiation of explosives by projectile impact.* Propellants, Explosives, Pyrotechnics, 1988. **13**(2): p. 35-41.

12. James, H., P. Haskins, and M. Cook, *Prompt shock initiation of cased explosives by projectile impact.* Propellants, explosives, pyrotechnics, 1996. **21**(5): p. 251-257.

13. Chen, P., et al., *Deformation and failure of polymer bonded explosives under diametric compression test.* Polymer testing, 2006. **25**(3): p. 333-341.

14. Siviour, C.R., et al. *High strain rate properties of a polymer-bonded sugar: their dependence on applied and internal constraints*. in *Proceedings of the Royal Society of London A: Mathematical, Physical and Engineering Sciences*. 2008. The Royal Society.

15. Wiegand, D.A. and B. Reddingius, *Mechanical properties of confined explosives.* Journal of Energetic Materials, 2005. **23**(2): p. 75-98.

16. Gray III, G., et al. *Influence of temperature on the high-strain-rate mechanical behavior of PBX 9501*. in *The tenth American Physical Society topical conference on shock compression of condensed matter*. 1998. AIP Publishing.

17. Palmer, S. and J. Field. *The Deformation and Fracture of $\ beta $-HMX*. in *Proceedings of the Royal Society of London A: Mathematical, Physical and Engineering Sciences*. 1982. The Royal Society.

18. Skidmore, C., et al., *Characterization of HMX particles in PBX 9501*. 1998.

19. Liu, G. and H. Yu, *Stereological characterization of particle contiguity.* Journal of Microscopy, 1996. **181**(1): p. 82-87.

20. Lee, E.L. and C.M. Tarver, *Phenomenological model of shock initiation in heterogeneous explosives.* Physics of Fluids (1958-1988), 1980. **23**(12): p. 2362-2372.

21. Baer, M. and J. Nunziato, *A two-phase mixture theory for the deflagration-to-detonation transition (DDT) in reactive granular materials.* International journal of multiphase flow, 1986. **12**(6): p. 861-889.

22. Bowman, A.L., et al., *Numerical modeling of shock-sensitivity experiments*. 1981, Los Alamos Scientific Lab., NM (USA).

23. Johnson, J., P. Tang, and C. Forest, *Shock-wave initiation of heterogeneous reactive solids.* Journal of Applied Physics, 1985. **57**(9): p. 4323-4334.

24. Menikoff, R., *Granular explosives and initiation sensitivity*. http://lib-www. lanl. gov/la-pubs/00796456. pdf, 1999: p. 2.

25. Campbell, A., et al., *Shock initiation of solid explosives.* Physics of Fluids (1958-1988), 1961. **4**(4): p. 511-521.

26. Khasainov, B., et al. *Two-phase visco-plastic model of shock initiation of detonation in high density pressed explosives*. in *7th symposium (international) on detonation, Annapolis, MD*. 1981.

27. Field, J.E., *Hot spot ignition mechanisms for explosives.* Accounts of chemical Research, 1992. **25**(11): p. 489-496.

28. Bowden, F., et al. *The detonation of liquid explosives by gentle impact. The effect of minute gas spaces*. in *Proceedings of the Royal Society of London A: Mathematical, Physical and Engineering Sciences*. 1947. The Royal Society.

29. Bowden, F.P. and A.D. Yoffe, *Initiation and growth of explosion in liquids and solids*. 1952: CUP Archive.

30. Bowden, F.P. and A.D. Yoffe, *Fast reactions in solids*. 1958: Academic Press.

31. Coley, G. and J. Field. *The role of cavities in the initiation and growth of explosion in liquids*. in *Proceedings of the Royal Society of London A: Mathematical, Physical and Engineering Sciences*. 1973. The Royal Society.

32. Chaudhri, M. and J. Field. *The role of rapidly compressed gas pockets in the initiation of condensed explosives*. in *Proceedings of the Royal Society of London A: Mathematical, Physical and Engineering Sciences*. 1974. The Royal Society.

33. Mader, C.L., *Initiation of detonation by the interaction of shocks with density discontinuities.* Physics of Fluids (1958-1988), 1965. **8**(10): p. 1811-1816.

34. Mader, C.L., *Numerical modeling of explosives and propellants*. 2007: CRC press.

35. Frey, R.B., *Cavity Collapse in Energetic Materials*. 1986, DTIC Document.

36. Bowden, F. and O. Gurton. *Initiation of solid explosives by impact and friction: the influence of grit*. in *Proceedings of the Royal Society of London A: Mathematical, Physical and Engineering Sciences*. 1949. The Royal Society.

37. Bowden, F. and O. Gurton. *Birth and growth of explosion in liquids and solids initiated by impact and friction*. in *Proceedings of the Royal Society of London A: Mathematical, Physical and Engineering Sciences*. 1949. The Royal Society.

38. Chaudhri, M., *Stab initiation of explosions.* 1976.

39. Afanas′ev, G.T. and V.K. Bobolev, *Initiation of solid explosives by impact*. 1971: Israel Program for Scientific Translations;[available from the US Dept. of Commerce, National Technical Information Service, Springfield, Va.].

40. Heavens, S. and J. Field. *The ignition of a thin layer of explosive by impact*. in *Proceedings of the Royal Society of London A: Mathematical, Physical and Engineering Sciences*. 1974. The Royal Society.

41. Winter, R. and J. Field. *The role of localized plastic flow in the impact initiation of explosives*. in *Proceedings of the Royal Society of London A: Mathematical, Physical and Engineering Sciences*. 1975. The Royal Society.

42. Field, J., G. Swallowe, and S. Heavens. *Ignition mechanisms of explosives during mechanical deformation*. in *Proceedings of the Royal Society of London A: Mathematical, Physical and Engineering Sciences*. 1982. The Royal Society.

43. Frey, R.B., *The initiation of explosive charges by rapid shear*. 1980, DTIC Document.

44. Bourne, N. and A. Milne. *The temperature of a shock-collapsed cavity*. in *Proceedings of the Royal Society of London A: Mathematical, Physical and Engineering Sciences*. 2003. The Royal Society.

45. Menikoff, R. *Pore collapse and hot spots in HMX*. in *AIP Conference Proceedings*. 2004. IOP INSTITUTE OF PHYSICS PUBLISHING LTD.

46. Barton, N.R., N.W. Winter, and J.E. Reaugh, *Defect evolution and pore collapse in crystalline energetic materials.* Modelling and Simulation in Materials Science and Engineering, 2009. **17**(3): p. 035003.

47. Menikoff, R. and E. Kober. *Compaction waves in granular HMX*. in *SHOCK COMPRESSION OF CONDENSED MATTER-1999*. 2000. AIP Publishing.

48. Mas, E., B. Clements, and D. George. *Direct numerical simulations of PBX 9501*. in *SHOCK COMPRESSION OF CONDENSED MATTER-2003: Proceedings of the Conference of the American Physical Society Topical Group on Shock Compression of Condensed Matter*. 2004. AIP Publishing.

49. Clements, B. and E. Mas. *Modeling high explosives with the method of cells and Mori-Tanaka effective medium theories*. in *AIP CONFERENCE PROCEEDINGS*. 2002. IOP INSTITUTE OF PHYSICS PUBLISHING LTD.

50. Baer, M., M. Kipp, and F.v. Swol, *Micromechanical modeling of heterogeneous energetic materials*. 1998, Sandia National Labs., Albuquerque, NM (United States).

51. Baer, M.R., *Mesoscale modeling of shocks in heterogeneous reactive materials*, in *ShockWave Science and Technology Reference Library*. 2007, Springer. p. 321-356.

52. Baer, M., *Modeling heterogeneous energetic materials at the mesoscale.* Thermochimica acta, 2002. **384**(1): p. 351-367.

53. Conley, P., D. Benson, and P.M. Howe. *Microstructural effects in shock initiation*. in *this symposium*. 1998.

54. Benson, D.J. and P. Conley, *Eulerian finite-element simulations of experimentally acquired HMX microstructures.* Modelling and Simulation in Materials Science and Engineering, 1999. **7**(3): p. 333.

55. Barua, A. and M. Zhou, *A Lagrangian framework for analyzing microstructural level response of polymer-bonded explosives.* Modelling and Simulation in Materials Science and Engineering, 2011. **19**(5): p. 055001.

56. Tran, L. and H. Udaykumar, *Simulation of Void Collapse in an Energetic Material, Part I: Inert Case.* Journal of propulsion and power, 2006. **22**(5): p. 947-958.

57. Tran, L. and H. Udaykumar, *Simulation of void collapse in an energetic material, Part 2: reactive case.* Journal of propulsion and power, 2006. **22**(5): p. 959-974.

58. Kapahi, A. and H. Udaykumar, *Dynamics of void collapse in shocked energetic materials: physics of void–void interactions.* Shock Waves, 2013. **23**(6): p. 537-558.

59. Kapahi, A. and H. Udaykumar, *Three-dimensional simulations of dynamics of void collapse in energetic materials.* Shock Waves, 2015. **25**(2): p. 177-187.

60. Levesque, G.A. and P. Vitello, *The Effect of Pore Morphology on Hot Spot Temperature.* Propellants, Explosives, Pyrotechnics, 2014.

61. Zhang, J. and T.L. Jackson. *Detonation Initiation with Thermal Deposition due to Pore Collapse in Energetic Materials-Towards the Coupling between Micro-and Macro-scale*. in *51st AIAA/SAE/ASEE Joint Propulsion Conference*. 2015.

62. Kapila, A., et al., *A numerical study of the dynamics of detonation initiated by cavity collapse.* Shock Waves, 2015: p. 1-28.

63. Barua, A., Y. Horie, and M. Zhou, *Energy localization in HMX-Estane polymer-bonded explosives during impact loading.* Journal of Applied Physics, 2012. **111**(5): p. 054902.

64. Panchadhar, R. and K.A. Gonthier. *MESO-SCALE HEATING PREDICTIONS FOR WEAK IMPACT OF GRANULAR ENERGETIC SOLIDS*. in *SHOCK COMPRESSION OF CONDENSED MATTER 2009: Proceedings of the American Physical Society Topical Group on Shock Compression of Condensed Matter*. 2009. AIP Publishing.

65. Bardenhagen, S., et al. *Direct numerical simulation of weak shocks in granular material*. in *Twelfth International Detonation Symposium, volume ONR*. 2002.

66. Baer, M. and W. Trott. *Theoretical and experimental mesoscale studies of impact-loaded granular explosive and simulant materials*. in *Twelfth International Detonation Symposium, volume ONR*. 2002.

67. Menikoff, R. *Compaction wave profiles in granular HMX*. in *AIP CONFERENCE PROCEEDINGS*. 2002. IOP INSTITUTE OF PHYSICS PUBLISHING LTD.

68. Wang, Y. and G. Weng, *The influence of inclusion shape on the overall viscoelastic behavior of composites.* Journal of Applied Mechanics, 1992. **59**(3): p. 510-518.

69. Li, J. and G. Weng, *Void growth and stress-strain relations of a class of viscoelastic porous materials.* Mechanics of materials, 1996. **22**(3): p. 179-188.

70. McGuire, R. and C. Tarver, *Chemical-decomposition models for the thermal explosion of confined HMX, TATB, RDX, and TNT explosives*. 1981, Lawrence Livermore National Lab., CA (USA).

71. Tarver, C.M., S.K. Chidester, and A.L. Nichols, *Critical conditions for impact-and shock-induced hot spots in solid explosives.* The Journal of Physical Chemistry, 1996. **100**(14): p. 5794-5799.

72. Sambasivan, S., A. Kapahi, and H. Udaykumar, *Simulation of high speed impact, penetration and fragmentation problems on locally refined Cartesian grids.* Journal of Computational Physics, 2012.

73. Kapahi, A., et al., *Three dimensional compressible multi-material flow computations using a parallelized levelset-based solver.* Plasticity of Crystalline Materials: From Dislocations to Continuum, John Wiley & Sons, 2011.

74. Rai, N., A. Kapahi, and H. Udaykumar, *Treatment of contact separation in Eulerian high-speed multimaterial dynamic simulations.* International Journal for Numerical Methods in Engineering, 2014. **100**(11): p. 793-813.

75. Kapahi, A., S. Sambasivan, and H. Udaykumar, *Simulation of collapse and fragmentation phenomena in a sharp interface Eulerian setting.* Computers & Fluids, 2012.

76. Dillard, S.I., et al., *From medical images to flow computations without user-generated meshes.* International journal for numerical methods in biomedical engineering, 2014. **30**(10): p. 1057-1083.

77. Henson, B., et al. *Modeling thermal ignition and the initial conditions for internal burning in PBX 9501*. in *SHOCK COMPRESSION OF CONDENSED MATTER 2009: Proceedings of the American Physical Society Topical Group on Shock Compression of Condensed Matter*. 2009. AIP Publishing.

78. Fehlberg, E., *Classical fifth-, sixth-, seventh-, and eighth-order Runge-Kutta formulas with stepsize control.* 1968.

79. Sethian, J.A., *Level set methods and fast marching methods.* Journal of Computing and Information Technology, 2003. **11**(1): p. 1-2.

80. Fedkiw, R.P., et al., *A non-oscillatory Eulerian approach to interfaces in multimaterial flows (the ghost fluid method).* Journal of computational physics, 1999. **152**(2): p. 457-492.

81. Plohr, B.J. and D.H. Sharp, *A conservative Eulerian formulation of the equations for elastic flow.* Advances in Applied Mathematics, 1988. **9**(4): p. 481-499.

82. Plohr, B.J. and D.H. Sharp, *A conservative formulation for plasticity.* Advances in Applied Mathematics, 1992. **13**(4): p. 462-493.

83. Sambasivan, S.K., *A sharp interface Cartesian grid hydrocode*. 2010: University of Iowa.

84. Simo, J. and T. Hughes, *General return mapping algorithms for rate-independent plasticity*. Constitutive laws for engineering materials: theory and applications, 1987. **1**: p. 221-232.

85. Johnson, G.R. and W.H. Cook, *Fracture characteristics of three metals subjected to various strains, strain rates, temperatures and pressures.* Engineering Fracture Mechanics, 1985. **21**(1): p. 31-48.

86. Conley, P.A., *Eulerian hydrocode analysis of reactive micromechanics in the shock initiation of heterogeneous energetic material*. 1999: University of California, San Diego.

87. Yan-Qing, W. and H. Feng-Lei, *A micromechanical model for predicting combined damage of particles and interface debonding in PBX explosives.* Mechanics of Materials, 2009. **41**(1): p. 27-47.

88. Shu, C.-W. and S. Osher, *Efficient implementation of essentially non-oscillatory shock-capturing schemes, II.* Journal of Computational Physics, 1989. **83**(1): p. 32-78.

89. Kapahi, A., S. Sambasivan, and H. Udaykumar, *A Three-Dimensional Sharp Interface Cartesian Grid Method for Solving High Speed Multi-Material Impact, Penetration and Fragmentation Problems.* Journal of Computational Physics, 2013.

90. Sethian, J.A., *Level set methods and fast marching methods: evolving interfaces in computational geometry, fluid mechanics, computer vision, and materials science*. 1999: Cambridge Univ Pr.

91. Sethian, J., *Evolution, implementation, and application of level set and fast marching methods for advancing fronts.* Journal of Computational Physics, 2001. **169**(2): p. 503-555.

92. Sun, Q., et al., *Speckle reducing anisotropic diffusion for 3D ultrasound images.* Computerized Medical Imaging and Graphics, 2004. **28**(8): p. 461-470.

93. Chan, T.F. and L. Vese, *Active contours without edges.* Image processing, IEEE transactions on, 2001. **10**(2): p. 266-277.

94. Russo, G. and P. Smereka, *A remark on computing distance functions.* Journal of Computational Physics, 2000. **163**(1): p. 51-67.

95. Merriman, T., et al., *'A Non-Oscillatory Eulerian Approach to Interfaces in Multi-Material Flows.* J. Comput. Phys., to appear, 2003.

96. Dalrymple, R.A., *Particle Methods and Waves, with Emphasis on SPH.* 2007.

97. Strang, G., *On the construction and comparison of difference schemes.* SIAM Journal on Numerical Analysis, 1968. **5**(3): p. 506-517.

98. Zukas, J.A., *High velocity impact dynamics*. 1990: Wiley-Interscience.

99. Baker, J. and A. Williams, *Hypervelocity penetration of plate targets by rod and rod-like projectiles.* International journal of impact engineering, 1987. **5**(1): p. 101-110.

100. Ahrens, T.J. and J.D. O'Keefe, *Impact on the Earth, ocean and atmosphere.* International journal of impact engineering, 1987. **5**(1): p. 13-32.

101. Roddy, D.J., et al., *Computer simulations of large asteroid impacts into oceanic and continental sites--preliminary results on atmospheric, cratering and ejecta dynamics.* International Journal of Impact Engineering, 1987. **5**(1): p. 525-541.

102. Benson, D.J. and W. Nellis, *Dynamic compaction of copper powder: Computation and experiment.* Applied physics letters, 1994. **65**(4): p. 418-420.

103. Benson, D., W. Tong, and G. Ravichandran, *Particle-level modeling of dynamic consolidation of Ti-SiC powders.* Modelling and Simulation in Materials Science and Engineering, 1995. **3**: p. 771.

104. Walker, J.D. and C.E. Anderson Jr. *Multi-material velocities for mixed cells*. in *AIP Conference Proceedings*. 1994.

105. Tran, L.B. and H.S. UdayKumar., *A particle levelset based sharp interface cartesian grid method for impact, penetration, and void collapse.* Journal of Computational Physics., 2004. **193**(2): p. 469-510.

106. Anderson, C.E., *An overview of the theory of hydrocodes.* International journal of impact engineering, 1987. **5**(1): p. 33-59.

107. Taylor, L. and D. Flanagan, *PRONTO 2D: A two-dimensional transient solid dynamics program*. 1987, Sandia National Labs., Albuquerque, NM (USA).

108. Camacho.G.T. and M.Ortiz., *Adaptive lagrangian modelling of ballistic penetration of metallic targets.* Comput. Methods Appl. Mech. Eng., 1997. **142**(3-4): p. 269-301.

109. Hallquist, J., *User's manual for DYNA2D: an explicit two-dimensional hydrodynamic finite element code with interactive rezoning*. 1980, Lawrence Livermore National Lab., CA (USA).

110. Batra, R. and J. Stevens, *Adiabatic shear bands in axisymmetric impact and penetration problems.* Computer methods in applied mechanics and engineering, 1998. **151**(3): p. 325-342.

111. Li, S., et al., *A meshfree contact-detection algorithm.* Computer methods in applied mechanics and engineering, 2001. **190**(24): p. 3271-3292.

112. Benson, D.J., *A mixture theory for contact in multi-material Eulerian formulations.* Computer methods in applied mechanics and engineering, 1997. **140**(1): p. 59-86.

113. Benson, D.J. and S. Okazawa, *Contact in a multi-material Eulerian finite element formulation.* Computer methods in applied mechanics and engineering, 2004. **193**(39): p. 4277-4298.

114. Vitali, E. and D.J. Benson, *An extended finite element formulation for contact in multi-material arbitrary Lagrangian–Eulerian calculations.* International journal for numerical methods in engineering, 2006. **67**(10): p. 1420-1444.

115. Vitali, E., *An extended finite element formulation for contact in multi-material arbitrary Lagrangian-Eulerian calculations*. 2007, UC San Diego Electronic Theses and Dissertations: UC San Diego.

116. Vitali, E. and D.J. Benson, *Contact with friction in multi-material arbitrary Lagrangian-Eulerian formulations using X-FEM.* International journal for numerical methods in engineering, 2008. **76**(6): p. 893-921.

117. Vitali, E., et al., *An extended Eulerian method for contacts in Godunov formulations.* International journal for numerical methods in engineering, 2012.

118. Sambasivan, S. and H.S. Udaykumar., *Ghost Fluid Method for Strong Shock Interactions Part 1: Fluid-Fluid Interfaces.* AIAA., 2009. **47**(12): p. 2907-2923.

119. Sambasivan, S. and H.S. Udaykumar., *Ghost fluid method for Strong Shock Interactions. Part2: Immersed Solid Boundaries.* AIAA., 2009. **47**(10): p. 2923-2937.

120. Kapahi, A., et al., *Parallel, sharp interface Eulerian approach to high-speed multi-material flows.* Computers & Fluids, 2012.

121. Curran, D., L. Seaman, and D. Shockey, *Dynamic failure of solids.* Physics reports, 1987. **147**(5-6): p. 253-388.

122. Lee, W., H.J. Lee, and H. Shin, *Ricochet of a tungsten heavy alloy long-rod projectile from deformable steel plates.* Journal of Physics D: Applied Physics, 2002. **35**: p. 2676.

123. Antoun, T., et al., *Spall fracture*. 2003, Springer Verlag: New York. p. 49-54.

124. Eftis, J., J. Nemes, and P. Randles, *Viscoplastic analysis of plate-impact spallation.* International journal of plasticity, 1991. **7**(1): p. 15-39.

125. Chen, Q., J. Wang, and K. Liu, *Improved CE/SE scheme with particle level set method for numerical simulation of spall fracture due to high-velocity impact.* Journal of Computational Physics, 2010. **229**(19): p. 7503-7519.

126. Seaman, L., D.R. Curran, and T.H. Antoun, *Dynamic Failure of Materials. Volume 2-Compilation of Russian Spall Data*. 1998, SRI INTERNATIONAL MENLO PARK CA.

127. Curran, D.R., *Nonhydrodynamic attenuation of shock waves in aluminum.* Journal of Applied Physics, 1963. **34**(9): p. 2677-2685.

128. Erkman, J. and A. Christensen, *Attenuation of shock waves in aluminum.* Journal of Applied Physics, 1967. **38**(13): p. 5395-5403.

129. Fowles, G., *Attenuation of the shock wave produced in a solid by a flying plate.* Journal of Applied Physics, 1960. **31**(4): p. 655-661.

130. Johnson, W., A. Sengupta, and S. Ghosh, *High velocity oblique impact and ricochet mainly of long rod projectiles: an overview.* International Journal of Mechanical Sciences, 1982. **24**(7): p. 425-436.

131. Tarver, C., J. Hallquist, and L. Erickson, *Modeling short pulse duration shock initiation of solid explosives*. 1985, Lawrence Livermore National Lab., CA (USA).